3D SOLID FINITE ELEMENT ROTORDYNAMICS:

PARAMETRIC STABILITY ANALYSIS AND CONTACT MODELLING

A Dissertation

by

JOSEPH OH

Submitted to the Office of Graduate and Professional Studies of
Texas A&M University
in partial fulfillment of the requirements for the degree of

DOCTOR OF PHILOSOPHY

Chair of Committee,	Alan B. Palazzolo
Committee Members,	C. Steve Suh
	Stefan Hurlebaus
	Won-Jong Kim
Head of Department,	Andreas A. Polycarpou

December 2020

Major Subject: Mechanical Engineering

ABSTRACT

Conventional rotordynamic analyses generally simplify the rotor, neglecting detailed geometrical characteristics. However, in modern rotating machines, rotors consist of multiple complex-shaped parts that are usually non-axisymmetric with preloads to ensure the assembly. These effects may significantly affect rotordynamic behavior of high-performance rotating machinery. The present study aims to take them into account in rotordynamic analyses, by presenting an efficient rotordynamic stability approach for non-axisymmetric rotor-bearing systems with complex shapes using three-dimensional solid finite elements. The 10-node quadratic tetrahedron element is used for the finite element formulation of the rotor. A rotor-bearing system, matrix differential equation is derived in the rotor-fixed coordinate system. The system matrices are reduced by using Guyan reduction. The current study utilizes the Floquet theory to determine the stability of solutions for parametrically excited rotor-bearing systems. Computational efficiency is improved by discretization and parallelization, taking advantage of the discretized Monodromy matrix of Hsu's method. The method is verified by an analytical model with the Routh-Hurwitz stability criteria, and by direct time-transient, numerical integration for large order models. The proposed and Hill's methods are compared with respect to accuracy and computational efficiency, and the results indicate the limitations of the Hill's method when applied to 3D solid rotor-bearing systems. A parametric investigation is performed for an asymmetric Root's blower type shaft, varying bearing asymmetry and bearing damping. In addition to the

non-axisymmetric rotor-bearing system analysis, a new contact model for rotordynamic analysis of an assembled rotor-bearing system with multiple parts connected by multiple joints is suggested. A contact element formulation is presented using solid finite elements and statistics-based contact theories. A test arrangement was developed to validate the proposed contact model for varying interface surface roughness and preloads. An iterative computation algorithm is introduced to solve the implicit relation between contact stiffness and stress distribution. Prediction results, using the contact model, are compared with measured natural frequencies for multiple configurations of a test rotor assembly. A case study is performed for an overhung type rotor-bearing system to investigate the effect of contact interfaces, between an overhung impeller and a rotor shaft, on critical speeds.

DEDICATION

To Gloria

ACKNOWLEDGEMENTS

I would like to thank my committee chair Dr. Palazzolo, whose passionate and knowledgeable guidance made this work possible. I also thank my committee members Dr. Suh, Dr. Hurlebaus, and Dr. Kim for their support and services throughout the long journey of my Ph.D. program.

Thanks also go to the department of mechanical engineering faculty and staff for making my time at Texas A&M University a great experience. I would like to give my gratitude to my colleagues at VCEL, especially to those who spent most of the time in the office and the lab together: Jongin, Dongil, Ahmad, MD, Baik Jin, Lingnan, Xiaomeng, Xiao, Yashu, and Farzam.

My special thanks go to Dwell church family for their genuine love and prayer support during the years of my study. I am always grateful to my old friends Youngseok and Yohan for their encouragement and genuine friendship. I can't be more grateful to my parents for their limitless encouragement and love. Their prayer strongly held me to stand firm in the faith in Jesus Christ, my Lord and Savior even in times of difficulty. Finally, my deep gratitude goes to my beloved wife, Gloria for her patient love and support through the entire years of my Ph.D. study. I thank God for bringing my children, Jacob and Marianne to us.

CONTRIBUTORS AND FUNDING SOURCES

Contributors

This work was supervised by a dissertation committee consisting of Professor Palazzolo, Professor Suh, and Professor Kim of the Department of Mechanical Engineering and Professor Hurlebaus of the Department of Civil Engineering.

All work conducted for the dissertation was completed by the student independently.

Funding Sources

The funding for this work was provided by the Turbomachinery Research Consortium (TRC) at Texas A&M University.

NOMENCLATURE

FEM	Finite Element Method
dof	Degree of Freedom
$\underline{\boldsymbol{P}}$	Coordinate of an arbitrary point in a rotating body
$\underline{\boldsymbol{r}}$	Position vector of $\underline{\boldsymbol{P}}$
$\underline{\boldsymbol{x}}$	Coordinate vector
$\underline{\boldsymbol{u}}$	Displacement vector
Ω	Spin speed
$\underline{\boldsymbol{\Omega}}$	Spin speed vector
$\underline{\boldsymbol{\Upsilon}}$	Rotation matrix
E_k^e	Kinetic energy of an element
$\underline{\boldsymbol{q}}^e$	Nodal displacement vector
$\underline{\boldsymbol{N}}$	Shape function matrix
$\underline{\boldsymbol{x}}_0$	Nodal coordinate vector of an element
$\underline{\boldsymbol{B}}$	strain-displacement relation matrix
$\underline{\boldsymbol{E}}$	Constitutive relation matrix
$\underline{\boldsymbol{M}}_e$	Element mass matrix
$\underline{\boldsymbol{C}}_e$	Element Coriolis matrix
$\underline{\boldsymbol{K}}_s^e$	Element structural stiffness matrix
$\underline{\boldsymbol{K}}_d^e$	Element dynamic stiffness matrix
$\underline{\boldsymbol{f}}_c^e$	Centrifugal force vector

ξ_i	Natural coordinates
ξ_{ik}	i^{th} direction coordinate of the k^{th} Gauss quadrature point
w_k	Weight factor corresponding to k^{th} Gauss quadrature point
$\underline{\boldsymbol{K}}_{b,i}$	Bearing stiffness coefficient matrix in inertial coordinates
$\underline{\boldsymbol{C}}_{b,i}$	Bearing damping coefficient matrix in inertial coordinates
$\underline{\boldsymbol{R}}$	Rotation matrix for coordinate transformation
$\underline{\boldsymbol{K}}_{b,r}$	Bearing stiffness coefficient matrix in rotor-fixed coordinates
$\underline{\boldsymbol{C}}_{b,r}$	Bearing damping coefficient matrix in rotor-fixed coordinates
$\underline{\boldsymbol{M}}$	System mass matrix
$\underline{\boldsymbol{C}}$	System damping matrix
$\underline{\boldsymbol{K}}$	System stiffness matrix
$\boldsymbol{f}_c$	System centrifugal force vector
R_i	Mass-to-stiffness ratio for Guyan reduction
$\underline{\boldsymbol{M}}^R$	Reduced system mass matrix
$\underline{\boldsymbol{C}}^R$	Reduced system damping matrix
$\underline{\boldsymbol{K}}^R$	Reduced system stiffness matrix
$\boldsymbol{f}_c^R$	Reduced system centrifugal force vector
$\underline{\boldsymbol{B}}(t)$	Time-varying coefficient matrix
$\underline{\boldsymbol{O}}_N$	N by N null matrix
$\underline{\boldsymbol{I}}_N$	N by N identity matrix
T_{min}	Minimum time period of $\underline{\boldsymbol{B}}(t)$
$\underline{\boldsymbol{\Phi}}_{\boldsymbol{M}}(t)$	Matrizant matrix

$\underline{\boldsymbol{H}}_M$	Monodromy matrix
$\underline{\boldsymbol{B}}_k$	Piecewise contact coefficient matrix
$\underline{\boldsymbol{H}}_M(K)$	Discretized Monodromy matrix
m	Point mass
c_r	Rotor internal damping
c_e	Rotor external damping
k_υ	Rotor stiffness along the υ-axis
k_η	Rotor stiffness along the η-axis
q	Rotor asymmetry
q_r	Rectangular cross-section rotor asymmetry
h	Height
w	Width
$k_{b,xx}$	Bearing stiffness in the x-direction corresponding to u_x
$k_{b,yy}$	Bearing stiffness in the y-direction corresponding to u_y
$k_{b,xy}$	Bearing stiffness in the x-direction corresponding to u_y
$k_{b,yx}$	Bearing stiffness in the y-direction corresponding to u_x
$c_{b,xx}$	Bearing damping in the x-direction corresponding to u_x
$c_{b,yy}$	Bearing damping in the y-direction corresponding to u_y
$c_{b,xy}$	Bearing damping in the x-direction corresponding to u_y
$c_{b,yx}$	Bearing damping in the y-direction corresponding to u_x
c_E	Equivalent bearing damping coefficient
m_r	Rotor point mass

k_E	Equivalent bearing stiffness coefficient
ζ	Damping ratio
q_b	Bearing asymmetry
$\underline{p(t)}$	General solution of rotor-bearing system equations
$\underline{p_n(t)}$	Periodic function
α_F	Floquet exponent
$\underline{\boldsymbol{K}_0}^R$	Coefficient matrix of the constant term in $\underline{\boldsymbol{K}}^R$
$\underline{\boldsymbol{K}_s}^R$	Coefficient matrix of the sine term in $\underline{\boldsymbol{K}}^R$
$\underline{\boldsymbol{K}_c}^R$	Coefficient matrix of the cosine term in $\underline{\boldsymbol{K}}^R$
j_{max}	Truncation number of Hill's infinite determinant
k_x	bearing stiffness in the *x*-direction for Jeffcott rotor
k_y	bearing stiffness in the *y*-direction for Jeffcott rotor
$\underline{\boldsymbol{M}_T}$	Mass matrix for Timoshenko beam model
$\underline{\boldsymbol{C}_T}$	Damping matrix for Timoshenko beam model
$\underline{\boldsymbol{K}_T}$	Stiffness matrix for Timoshenko beam model
$\underline{\boldsymbol{D}}$	Constant coefficient matrix for first order state-space equations
λ	Eigenvalue
α	Real part of eigenvalue
β	Imaginary part of eigenvalue
$\underline{\boldsymbol{K}_\sigma}$	Stress-stiffness matrix
$\underline{\boldsymbol{h}}^e$	Element contact stiffness matrix
Π_c^e	Potential energy of the contact element

$\underline{\boldsymbol{u}}^e$	Displacement vector of the element
$\underline{\boldsymbol{d}}^e$	Nodal dof vector of the element
$\underline{\boldsymbol{k}}_c^e$	Element contact stiffness coefficient matrix
$\underline{\boldsymbol{N}}_i^e$	Element inter-domain shape function matrix
$\underline{\boldsymbol{e}}_n^e$	Unit vector normal to the contact plane
$\underline{\boldsymbol{e}}_{t1}^e$	Orthogonal unit vector 1 tangential to the contact plane
$\underline{\boldsymbol{e}}_{t2}^e$	Orthogonal unit vector 2 tangential to the contact plane
k_{ct1}^e	Contact stiffness in $\underline{\boldsymbol{u}}_{t1}^e$ direction
k_{ct2}^e	Contact stiffness in $\underline{\boldsymbol{u}}_{t2}^e$ direction
ns	Number of the nodes of face nodes
N_1	Shape function of node 1
N_{ns}	Shape function of node ns
n_G	Number of Gauss quadrature integration points
$det(\underline{\boldsymbol{J}})$	Determinant of the Jacobian matrix
J	Jacobian matrix
$\xi_{1\alpha}$	Gauss quadrature point in the α-direction
$\xi_{2\beta}$	Gauss quadrature point in the β-direction
w_α	Weight factor corresponding to $\xi_{1\alpha}$
w_β	Weight factor corresponding to $\xi_{2\beta}$
$\underline{\boldsymbol{K}}_c$	Assembled contact stiffness matrix
$\underline{\boldsymbol{I}}$	Identity matrix
$\underline{\boldsymbol{0}}$	Null matrix

E'	Plane-stress modulus
$z(x)$	Surface height profile along with the linear path x
η_s	Area density
R_s	Average radius of the asperity
σ_s	Standard deviation of height
m_i	Zeroth, second, and fourth spectral moments, I = 0, 2, 4
P_c	Contact pressure
h	Standardized separation
$F_n(h)$	A solution of parabolic cylinder function
U	Whittaker function
$\phi^*(s)$	Gaussian distribution function
K	Modified Bessel function
υ	Poisson's ratio
E	Elastic modulus
D_{out}	Outer diameter
D_{in}	Inner diameter
L	Length
ρ	Density
BJ_A	Surface of joint A
BJ_B	Surface of joint B
BJ_C	Surface of joint C
BJ_Ap	Contact plane between joint A and the shaft

BJ_Bp	Contact plane between joint B and the shaft
BJ_Cp	Contact plane between joint C and the shaft
$\underline{\boldsymbol{K}}_{sys}$	Constant system stiffness matrix
$\underline{\boldsymbol{K}}_{bc}$	Contact stiffness at boundary faces
σ_{zz}	Stress in the *z*-direction
$\underline{\boldsymbol{K}}_{s}$	Structural stiffness matrix
$\underline{\boldsymbol{C}}_{R}$	Coriolis matrix
$\underline{\boldsymbol{K}}_{d}$	Dynamic stiffness matrix
SFER	Standalone code for Solid Finite Element Rotordynamic
VCEL	Vibration, Controls, and Electro-mechanics Laboratory
XLTRC^2	Rotordynamic code by TurboLab, Texas A&M University

TABLE OF CONTENTS

Page

LIST OF FIGURES

Page

LIST OF TABLES

Page

1. INTRODUCTION

1.1. Problem Statement and Motivation

As modern industry faces uprising demands of highly efficient systems with higher power density, light weight, and faster rotating speed, rotating machinery gets more complex and sophisticated. In general, an increase of spin speed in rotating machinery is advantageous in productivity. Furthermore, the higher spin speed lowers the required torque for the same amount of power generation compared to lower spin speed machines, allowing the machines to be lighter in weight [1]. On account of these technical trends, unprecedented dynamic behaviors of rotating machinery are likely to arise, resulting in accurate predictions to be more challenging. On the other hand, the operating conditions of rotating machines, such as rotating speeds, have to be determined within a range satisfying safety criteria. A failure of a proper prediction may cause severe damages of the facilities followed by a huge amount of financial loss. Rotordynamic analysis spans not only design stages, but also overall machine-life-cycles including operations and preventive maintenances.

1.2. Background

1.2.1. Finite Element Rotordynamics: Beam-type and Solid Elements

Rotating machinery mainly consists of rotors, stators, and bearings, and an adequate rotordynamic model should account for these components with the related forces [2]. Historically, several models accounting for a flexible rotor have suggested.

Jeffcott rotor is one of the simplest models which describes a flexible rotor with 2 degree of freedoms (dofs) [3]. Lumped-parameter models [4, 5] have been employed to represent the distributed elastic and inertial properties of rotors, discretizing a solution of continuous partial differential equations. The finite element method (FEM) using Rayleigh-Ritz approach approximate partial differential [6, 7, 8] . FEM provides a more accurate solution than the lumped-parameter model compared to an exact solution [8]

Figure 1.1 Beam-type element rotor

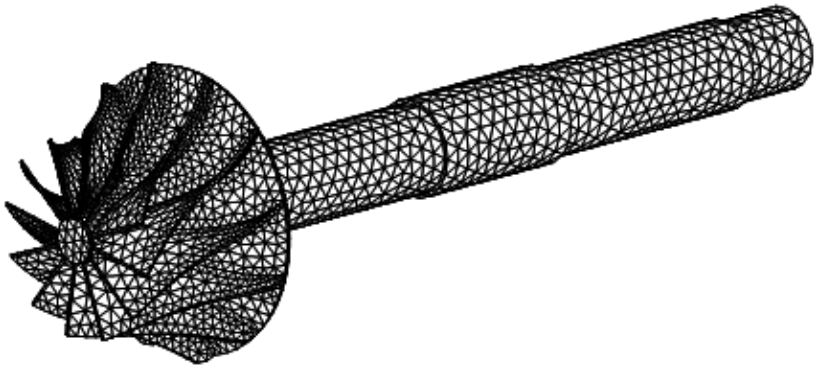

Figure 1.2 Solid element rotor

beam-type finite element models such as the Euler-Bernoulli beam and the Timoshenko beam [9] have been developed and performed reliably. To accommodate more complex geometrical characteristics, such as thin walled rotor, axisymmetric solid finite elements have been used [10, 11]. There are more cases when either beam theories or axisymmetric solid elements are inadequate to model the behavior of rotors, for example, a rotor with bladed disks with non-axisymmetric structure [1]. In such cases, 3D solid finite element rotor model can be utilized for such cases without ignoring geometrical characteristics [12, 13].

1.2.2. Non-Axisymmetric Rotor-Bearing Systems

As rotor-bearing systems become complex, accurate predictions of system stability get more acute job. Numerous effort has been invested to implement all the details of the system into analyses [14, 15, 16, 17, 18]. When it comes to rotor structure, accounting for geometrical details is one of the important aspects of the on-going development. In contrast to the simplified rotor models which would be used in beam-type rotordynamic analyses: lumped and axisymmetric, the rotors of many industrial machines are not axisymmetric due to the rotor disk blades, couplings, and etc. The rotor models do not need to be axisymmetric when using 3D solid finite element formulations. Therefore, non-axisymmetric rotors, i.e., two-pole turbine generators, three-bladed wind turbines, Root's type impellers, cracked rotors, etc. can be taken into account in rotordynamic analyses by taking advantage of the 3D solid element method.

1.2.3. Contact Model for Assembled Rotor-Bearing Systems

In general, rotating machines are assembled with multiple parts: impellers, disks, shafts, couplings and etc. These parts are tightened by bolts and nuts or fitted by press fits and interference fits. The dynamic behavior of an assembled rotor may be different from the one of a seamless body rotor due to the existence of contacts and forces caused by clamping objects. There are various contributing factors to the contact effect, such as sizes and shapes of contact areas, surface roughness at interfaces, misalignments of each part, stress-stiffening effect due to clamping forces, and so on. Most of the contributing factors are geometry-dependent parameters that are hardly predicted by conventional rotordynamic analyses using beam-type elements or even solid-type elements when contacts between different domains are not properly considered. Therefore, neglecting the contact effect may result in a significant decrease of prediction accuracy [19].

1.3. Literature Review

1.3.1. Stability Analysis for Non-Axisymmetric Rotor-Bearing Systems [20]

Prior research has suggested various approaches for modeling rotors with complex geometry using the 3D solid finite element method. Nandi and Neogy proposed a 3D solid finite element model for rotordynamic analysis [12]. They showed the 3D solid finite element model performs better than beam-type finite element models for rotors with high slenderness ratios. Chatelet et al. presented a flexible bladed disc-shaft model by using a multilayered shell element based on a cyclic symmetry assumption [21]. Combescure and Lazarus used a refined 3D model and a 2D Fourier model to

demonstrate significant improvement on predicting the dynamic behavior of flexible rotor disks [22]. Chaudhry described a solid finite element modeling method for rotors with slender shafts and many blades [23]. This method, however, is only available for rotor-bearing systems with radially isotropic bearings. The matrix equations of motion include time-varying coefficients for a non-axisymmetric rotor supported by non-axisymmetric bearings. This may destabilize the rotor-bearing system due to parametric excitation. Several approaches have been proposed to investigate the rotordynamic behavior of non-axisymmetric rotor-bearing systems. Black discussed lateral motion of a multi-degree-of-freedom shaft with cross-sectional asymmetry mounted on asymmetrically flexible bearings [24]. He used the perturbation-variation method of Hsu to solve the equation of motion [25].

Genta presented the finite element based equations of motion in the inertial frame for a general multi-degree of freedom rotor, and presented the solution for a non-axisymmetric rotor running on an asymmetric supporting structure [26]. In this approach, Hill's infinite determinant was used to approximate the solution for non-axisymmetric rotor-bearing systems. The Monodromy matrix method can be utilized for stability analyses, and several works with beam-type finite element models have been published [27, 28]. These papers utilized numerical integration for evaluation of the Monodromy matrix, which is less efficient than the Hsu approach utilized here.

Lazarus et al. suggested the 3D finite element method based on the modal theory in order to analyze linear periodic time-varying systems [13]. The authors mainly followed Genta's approach by utilizing the Floquet theory and Hill's infinite determinant,

considering a small number of flexural modes in the inertial frame. The literature demonstrates that the Hill method predicts instabilities accurately and efficiently with tolerable approximation errors for weakly coupled systems, without Coriolis force or gyroscopic effects. However, use of transient numerical integration as a benchmark in the present work demonstrates that the Hill method predicts stability inaccurately for a case of large order, with non-axisymmetric rotor plus non-axisymmetric bearings, and including Coriolis and gyroscopic effects. This weakness in the Hill method for the example is demonstrated to be remedied by use of an alternative "Hsu" type method.

The Coriolis force must be included in the 3D solid finite element described in the rotor-fixed coordinate system. Ma et al. presented a Hill's infinite determinant based analysis for a 3D finite element model [29]. Their method was numerically verified in the inertial frame, comparing results with Genta's [26]. A distribution of unstable speed ranges due to asymmetry of the rotor and bearings appeared to be missed in their predictions**.** Tai and Shen presented closed-form solutions for a spinning, cyclic symmetric rotor with 3D solid finite element [30]. The prior literature's quantitative studies on the effects of combined rotor and bearing asymmetry on system stability is very sparse.

The present study utilizes a 10-node quadratic tetrahedron element for developing finite element models of non-axisymmetric rotor-bearing systems. Hsu's approximation method is adopted to generate the discretized Monodromy matrix [31]. Parametric studies are conducted for the effect of bearing asymmetry and bearing damping on the stability of a non-axisymmetric rotor-bearing system. Direct time-transient integration using a fourth order Runge-Kutta method and an analytical model with the Routh-

Hurwitz stability criteria are provided for verifications. Some limitations of the existing Hill's infinite determinant related methods are identified by comparison with the proposed approach and direct numerical integration.

1.3.2. 3D Solid Finite Element Contact Model for Assembled Rotor-Bearing Systems [32]

The importance of taking contact effect into consideration was reported in [19]. The evolution of contact model starting from the GW contact model [33] was reviewed by Müser and et al. [34]. The present work focuses on accounting for contact interface effects of stacked rotor assemblies on rotordynamic response, while there are other applications for contact theory modeling, as exemplified by the work in the area of bladed disk vibration [35, 36], numerical studies on jointed structures using zero thickness contact elements, the penalty method, etc. [37, 38, 39, 40, 41, 42], and experimental studies on the assembled structures [43, 44, 45, 46].

In prior research, there are several approaches for modeling the contact effect in the finite element method. Modeling approaches with 2D axisymmetric solid elements [47], beam-type elements [48, 49, 50, 51] and 3D solid elements [52, 53] were used for rotordynamic analyses of assembled rotors. Zhang, Du, Shi and Liu [47] utilized empirically obtained contact stiffness for their 2D axisymmetric finite element rotor model. For the beam-type approaches [48, 49, 50, 51], statistical contact theories were adopted to calculate contact stiffness at joints. Geometrical characteristics and the stress-stiffening effect were not considered with these beam-type methods. Prior

studies were conducted with 3D solid elements [52, 53], and included geometric details and stress stiffening. The contact stiffnesses at the interfaces were modeled using an axial layer with a fictitious elastic modulus, adjusted to match experimental natural frequency measurements. This may have limited use for original rotor assembly design, where natural frequency measurements are not available.

The novel contribution of the present work is a new approach for applying GW contact theory model to stacked, preloaded, spinning shaft assemblies, as found in industrial and aviation turbines and compressors. This extends prior work in this application area by employing a higher fidelity, 3D solid element, finite element model, with zero-thickness-plane-type contact elements at contact interfaces. The suggested model can be applied to various types of joints in rotor-bearing systems without imposing simplifying geometrical modeling assumptions. In addition, the approach has a greater level of universality by not requiring prior tests to establish “equivalent” parameters, such as an equivalent Youngs modulus, for a given shaft assembly. Therefore, the asperity induced, contact stiffness model at interfaces can be evaluated by the prediction model at the design stage, without measuring natural frequencies of the built system.

In this paper, a finite element formulation of the contact element with a statistics-based contact theory is presented. A test rig for a through-bolt type rotor assembly with multiple joints is built, and experimental results are obtained to validate the proposed contact modeling method. An iterative procedure for a prediction model is introduced, and simulation results of the prediction model are compared with the experimental

results. Finally, a rotordynamic analysis is carried out for an overhung type rotor-bearing system using the proposed contact modeling method.

1.4. Objectives

The present study seeks the following objectives:

I. Investigate instabilities caused by non-axisymmetric rotor-bearing systems.

II. Derive 3D solid finite element formulation dedicated to rotordynamic analyses.

III. Generalize simulation modelling method for evaluating stability of non-axisymmetric solid rotor-linear bearing system using Floquet theory.

IV. Improve computational efficiency by utilizing Hsu's method.

V. Conduct quantitative comparison between Hill's method and Hsu's method both in the rotor-fixed coordinate system and the inertial coordinate system.

VI. Derive a contact model finite element formulation which is suitable for the 3D solid finite element rotordynamic analysis.

VII. Develop the contact stiffness calculation algorithm for a preloaded rotor structure

VIII. Validate the contact model by conducting an experimental test rig.

1.5. Novelties and Contributions

In the present study, non-axisymmetric rotor-bearing systems and contact modeling within rotor-assemblies are investigated via 3D solid finite element method. These subjects have been challenging in conventional rotordynamic analysis on account

of geometrical complexities. Beam-type elements couldn't afford to fully implement geometrical variances of non-axisymmetric rotor [24, 27, 28]. Though 3D solid finite element method was utilized, obtaining a Floquet solution of the problem was still challenging with respect to computational loads [30]. As an alternative way, Hill's determinant with modal reduction was adopted, but verification of the method was done only in the inertial frame of reference [1, 29].

The author presents a new efficient way of obtaining a Floquet solution for non-axisymmetric rotor-bearing systems by adopting 3D solid element method and Hsu's approximation [31]. The proposed method is verified by Routh-Hurwitz stability criteria. Monodromy matrix method [54] and Hill's determinant method [1] for the same Floquet solution of a rotor-bearing system are compared quantitively in both the inertial frame of reference and the rotating frame of reference with respect to accuracy and computational speed. Some limitations of Hill's determinant are shown in a numerical approach. It is also proven that the proposed method can be used to detect non-parametric instability as well.

As regard to contact modeling, a new contact element for 3D solid finite element rotordynamic analysis is proposed. While equivalent flexural stiffness method [48, 49, 50, 51] and fictitious elastic modulus method [52, 53] have been suggested so far, no general contact algorithm which accounts for geometrical variances and surface roughness with an adequate modeling algorithm has been published yet. The author proposes a model which can be applied to various types of joints in rotor-bearing systems without geometrical limitations. Furthermore, statistics-based contact theories

can be applied directly to the 3D solid finite element rotordynamic model without additional manipulations, such as generating fictitious modulus. Therefore, asperity effect at interfaces can be evaluated by the prediction model with surface roughness parameters case independently.

When it comes to experimental validations for contact models, adequate test results with full descriptions for surface roughness parameters and accurate preload measurements are very sparse in literature. No surface roughness parameters were measured in most references, while only one paper compared multiple levels of surface roughness on dynamic characteristics of a stacked rotor [47], still providing only a rough mean value of height of the surface that are insufficient for a proper contact modeling. The present research builds a test rig for a through-bolt type rotor assembly with multiple joints, providing full descriptions for geometries and surface roughness parameters for contact theories. Unlike explicit modeling methods that have been shown in prior research, lacking accurate predictions for stress distribution, an implicit contact modeling algorithm is presented, providing more accurate stress distribution at contact interfaces.

2. STABILITY ANALYSIS FOR NON-AXIYSMMETRIC ROTOR-BEARING SYSTEMS* [20]

2.1. Rotordynamic System Modelling with the Finite Element Method

2.1.1. Equation of Motion in the Rotor-Fixed Coordinate System

The rotor-fixed coordinate system is attached to the spinning rotor and rotates along with the rotor at the same speed. The rotor-fixed coordinate system is advantageous for describing detailed kinematics when it comes to non-axisymmetric rotors [13]. In this study, non-axisymmetric rotors are described in the rotor-fixed coordinate system. In order to develop the equation of motion of a non-axisymmetric rotor, the rotor is assumed to have small displacements and to spin at a constant speed. Figure 2.1 shows a point $\underline{\boldsymbol{P}}$ on the rotating body and its position vector $\underline{\boldsymbol{r}} = \underline{\boldsymbol{x}} + \underline{\boldsymbol{u}}$, where $\underline{\boldsymbol{x}}$ and $\underline{\boldsymbol{u}}$ are the coordinate vector and the displacement vector, respectively. The body is rotating at speed Ω about the $\boldsymbol{z}$-axis along with the rotor-fixed coordinate system $\boldsymbol{\upsilon\eta z}$. The relation between the time derivatives of position vector $\underline{\boldsymbol{r}}$ in the inertial coordinate system and the rotor-fixed coordinate system can be written as [23]

$$\underline{\left(\frac{d\boldsymbol{r}}{dt}\right)}_{i} = \underline{\left(\frac{d\boldsymbol{r}}{dt}\right)}_{r} + \underline{\boldsymbol{\Omega}} \times \underline{\boldsymbol{r}} \tag{2.1}$$

* Reprinted in part with permission from "Stability of Non-Axisymmetric Rotor and Bearing Systems Modeled With Three-Dimensional-Solid Finite Elements," by Oh, J., Palazzolo, A., and Hu, L., 2020. *ASME J. Vib. Acoust.*, 142(1), pp. 011010., Copyright 2020 by ASME.

where subscripts i and r mean the inertial coordinate system and the rotor-fixed coordinate system, respectively, and the rotating frame, time rate of change term $\underline{\left(\frac{d\boldsymbol{r}}{dt}\right)}_r$ is that which is sensed by an observer in the rotating frame. The angular velocity vector $\underline{\boldsymbol{\Omega}}$ of the rotor-fixed coordinate system is represented in vector form as

$$\underline{\boldsymbol{\Omega}} = \Omega\underline{\boldsymbol{\Upsilon}}$$

$$\boldsymbol{\Upsilon} = \begin{bmatrix} 0 & -1 & 0 \\ 1 & 0 & 0 \\ 0 & 0 & 0 \end{bmatrix} \tag{2.2}$$

Then equation (2.1) can be written as

$$\underline{\left(\frac{d\boldsymbol{r}}{dt}\right)}_i = \underline{\left(\frac{d\boldsymbol{r}}{dt}\right)}_r + \Omega\underline{\boldsymbol{\Upsilon}} \cdot \underline{\boldsymbol{r}} \tag{2.3}$$

Let the body be an element of the rotor, then the kinetic energy of the element in the spinning rotor is obtained from equation (2.3) as

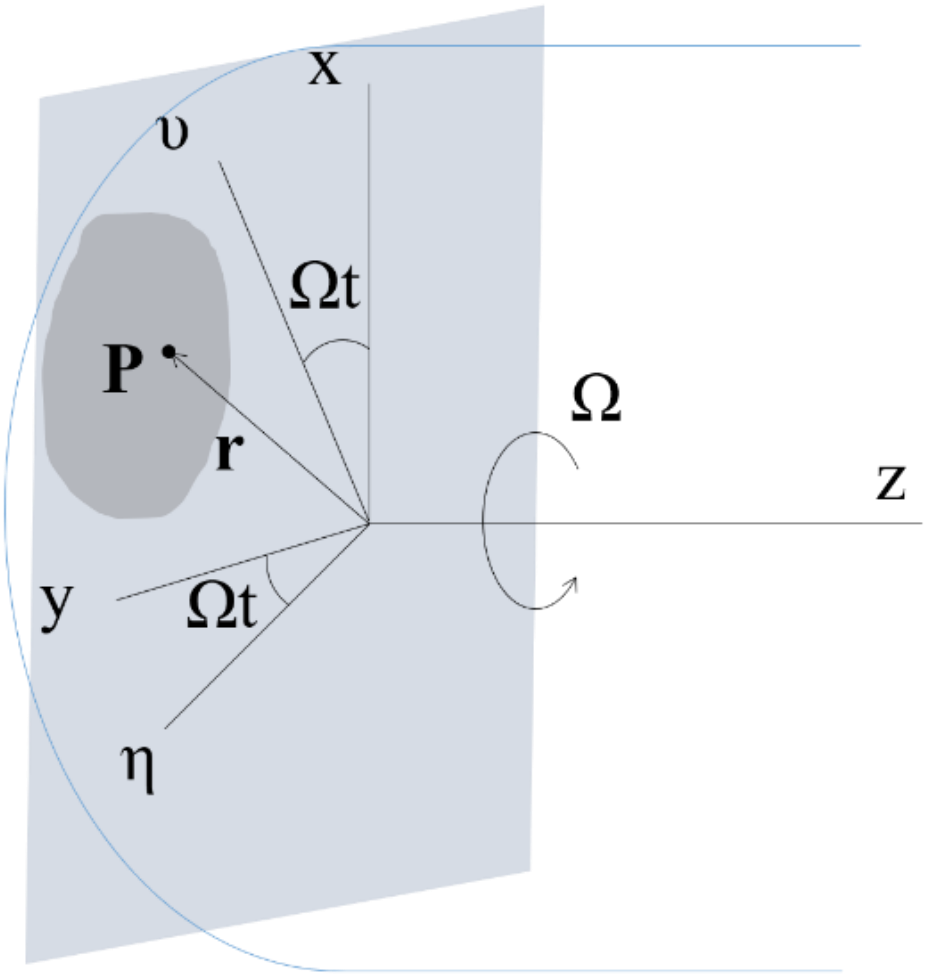

Figure 2.1 Rotor-fixed coordinate system

$$
\begin{aligned}
E_k^e &= \frac{1}{2}\int_{V_e} \rho \underline{\left(\frac{d\boldsymbol{r}}{dt}\right)}_i^T \underline{\left(\frac{d\boldsymbol{r}}{dt}\right)}_i dV_e \\
&= \frac{1}{2}\int_{V_e} \rho \left(\underline{\dot{\boldsymbol{u}}} + \underline{\boldsymbol{\Upsilon}} \cdot \left(\underline{\boldsymbol{u}} + \underline{\boldsymbol{x}}\right)\right)^T \left(\underline{\dot{\boldsymbol{u}}} + \underline{\boldsymbol{\Upsilon}} \cdot \left(\underline{\boldsymbol{u}} + \underline{\boldsymbol{x}}\right)\right) dV_e \\
&= \frac{1}{2}\left(\underline{\dot{\boldsymbol{q}}}^e\right)^T \int_{V_e} \rho \underline{\boldsymbol{N}}^{\boldsymbol{T}} \underline{\boldsymbol{N}} dV_e \, \underline{\dot{\boldsymbol{q}}}^e + \left(\underline{\dot{\boldsymbol{q}}}^e\right)^T \int_{V_e} \rho \underline{\boldsymbol{N}}^{\boldsymbol{T}} \underline{\boldsymbol{\Upsilon}} \underline{\boldsymbol{N}} dV_e \, \underline{\boldsymbol{q}}^e \\
&+ \left(\underline{\dot{\boldsymbol{q}}}^e\right)^T \int_{V_e} \rho \underline{\boldsymbol{N}}^{\boldsymbol{T}} \underline{\boldsymbol{\Upsilon}} \underline{\boldsymbol{N}} dV_e \, \underline{\boldsymbol{x_0}} + \frac{1}{2}\left(\underline{\boldsymbol{q}}^e\right)^T \int_{V_e} \rho \underline{\boldsymbol{N}}^{\boldsymbol{T}} \underline{\boldsymbol{\Upsilon}}^{\boldsymbol{T}} \underline{\boldsymbol{\Upsilon}} \underline{\boldsymbol{N}} dV_e \, \underline{\boldsymbol{q}}^e \\
&+ \frac{1}{2}\left(\underline{\boldsymbol{q}}^e\right)^T \int_{V_e} \rho \underline{\boldsymbol{N}}^{\boldsymbol{T}} \underline{\boldsymbol{\Upsilon}}^{\boldsymbol{T}} \underline{\boldsymbol{\Upsilon}} \underline{\boldsymbol{N}} dV_e \, \underline{\boldsymbol{x_0}} \\
&+ \frac{1}{2}\underline{\boldsymbol{x_0}}^{\boldsymbol{T}} \int_{V_e} \rho \underline{\boldsymbol{N}}^{\boldsymbol{T}} \underline{\boldsymbol{\Upsilon}}^{\boldsymbol{T}} \underline{\boldsymbol{\Upsilon}} \underline{\boldsymbol{N}} dV_e \, \underline{\boldsymbol{q}}^e \\
&+ \frac{1}{2}\underline{\boldsymbol{x_0}}^{\boldsymbol{T}} \int_{V_e} \rho \underline{\boldsymbol{N}}^{\boldsymbol{T}} \underline{\boldsymbol{\Upsilon}}^{\boldsymbol{T}} \underline{\boldsymbol{\Upsilon}} \underline{\boldsymbol{N}} dV_e \, \underline{\boldsymbol{x_0}}
\end{aligned} \tag{2.4}
$$

where E_k^e is the kinetic energy of the element, $\underline{\boldsymbol{q^e}}$ is the nodal displacement vector of the element, $\underline{\boldsymbol{N}}$ is the shape function matrix, $\underline{\boldsymbol{x_0}}$ is the nodal coordinate vector of the element. The potential energy of the rotor from deformation can be written by

$$
E_p^e = \frac{1}{2}\underline{\boldsymbol{q^e}}(t)^T \int_{V_e} \underline{\boldsymbol{B}}^{\boldsymbol{T}} \underline{\boldsymbol{E}} \, \underline{\boldsymbol{B}} \, dV \, \underline{\boldsymbol{q^e}}(t) \tag{2.5}
$$

where $\underline{\boldsymbol{B}}$ provides strains when multiplied into $\underline{\boldsymbol{q}^e}$, and $\underline{\boldsymbol{E}}$ is the constitutive relation matrix [9]. The Euler-Lagrange equation for the system is

$$\frac{d}{dt}\left(\frac{dE_k^e}{d\underline{\dot{\boldsymbol{q}}^e}(t)}\right) - \frac{dE_k^e}{d\underline{\boldsymbol{q}^e}(t)} + \frac{dE_p^e}{d\underline{\boldsymbol{q}^e}(t)} = 0 \tag{2.6}$$

The equation of motion of the element is obtained by substituting equations (2.4) and (2.5) into (2.6), yielding [23, 11],

$$\underline{\boldsymbol{M}^e}\,\underline{\ddot{\boldsymbol{q}}^e}(t) + 2\Omega\underline{\boldsymbol{C}^e}\,\underline{\dot{\boldsymbol{q}}^e}(t) + \left(\underline{\boldsymbol{K}_s^e} - \Omega^2\underline{\boldsymbol{K}_d^e}\right)\underline{\boldsymbol{q}^e}(t) = \Omega^2\underline{\boldsymbol{f}_c^e} \tag{2.7}$$

where $\underline{\boldsymbol{M}^e}$, $\underline{\boldsymbol{C}^e}$, $\underline{\boldsymbol{K}_s^e}$, $\underline{\boldsymbol{K}_d^e}$ and $\underline{\boldsymbol{f}_c^e}$ are the element mass matrix, the element Coriolis matrix, the element structural stiffness matrix, the element dynamic stiffness matrix and the centrifugal force vector, respectively.

$$\underline{\boldsymbol{M}^e} = \int_{V_e} \rho\underline{\boldsymbol{N}^T}\,\underline{\boldsymbol{N}}dV_e \tag{2.8}$$

$$\underline{\boldsymbol{C}^e} = \int_{V_e} \rho\underline{\boldsymbol{N}^T}\boldsymbol{\Upsilon}\boldsymbol{N}dV_e \tag{2.9}$$

$$\underline{\boldsymbol{K}_s^e} = \int_{V_e} \underline{\boldsymbol{B}^T}\,\underline{\boldsymbol{E}}\,\underline{\boldsymbol{B}}\,dV \tag{2.10}$$

$$\underline{\boldsymbol{K}_d^e} = \int_{V_e} \rho\underline{\boldsymbol{N}^T}\,\underline{\boldsymbol{\Upsilon}^T}\,\underline{\boldsymbol{\Upsilon}}\,\underline{\boldsymbol{N}}dV_e \tag{2.11}$$

$$\underline{\boldsymbol{f}}_c^e = \int_{\mathrm{V}_e} \rho \underline{\boldsymbol{N}}^T \underline{\boldsymbol{\Upsilon}}^T \underline{\boldsymbol{\Upsilon}}\, \underline{\boldsymbol{N}}\, d\mathrm{V}_e\, \underline{\boldsymbol{x}}_0 \tag{2.12}$$

2.1.2. 10-node, Quadratic, Isoparametric Tetrahedron Element

One of the advantages of using tetrahedron elements in the finite element formulations is the ability to create unstructured mesh for complex geometry structures. In reality, geometries of rotors are complex and non-axisymmetric; for example, a gas-turbine rotor with many blades, a screw compressor rotor, a motor armature, etc. High-order elements, such as the 10-node quadratic tetrahedron shown in Figure 2.2, may be preferable choices for developing element matrices for vibration analyses. A quadratic tetrahedron mesh can be created by several meshing software packages (SolidWorks, MATLAB and etc). The elements are assumed to be isoparametric, and the tetrahedral coordinate system is utilized to describe arbitrary points within a tetrahedron element. The mapping between the isoparametric natural coordinates ξ_i and the actual coordinates of the tetrahedron element is given by

$$\begin{Bmatrix} 1 \\ x \\ y \\ z \end{Bmatrix} = \begin{bmatrix} 1 & 1 & 1 & 1 & \cdots & 1 \\ x_1 & x_2 & x_3 & x_4 & \cdots & x_{10} \\ y_1 & y_2 & y_3 & y_4 & \cdots & y_{10} \\ z_1 & z_2 & z_3 & z_4 & \cdots & z_{10} \end{bmatrix} \begin{Bmatrix} N_1 \\ N_2 \\ \vdots \\ N_{10} \end{Bmatrix} \tag{2.13}$$

where the shape functions are defined by

$$N_i = \xi_i(2\xi_i - 1)\ for\ i = 1{\sim}4$$

$$N_5 = 4\xi_1\xi_2, N_6 = 4\xi_2\xi_3, N_7 = 4\xi_3\xi_1, N_8 = 4\xi_1\xi_4, \tag{2.14}$$

$$N_9 = 4\xi_2\xi_4, N_{10} = 4\xi_3\xi_4$$

Each element matrix is numerically integrated with 14 Gauss Quadrature points with 4 coordinates

$$\underline{K}^e = \sum_{k=1}^{p} w_k F(\xi_{1k}, \xi_{2k}, \xi_{3k}, \xi_{4k}) \tag{2.15}$$

where *p* is the number of Gauss quadrature integration points, ξ_{ik} is the *ith* direction coordinate of the *kth* Gauss quadrature integration point in the tetrahedral coordinate system, and w_k is the corresponding weight factor.

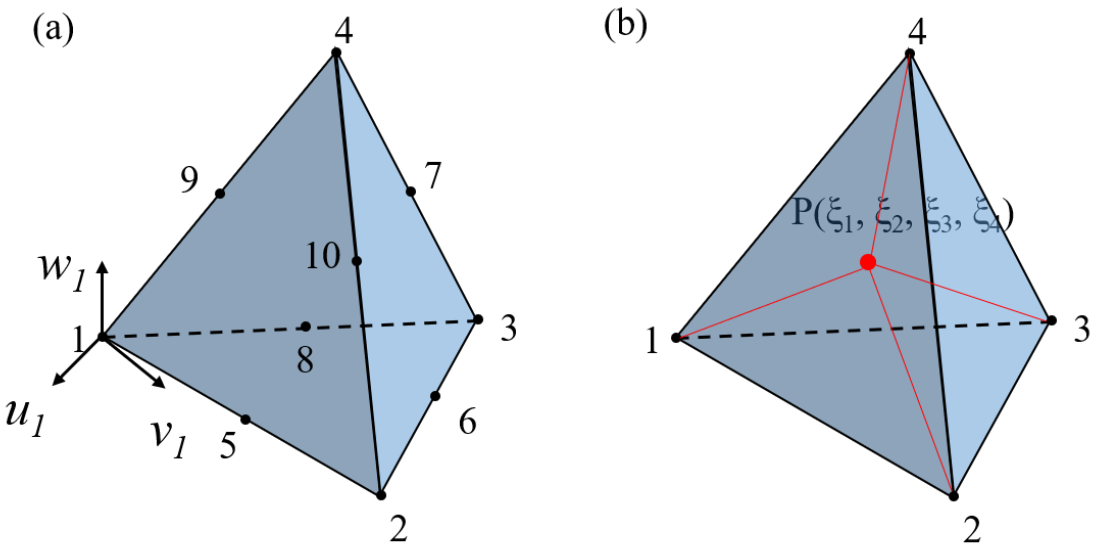

Figure 2.2 10-node quadratic isoparametric tetrahedron element (a) local 10 nodes of the element (b) the tetrahedral coordinate system

2.1.3. Bearing Model

The bearing coefficient matrices in the inertial coordinate system consist of four stiffness coefficients and four damping coefficients, which are defined as for bearing as

$$\underline{\boldsymbol{K}}_{b,i} = \begin{bmatrix} k_{b,xx} & k_{b,xy} \\ k_{b,yx} & k_{b,yy} \end{bmatrix} \tag{2.16}$$

$$\underline{\boldsymbol{C}}_{b,i} = \begin{bmatrix} c_{b,xx} & c_{b,xy} \\ c_{b,yx} & c_{b,yy} \end{bmatrix} \tag{2.17}$$

where $\underline{\boldsymbol{K}}_{b,i}$ and $\underline{\boldsymbol{C}}_{b,i}$ are the stiffness coefficient matrix and the damping coefficient matrix in the inertial coordinate system, respectively. An entry $k_{b,ij}$ of the stiffness

matrix indicates the bearing stiffness coefficient which exerts a force on the journal in the *i* direction due to the journal deflection in the *j* direction, in the inertial coordinate system. Similarly, $c_{b,ij}$ is the bearing damping coefficient defined in the same manner with respect to the journal velocity. The bearing stiffness matrix $\underline{\boldsymbol{K}}_{b,i}$ has to be transformed to the rotor-fixed coordinate system in order to assemble it with the rotor-fixed, shaft element matrices. Displacement and velocity vectors in the fixed, inertial x, y coordinates can be transformed to their counterparts in the rotating frame υ, η coordinates by pre-multiplying with the rotation matrix $\underline{\boldsymbol{R}}$

$$\underline{\boldsymbol{R}} = \begin{bmatrix} \cos \Omega t & \sin \Omega t \\ -\sin \Omega t & \cos \Omega t \end{bmatrix} \tag{2.18}$$

And the displacement and velocity vector in the fixed coordinates can also be expressed by the transposed rotation matrix

$$\begin{Bmatrix} \boldsymbol{x} \\ \boldsymbol{y} \end{Bmatrix} = \underline{\boldsymbol{R}}^{\boldsymbol{T}} \begin{Bmatrix} \boldsymbol{\zeta} \\ \boldsymbol{\eta} \end{Bmatrix} \tag{2.19}$$

$$\begin{Bmatrix} \dot{\boldsymbol{x}} \\ \dot{\boldsymbol{y}} \end{Bmatrix} = \underline{\boldsymbol{R}}^{\boldsymbol{T}} \begin{Bmatrix} \dot{\boldsymbol{\zeta}} \\ \dot{\boldsymbol{\eta}} \end{Bmatrix} + \underline{\dot{\boldsymbol{R}}}^{\boldsymbol{T}} \begin{Bmatrix} \boldsymbol{\zeta} \\ \boldsymbol{\eta} \end{Bmatrix} \tag{2.20}$$

The bearing force vector exerted by bearing damping and stiffness in the inertial frame can be represented as

$$\underline{\boldsymbol{F}}_{b,i} = \underline{\boldsymbol{C}}_{b,i} \begin{Bmatrix} \dot{x} \\ \dot{y} \end{Bmatrix} + \underline{\boldsymbol{K}}_{b,i} \begin{Bmatrix} x \\ y \end{Bmatrix} \tag{2.21}$$

The bearing force vector in the rotating frame can be obtained by pre-multiplying the rotation matrix $\underline{\boldsymbol{R}}$ to equation (2.21)

$$\begin{aligned} \underline{\boldsymbol{F}}_{b,r} = \underline{\boldsymbol{R}}\, \underline{F}_{b,i} &= \underline{\boldsymbol{R}} \left(\underline{\boldsymbol{C}}_{b,i} \begin{Bmatrix} \dot{x} \\ \dot{y} \end{Bmatrix} + \underline{\boldsymbol{K}}_{b,i} \begin{Bmatrix} x \\ y \end{Bmatrix} \right) \\ &= \underline{\boldsymbol{R}}\, \underline{\boldsymbol{C}}_{b,i} \left(\underline{\boldsymbol{R}}^T \begin{Bmatrix} \dot{\zeta} \\ \dot{\eta} \end{Bmatrix} + \underline{\dot{\boldsymbol{R}}}^T \begin{Bmatrix} \zeta \\ \eta \end{Bmatrix} \right) + \underline{\boldsymbol{R}}\, \underline{\boldsymbol{K}}_{b,i} \underline{\boldsymbol{R}}^T \begin{Bmatrix} \zeta \\ \eta \end{Bmatrix} \\ &= \underline{\boldsymbol{R}}\, \underline{\boldsymbol{C}}_{b,i} \underline{\boldsymbol{R}}^T \begin{Bmatrix} \dot{\zeta} \\ \dot{\eta} \end{Bmatrix} + \left(\underline{\boldsymbol{R}}\, \underline{\boldsymbol{C}}_{b,i} \underline{\dot{\boldsymbol{R}}}^T + \underline{\boldsymbol{R}}\, \underline{\boldsymbol{K}}_{b,i} \underline{\boldsymbol{R}}^T \right) \begin{Bmatrix} \zeta \\ \eta \end{Bmatrix} \end{aligned} \tag{2.22}$$

Therefore, the bearing coefficient matrices in the rotating frame can be defined by

$$\underline{\boldsymbol{C}}_{b,r} = \underline{\boldsymbol{R}} \cdot \underline{\boldsymbol{C}}_{b,i} \cdot \underline{\boldsymbol{R}}^T \tag{2.23}$$

$$\underline{\boldsymbol{K}}_{b,r} = \underline{\boldsymbol{R}} \cdot \underline{\boldsymbol{K}}_{b,i} \cdot \underline{\boldsymbol{R}}^T + \underline{\boldsymbol{R}} \cdot \underline{\boldsymbol{C}}_{b,i} \cdot \underline{\dot{\boldsymbol{R}}}^T \tag{2.24}$$

$$\underline{\boldsymbol{K}}_{b,r}(1,1) = \frac{k_{b,xx} + k_{b,yy}}{2} + \frac{k_{b,xx} - k_{b,yy}}{2}\cos 2\Omega t - \frac{k_{b,yx} + k_{b,xy}}{2}\sin 2\Omega t$$
$$+ \Omega\left(\frac{c_{b,xy} - c_{b,yx}}{2} + \frac{c_{b,xy} + c_{b,yx}}{2}\cos 4\Omega t\right.$$
$$\left. - \frac{c_{b,xx} - c_{b,yy}}{2}\sin 4\Omega t\right)$$

$$\underline{\boldsymbol{K}}_{b,r}(1,2) = \frac{k_{b,xy} - k_{b,yx}}{2} + \frac{k_{b,xy} + k_{b,yx}}{2}\cos 2\Omega t - \frac{k_{b,xx} - k_{b,yy}}{2}\sin 2\Omega t$$
$$+ \Omega\left(-\frac{c_{b,xx} + c_{b,yy}}{2} - \frac{c_{b,xx} - c_{b,yy}}{2}\cos 4\Omega t\right.$$
$$\left. - \frac{c_{b,xy} + c_{b,yx}}{2}\sin 4\Omega t\right)$$

$$\underline{\boldsymbol{K}}_{b,r}(2,1) = -\frac{k_{b,xy} - k_{b,yx}}{2} + \frac{k_{b,xy} + k_{b,yx}}{2}\cos 2\Omega t$$
$$- \frac{k_{b,xx} - k_{b,yy}}{2}\sin 2\Omega t$$
$$+ \Omega\left(\frac{c_{b,xx} + c_{b,yy}}{2} - \frac{c_{b,xx} - c_{b,yy}}{2}\cos 4\Omega t\right.$$
$$\left. - \frac{c_{b,xy} + c_{b,yx}}{2}\sin 4\Omega t\right) \tag{2.25}$$

$$\underline{\boldsymbol{K}}_{b,r}(2,2) = \frac{k_{b,xx} + k_{b,yy}}{2} - \frac{k_{b,xx} - k_{b,yy}}{2}\cos 2\Omega t - \frac{k_{b,xy} + k_{b,yx}}{2}\sin 2\Omega t$$
$$+ \Omega\left(\frac{c_{b,xy} + c_{b,yx}}{2} - \frac{c_{b,xy} + c_{b,yx}}{2}\cos 4\Omega t\right.$$
$$\left. + \frac{c_{b,xx} - c_{b,yy}}{2}\sin 4\Omega t\right)$$

$$\underline{\boldsymbol{C}}_{b,r}(1,1) = \frac{c_{b,xx} + c_{b,yy}}{2} + \frac{c_{b,xx} - c_{b,yy}}{2}\cos 2\Omega t - \frac{c_{b,yx} + c_{b,xy}}{2}\sin 2\Omega t$$

$$\underline{\boldsymbol{C}}_{b,r}(1,2) = \frac{c_{b,xy} - c_{b,yx}}{2} + \frac{c_{b,xy} + c_{b,yx}}{2}\cos 2\Omega t - \frac{c_{b,xx} - c_{b,yy}}{2}\sin 2\Omega t$$

$$\underline{\boldsymbol{C}}_{b,r}(2,1) = -\frac{c_{b,xy} - c_{b,yx}}{2} + \frac{c_{b,xy} + c_{b,yx}}{2}\cos 2\Omega t - \frac{c_{b,xx} - c_{b,yy}}{2}\sin 2\Omega t \tag{2.26}$$

$$\underline{\boldsymbol{C}}_{b,r}(2,2) = \frac{c_{b,xx} + c_{b,yy}}{2} - \frac{c_{b,xx} - c_{b,yy}}{2}\cos 2\Omega t - \frac{c_{b,xy} + c_{b,yx}}{2}\sin 2\Omega t$$

$\underline{\boldsymbol{K}}_{b,r}$ and $\underline{\boldsymbol{C}}_{b,r}$ contain time-varying coefficients with the minimum period $T_{min} = \pi/\Omega$ due to the coordinate system transformation. Therefore, the assembled system matrix differential equation

$$\underline{\boldsymbol{M}}\underline{\ddot{\boldsymbol{q}}}(t) + 2\Omega\underline{\boldsymbol{C}}(t)\underline{\dot{\boldsymbol{q}}}(t) + \underline{\boldsymbol{K}}(t)\underline{\boldsymbol{q}}(t) = \Omega^2\underline{\boldsymbol{f}}_c \tag{2.27}$$

also has time-periodic stiffness $\underline{\boldsymbol{K}}(t)$ and rate $\underline{\boldsymbol{C}}(t)$ matrices. Figure 2.3 illustrates how the bearings are attached to the rotor in the finite element model. Bearing nodes are distributed along the circumferential direction, and the shaft at the bearing location moves as rigid plane which is imposed via the use of constraint equations which force all degrees of freedom located on the cross section to remain in a plane after deformation.

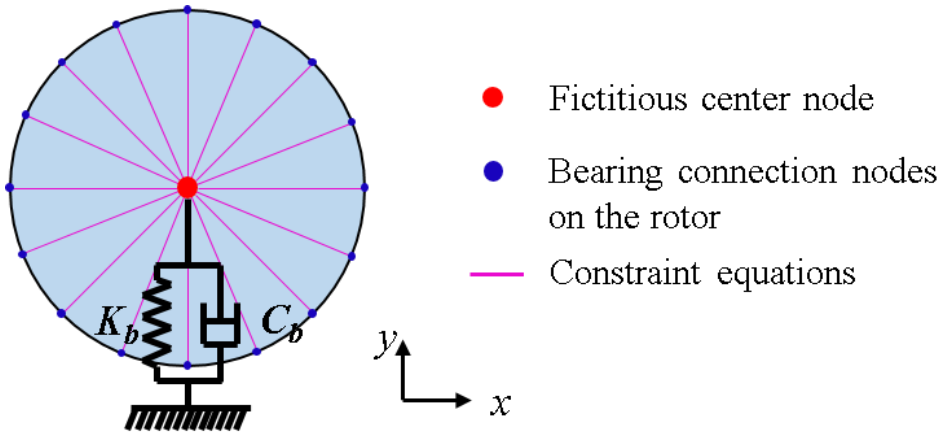

Figure 2.3 Bearing connection nodes in the finite element model

2.1.4. Model Reduction

A finite element model for a complex-shape, non-axisymmetric rotor requires a large number of dofs to include sufficient detail for its complex geometry. This large number of dofs has to be properly reduced in order to lessen the computational requirement. Guyan reduction [55] is utilized to reduce the size of the total system matrices, retaining only a certain portion of the total dofs. The selection of retained dofs is achieved by comparing mass-to-stiffness ratios of diagonal entries of the mass matrix and stiffness matrix as explained in [11]. A mass-to-stiffness ratio for *ith* dof can be represented as

$$R_i = \frac{\boldsymbol{M}_{ii}}{\boldsymbol{K}_{ii}} \tag{2.28}$$

Degrees of freedom dofs which are connected to the bearings may include time-varying coefficients and should always be retained. The model reduction yields the reduced matrix differential equation as

$$\underline{\boldsymbol{M}}^R \ddot{\underline{\boldsymbol{q}}}^R(t) + 2\Omega \underline{\boldsymbol{C}}^R(t) \dot{\underline{\boldsymbol{q}}}^R(t) + \underline{\boldsymbol{K}}^R(t) \underline{\boldsymbol{q}}^R(t) = \Omega^2 \underline{\boldsymbol{f}}_c^R \tag{2.29}$$

2.2. Parametric Vibration Stability Analysis

2.2.1. Floquet Theory

The reduced system matrix differential equation includes periodically varying coefficients in the stiffness and damping matrices. Time variation of the stiffness, mass or damping parameters causes parametric excitation and resulting parametric vibration. The theory that is used to evaluate the stability of systems governed by periodically varying coefficients is referred to as Floquet theory [54]. The form of equation (2.29) with external force terms removed may be written in first-order (state-space) form as

$$\dot{\underline{\boldsymbol{X}}}(t) = \underline{\boldsymbol{B}}(t)\, \underline{\boldsymbol{X}}(t) \tag{2.30}$$

where the periodic time-varying coefficient matrix $\underline{\boldsymbol{B}}(t)$ is

$$\underline{\boldsymbol{B}}(t) = \begin{bmatrix} \underline{\mathbf{0}}_N & \underline{\boldsymbol{I}}_N \\ -\left(\underline{\boldsymbol{M}}^R\right)^{-1} \underline{\boldsymbol{K}}^R(t) & -2\Omega \left(\underline{\boldsymbol{M}}^R\right)^{-1} \underline{\boldsymbol{C}}^R(t) \end{bmatrix} \tag{2.31}$$

$$\underline{\boldsymbol{B}}(t + T_{min}) = \underline{\boldsymbol{B}}(t) \tag{2.32}$$

T_{min} is the minimum period of $\underline{\boldsymbol{B}}(t)$, and N is the number of retained dofs. The Matrizant matrix $\underline{\boldsymbol{\Phi}}_{\boldsymbol{M}}(t)$ satisfies

$$\dot{\underline{\boldsymbol{\Phi}}}_{\boldsymbol{M}}(t) = \underline{\boldsymbol{B}}(t)\underline{\boldsymbol{\Phi}}_{\boldsymbol{M}}(t) \tag{2.33}$$

$$\underline{\boldsymbol{\Phi}}_{\boldsymbol{M}}(t_0) = \underline{\boldsymbol{I}}_{2N} \tag{2.34}$$

where $\underline{\boldsymbol{I}}_{2N}$ is the identity matrix of size $2N$. The Monodromy matrix is then obtained from

$$\underline{\boldsymbol{H}}_{\boldsymbol{M}} = \underline{\boldsymbol{\Phi}}_{\boldsymbol{M}}(T_{min}) \tag{2.35}$$

The Monodromy matrix is obtained by evaluating the Matrizant matrix at T_{min}, and $\underline{\boldsymbol{H}}_{\boldsymbol{M}}$ is a numerical matrix by virtue of its evaluation at T_{min}. The stability of the system can be evaluated by considering the magnitude of the *kth* eigenvalue λ_{mk} of $\underline{\boldsymbol{H}}_{\boldsymbol{M}}$. The system is asymptotically stable if $|\lambda_{mk}| < 1$ for all k, asymptotically unstable if $|\lambda_{mk}| > 1$ for any k and marginally stable if $|\lambda_{mk}| = 1$ for any k and $|\lambda_{mk}| < 1$ for all $j \neq k$.

2.2.2. Hsu's Method

The numerical integration based solution for $\underline{\boldsymbol{H}}_{\boldsymbol{M}}$ via (2.33) – (2.35), may take an excessive amount of computer time for systems with time-varying $\underline{\boldsymbol{B}}(t)$ and a large number of dofs. Hsu [31] developed an approximate method to efficiently obtain $\underline{\boldsymbol{H}}_{\boldsymbol{M}}$, by dividing the period *T* into small intervals, and then assume that $\underline{\boldsymbol{B}}(t)$ is approximately constant within each interval. The piecewise constant coefficient matrix $\underline{\boldsymbol{B}}_k$ is obtained from

$$\underline{\boldsymbol{B}}_k = \frac{1}{\Delta_k}\int_{t_{k-1}}^{t_k} \underline{\boldsymbol{B}}(s)ds \tag{2.36}$$

Then the discretized Monodromy matrix is obtained from

$$\underline{\boldsymbol{H}}_{\boldsymbol{M}}(K) = \underline{\boldsymbol{I}}_N exp\left(\Delta_K \underline{\boldsymbol{B}}_K\right) exp\left(\Delta_{K-1}\underline{\boldsymbol{B}}_{K-1}\right)\cdots exp\left(\Delta_1 \underline{\boldsymbol{B}}_1\right) \tag{2.37}$$

A matrix exponential of a constant coefficient matrix has a constant matrix solution, and each solution is independent of the others in (2.37). Hence, the discretized Monodromy matrix can be integrated with multiple parallel computing processors. Utilizing parallel processing improves computation speed significantly.

2.3. Illustration and Validation

2.3.1. Asymmetric Rectangular Cross Section Rotor Supported by Isotropic Bearings

The parametrically excited, rectangular cross section Jeffcott rotor analyzed in [2] is examined as a validation step for the proposed method. The homogeneous equation of motion for a Jeffcott rotor with asymmetric shaft stiffness and rigid bearings is written in the rotor-fixed coordinate system as

$$\begin{bmatrix} m & 0 \\ 0 & m \end{bmatrix} \begin{Bmatrix} \ddot{q}_\upsilon \\ \ddot{q}_\eta \end{Bmatrix} + \begin{bmatrix} 2(c_r + c_e) & -2\Omega m \\ 2\Omega m & 2(c_r + c_e) \end{bmatrix} \begin{Bmatrix} \dot{q}_\upsilon \\ \dot{q}_\eta \end{Bmatrix} + \begin{bmatrix} k_\upsilon - m\Omega^2 & -c_e\Omega \\ c_e\Omega & k_\eta - m\Omega^2 \end{bmatrix} \begin{Bmatrix} q_\upsilon \\ q_\eta \end{Bmatrix} = 0 \tag{2.38}$$

where m, c_r, c_e, Ω, k_υ and k_η are the point mass, the rotor internal damping, the external damping, the spin speed of the rotor, the rotor stiffness along the υ-axis and the rotor stiffness along the η-axis, respectively. Equation (2.38) is written in simplified form as

$$\begin{Bmatrix} \ddot{q}_\upsilon \\ \ddot{q}_\eta \end{Bmatrix} + \begin{bmatrix} 2\zeta\bar{\lambda} & -2\Omega \\ 2\Omega & 2\zeta\bar{\lambda} \end{bmatrix} \begin{Bmatrix} \dot{q}_\upsilon \\ \dot{q}_\eta \end{Bmatrix} + \begin{bmatrix} \bar{\lambda}^2(1+q) - \Omega^2 & -2\zeta_e\bar{\lambda}\Omega \\ 2\zeta_e\bar{\lambda}\Omega & \bar{\lambda}^2(1-q) - \Omega^2 \end{bmatrix} \begin{Bmatrix} q_\upsilon \\ q_\eta \end{Bmatrix} = 0 \tag{2.39}$$

where $\bar{\lambda}^2 = \left(k_\upsilon + k_\eta\right)/2m$, $q = \left(k_\upsilon - k_\eta\right)/2m\bar{\lambda}^2$, $\zeta_e = c_e/2m\bar{\lambda}$, $\zeta_r = c_r/2m\bar{\lambda}$, $\zeta = \zeta_r + \zeta_e$

The characteristic equation of equation for (2.39) is

$$\bar{s}^4 + 4\zeta\bar{s}^3 + 2(1 + 2\zeta^2 + \bar{\Omega}^2)\bar{s}^2 + 4[\zeta + (\zeta_e - \zeta_r)\bar{\Omega}^2]\bar{s} + [(\bar{\Omega}^2 - 1)^2 + 4\zeta_e\bar{\Omega}^2 - q^2] = 0 \tag{2.40}$$

where $\bar{\Omega} = \Omega/\bar{\lambda}$, $\bar{s} = s/\bar{\lambda}$. Application of the Routh-Hurwitz stability criteria to the roots of equation (2.40) yields the following stability criteria:

$$\begin{aligned} &\zeta + (\zeta_e - \zeta_r)\bar{\Omega}^2 > 0, \\ &-(\zeta_r/\zeta)^2\bar{\Omega}^4 + (1 - \zeta_r^2)\bar{\Omega}^2 + \zeta^2 - (q/2)^2 > 0, \\ &(\bar{\Omega}^2 - 1)^2 + 4\zeta_e^2\underline{\Omega}^2 - q^2 > 0 \end{aligned} \tag{2.41}$$

The first two conditions of equation (2.41) determine instability due to internal damping, and the last condition determines instability by parametric excitation due to the rotor asymmetry q. For undamped systems, the instability criteria from the last condition of equation (2.41) becomes

$$\begin{aligned} &\lambda_\upsilon < \Omega < \lambda_\eta \\ &where\ \lambda_\upsilon^2 = \lambda^2(1 - q) = k_\upsilon/m \\ &and\ \lambda_\eta^2 = \lambda^2(1 + q) = k_\eta/m \\ &and\ (k_\eta > k_\upsilon) \end{aligned} \tag{2.42}$$

Thus, the undamped asymmetric rotor will be unstable at running speeds between the undamped natural frequencies in the υz and ηz planes. These results are utilized as a validation step for the proposed general, numerical approach using Hsu's approximation for the Monodromy matrix. The asymmetry of the rectangular cross section rotor with height h and width w is characterized by

$$q_r = abs\left(\frac{h-w}{h+w}\right) \tag{2.43}$$

The rotor spins about the z-axis at the constant spin speed Ω. An 8-coefficient bearing model is included at each end of the rotor. The Young's modulus and Poisson's ratio of the model are 200 GPa and 0.3, respectively. A mesh convergence study was conducted for the four lowest natural frequencies of the rotor with the rotor asymmetry $q_r = 0.1$. The results are plotted in Figure 2.4. The rotor mesh density was then selected to be within the range for which the four lowest natural frequencies are well converged. Figure 2.5 shows the rotor mesh for q_r= 0.1, including 12,262 elements and 19,935 nodes, with 59,805 dof. The monodromy matrix in (2.35) is of order twice the number of retained degrees of freedom, which would equal 119,610 without Guyan reduction. This is excessive from a computation time perspective therefore Guyan reduction must be applied. The retained degrees of freedom include all degree of freedom that have time varying stiffness or damping terms plus those with the largest R_i ratios in (2.28). A study is conducted utilizing the 4 lowest undamped natural frequencies of the non-spinning rotor as a measure of convergence with respect to increasing the number of retained

degrees of freedom. Figure 2.6 shows the four lowest undamped natural frequencies vs. the number of the retained dofs. The graph shows steep drops of two of these frequencies at 40 and 50 dof and then the frequencies converge. The converged values for the undamped natural frequencies are listed Table 2.1.

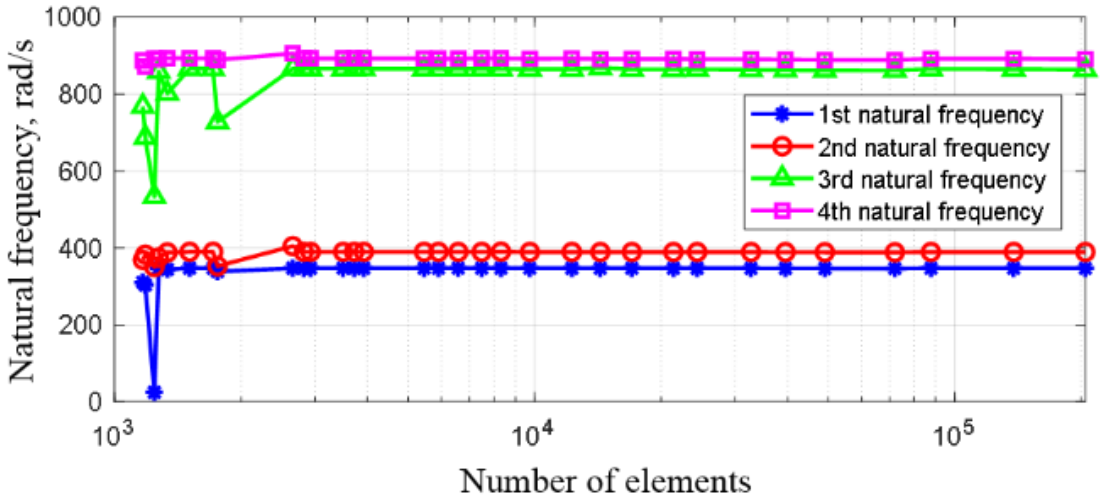

Figure 2.4 Undamped natural frequencies of the rectangular rotor-bearing system (q_r= 0.1) vs. number of elements

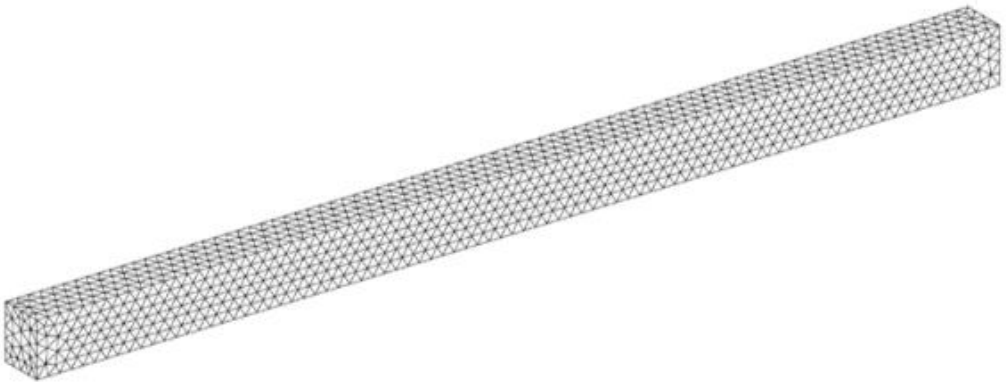

Figure 2.5 Mesh for the asymmetric rectangular rotor with q_r = 0.1

Table 2.1 Undamped natural frequencies of asymmetric non-spinning rotors

q_r	Modes	υz plane	ηz plane
0.01	1st bending mode	367 rad/s	371 rad/s
	2nd bending mode	878 rad/s	879 rad/s
0.05	1st bending mode	358 rad/s	380 rad/s
	2nd bending mode	871 rad/s	884 rad/s
0.10	1st bending mode	347 rad/s	390 rad/s
	2nd bending mode	864 rad/s	892 rad/s

Convergence on natural frequencies is neither a necessary nor a sufficient condition for convergence on monodromy matrix eigenvalues, and ultimately on prediction of parametric excitation instabilities.

Figure 2.7 shows the maximum magnitude eigenvalue λ_{mk} of the monodromy matrix $\underline{\boldsymbol{H}}_M$ through an unstable speed range for various values of the number of retained degrees. For the preceding example, only 0.1% of the total number of system degrees of freedom needed to be retained for converged results to occur. The effect of rotor asymmetry on parametric stability is clearly presented in Figure 2.8. As expected the undamped spinning rotor is marginally stable over the entire speed range when q_r = 0.0 (no asymmetry). The unstable speed ranges appear in the vicinities of Ω = 370 rad/s and Ω = 880 rad/s for the rotor asymmetry greater than 0, and the width of each unstable speed range becomes larger as the rotor asymmetry increases. These results are consistent with eq. (2.42) and the natural frequencies in Table 2.1. The first and second bending modes occur in the spin speed range in Figure 2.8. The unstable speed ranges are seen to occur between the undamped natural frequencies in the xz plane and the yz plane for both first and second bending modes, consistent with equation (2.42). Gyroscopic effects are negligible for this example.

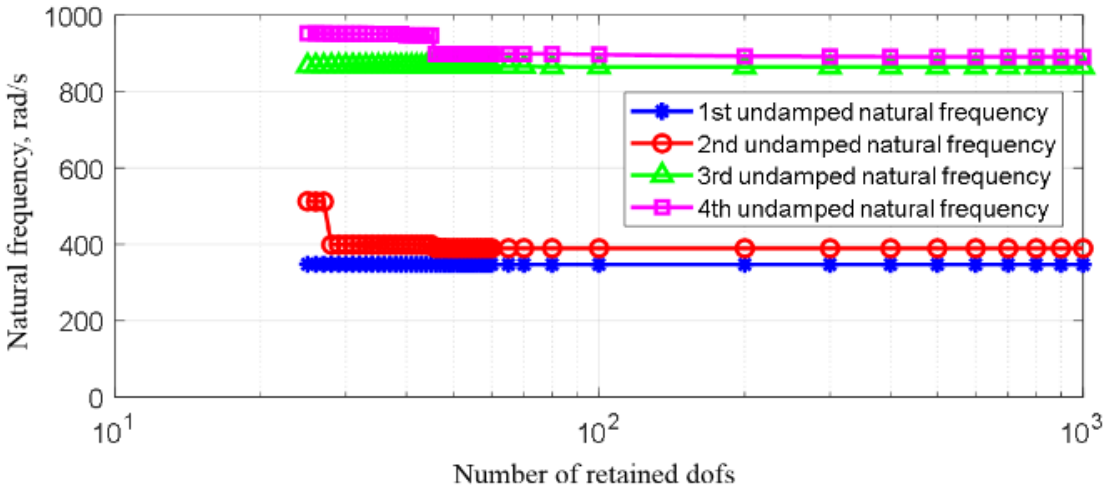

Figure 2.6 The four lowest undamped natural frequencies of the rotor-bearing system (for q_r=0.1) versus the number of the retained dofs

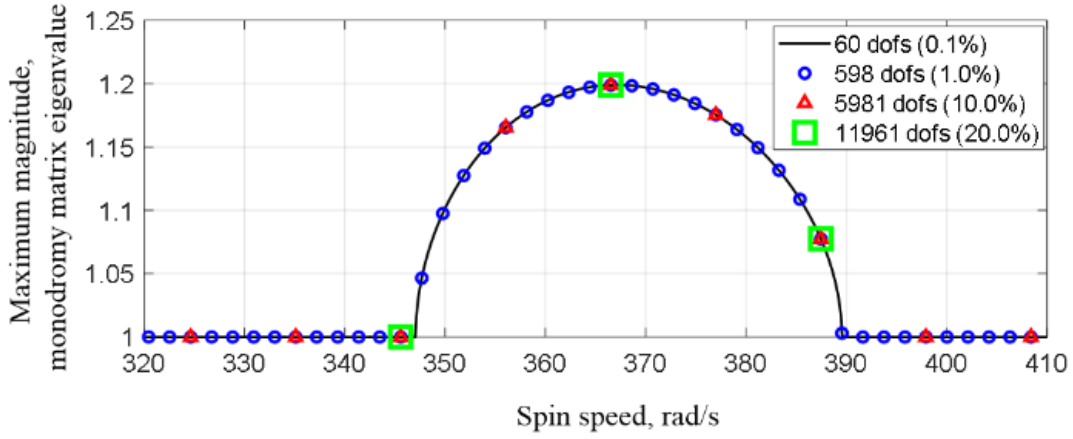

Figure 2.7 Maximum magnitude, monodromy matrix eigenvalue vs. spin speed for various numbers of retained dofs.

2.3.2. Asymmetric Rectangular Rotors with Asymmetric Bearings

The bearing asymmetry parameter q_b is defined as

$$q_b = abs\left(\frac{k_{b,xx} - k_{b,yy}}{k_{b,xx} + k_{b,yy}}\right) \tag{2.44}$$

where $k_{b,xx}$ and $k_{b,yy}$ are the bearing stiffness in the x-axis and the y-axis of the inertial coordinate system, respectively. Figure 2.9 illustrates the unstable spin speed ranges of the rotor-bearing system with q_r = 0.1 for the four different levels of the bearing asymmetry. The first unstable speed range (346 rad/s ≤ Ω ≤ 390 rad/s) corresponding to the first bending modes is nearly invariant with respect to bearing asymmetry. The second unstable speed range (864 rad/s ≤ Ω ≤ 892 rad/s) corresponding to the second bending modes splits into the three parts with increasing bearing asymmetry. The unstable range separates into 3 distinct unstable sub-ranges, and increases in total width by 60% as q_b increases from 0 to 0.1. In addition, the overall magnitude of the maximum eigenvalue for each unstable range decreases as q_b increases. The instability criterion from the analytical approach in equation (2.42) is not applicable for asymmetric rotors with asymmetric bearings. Instead a time-transient, numerical integration [9] is performed to identify stable and unstable speed ranges. The Runge-Kutta method is applied to equation (2.29), with q_r = 0.1, to obtain nodal displacements and velocities vs. time. Figure 2.10 (a) and (b) show the y displacement at the bearing location vs. number of revolutions at five different spin speeds: Ω = 885 rad/s and Ω = 911 rad/s. The

system is marginally stable at Ω = 911 rad/s, and unstable at Ω = 885 rad/s, in agreement with the Floquet stability result in Figure 2.9. Comparison between $q_b = 0$ and $q_b = 0.1$ in Figure 2.9 shows that the unstable speed ranges of the asymmetric rotor may shift due to bearing asymmetry. For example, the system is unstable at Ω = 885 rad/s, and stable at Ω = 911 rad/s with zero bearing asymmetry q_b = 0. This is reversed when the bearing asymmetry is increased to q_b = 0.1. The latter case results are verified by direct time-transient, numerical integration as presented in Figure 2.10 (c) and (d). The system is stable at Ω = 885 rad/s and unstable at Ω = 911 rad/s, consistent with Figure 2.9.

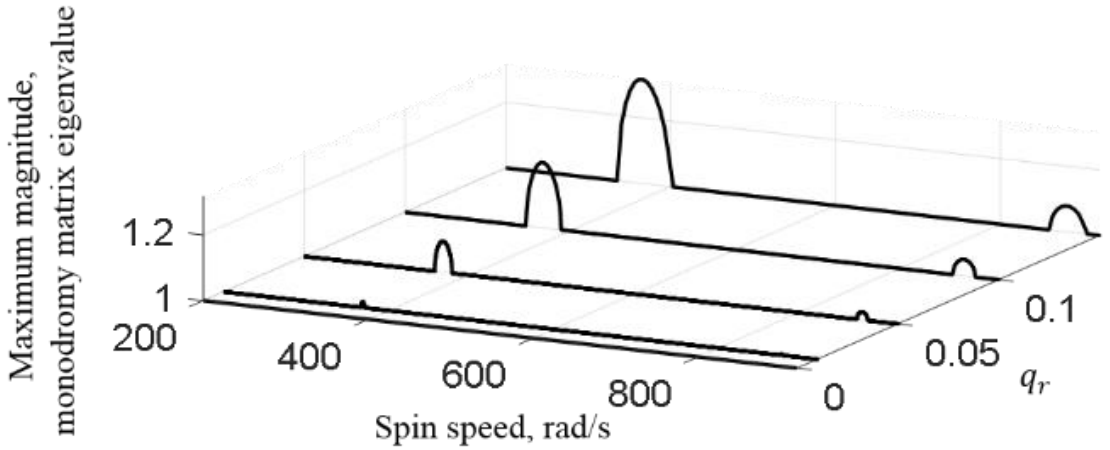

Figure 2.8 Maximum magnitude, monodromy matrix eigenvalue vs. spin speed vs. q_r

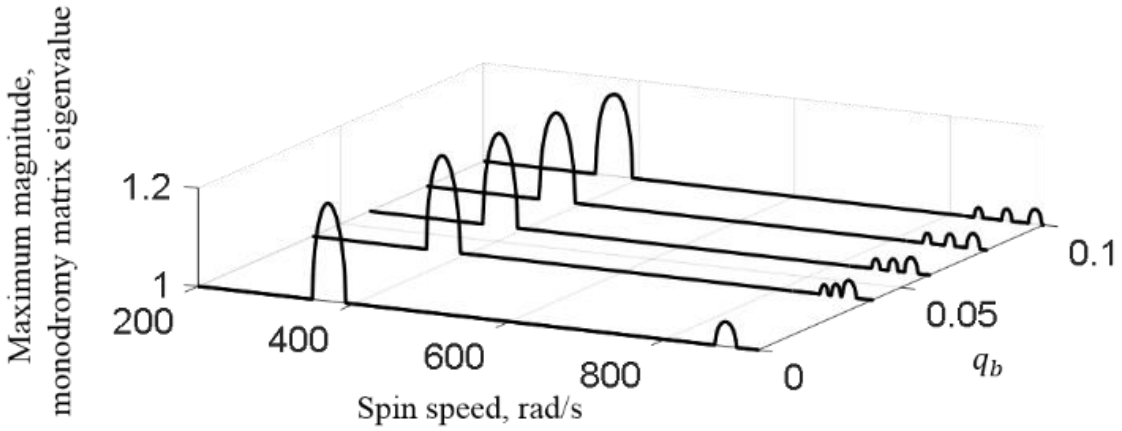

Figure 2.9 Maximum magnitude, monodromy matrix eigenvalue vs. spin speed vs. q_b for the rectangular rotor-bearing system (q_r= 0.1)

2.3.3. Damping Effects on the Stability of an Asymmetric Rotor-Bearing System

The addition of external damping to conventional undamped rotor models without rotor asymmetry, will always improve stability. Likewise, the addition of external damping to a rotor model with rotor asymmetry also mitigates parametric excitation instability. Bearings are generally the main source of external damping in rotor-bearing systems [2]. The bearing damping coefficient matrix in the rotor-fixed coordinate system $\underline{C}_{b,r}$ was derived from the bearing damping matrix in the inertia coordinate system $\underline{C}_{b,i}$ in equation (2.17). For sake of simplicity the bearing damping $\underline{C}_{b,i}$ is assumed to be isotropic without cross-coupled damping terms, i.e. $c_{b,xx} = c_{b,yy} = c_{b,n}$ and $c_{b,xy} = c_{b,yx} = 0$. Hence by (2.17) and (2.23),

$$\underline{\boldsymbol{C}}_{b,i} = \underline{\boldsymbol{C}}_{b,r} = c_{b,n}\underline{I}_2 \tag{2.45}$$

Define the damping ratio ζ as

$$\zeta = \frac{c_E}{2\sqrt{m_r k_E}} \tag{2.46}$$

where c_E, m_r and k_E are the equivalent bearing damping coefficient, the rotor mass and the equivalent bearing stiffness coefficient, respectively. For example, the damping ratio, ζ = 10% can be calculated by considering c_E = 7.2 e3 N/(m/s), m_r= 65.154 kg, and k_E = 2.0 e^7 N/m. Figure 2.11 shows the maximum magnitude, monodromy matrix eigenvalue vs. spin speed for the case of q_r = 0.1 and q_b = 0.0. Results are shown for various

damping ratios. The inclusion of ζ = 10% external damping has the effects of decreasing the intensity and speed range of the 1st mode instability, and completely eliminating the 2nd mode instability range. Similarly, the 1st mode instability range is completely eliminated when ζ = 30%. The stabilizing effect of bearing damping can also be verified by the direct time-transient integration method. Figure 2.10 (e) shows the y direction response of a nodal displacement at the bearing location with bearing damping ζ = 30%, for a spin speed: Ω = 885 rad/s. The bearing damping causes the nodal displacements to converge to zero.

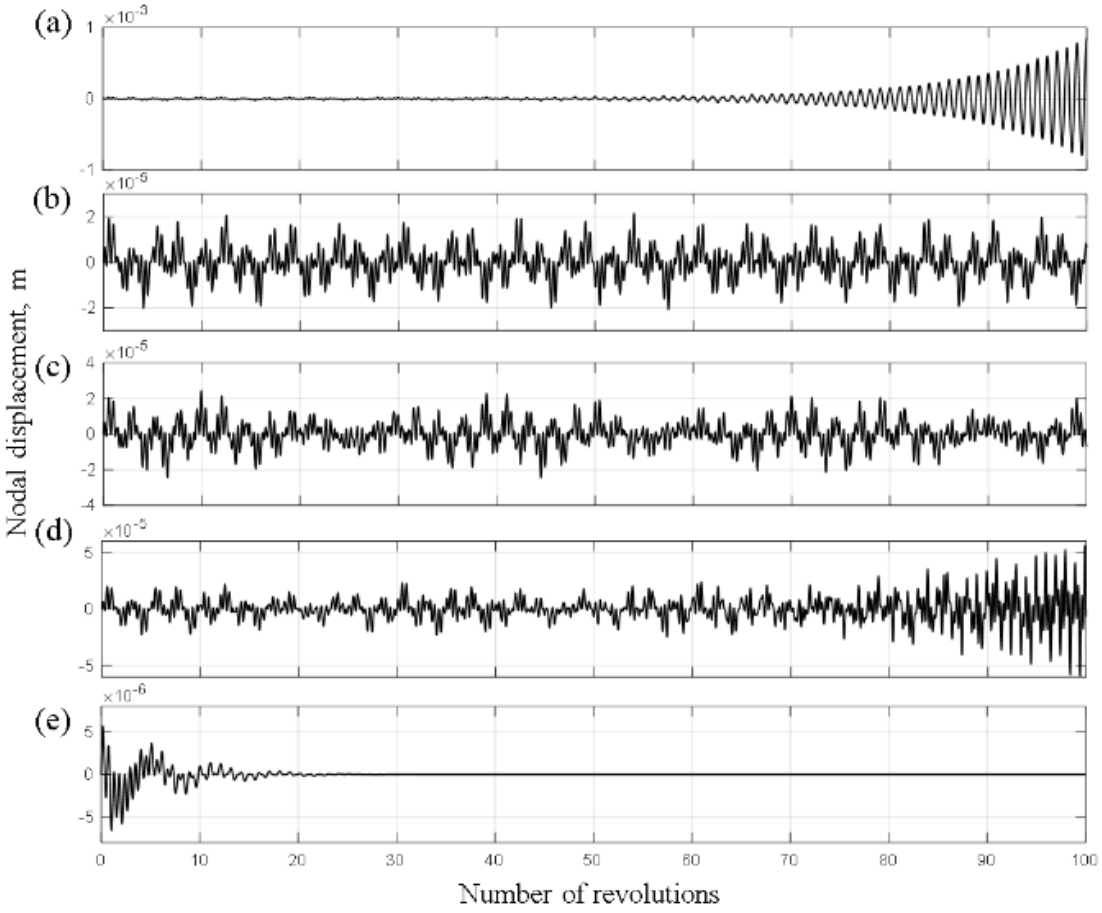

Figure 2.10 y displacement at the bearing location vs. time (a) q_r = 0.1, q_b = 0.0, Ω = 885 rad/s, (b) q_r = 0.1, q_b = 0.0, Ω = 911 rad/s, (c) q_r = 0.1, q_b = 0.1, Ω = 885 rad/s, (d) q_r = 0.1, q_b = 0.1, Ω = 911 rad/s, (e) , (d) q_r = 0.1, q_b = 0.0, ζ = 0.3, Ω = 885 rad/s

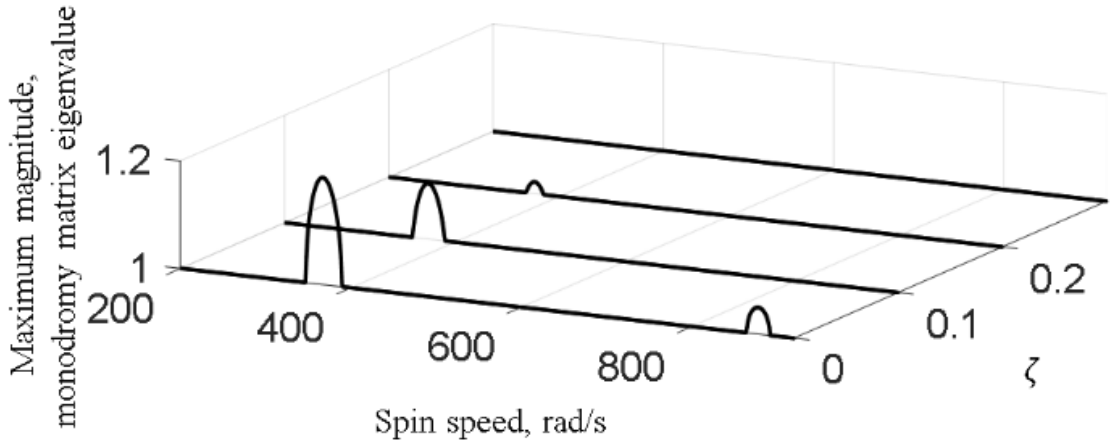

Figure 2.11 Maximum magnitude, monodromy matrix eigenvalue vs. spin speed with (q_r = 0.1, q_b = 0.0) vs. ζ

2.4. Computation speed enhancement

Demands for longer, more lightweight and more geometrically complex rotors have produced a need for higher fidelity structural models that include very large numbers of dofs. The stability evaluation approach presented here is highly efficient and benefits from Hsu's approach being amenable to discretization and parallelization. Hsu's approximate evaluation of (2.33) – (2.35) is accurate as demonstrated by the results shown in Figure 2.12. The "without Hsu" approach corresponds with numerically integrating the full set of equation in (2.33) – (2.35) without assumptions or approximations. The "with Hsu" approach follows the approximate evaluation of the monodromy system matrix outlined in (2.36) and (2.37).

Figure 2.13 shows plots of the ratio of computation time for full numerical integration of (2.33) – (2.35) divided by time to evaluate the monodromy matrix with Hsu's approach. Hsu's method without parallel-processing is 100 times faster than the conventional Floquet method. Parallelization with Hsu's approach further improves computational efficiency so that the ratio becomes 400 or more. A 12-core computing system is utilized for the parallel-processing. The computation speed improvement by the parallel-processing becomes more effective as the number of dofs increases.

Figure 2.13 (b) shows the corresponding ratio of full Floquet to Hsu approach for the maximum magnitude, Monodromy matrix eigenvalue. This comparison indicates the relative error by the Hsu approximation is less than 0.0001%.

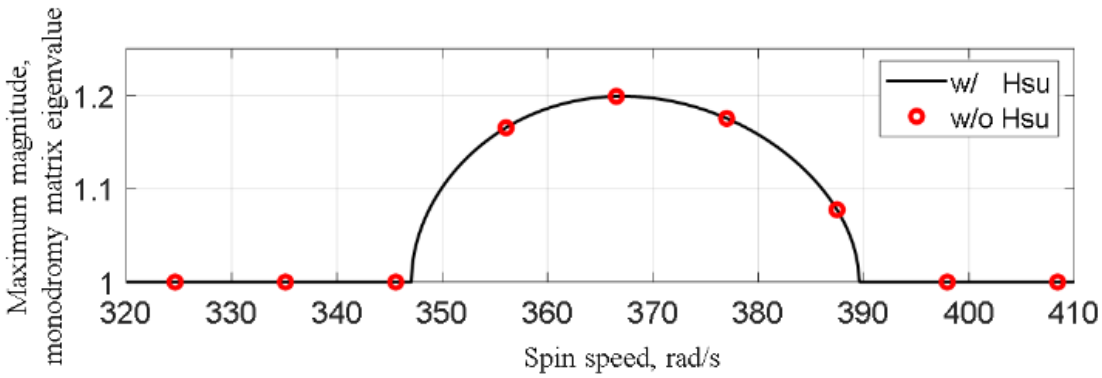

Figure 2.12 Maximum magnitude, monodromy matrix eigenvalue vs. spin speed with (q_r = 0.1, q_b = 0.0) for with and without Hsu's method

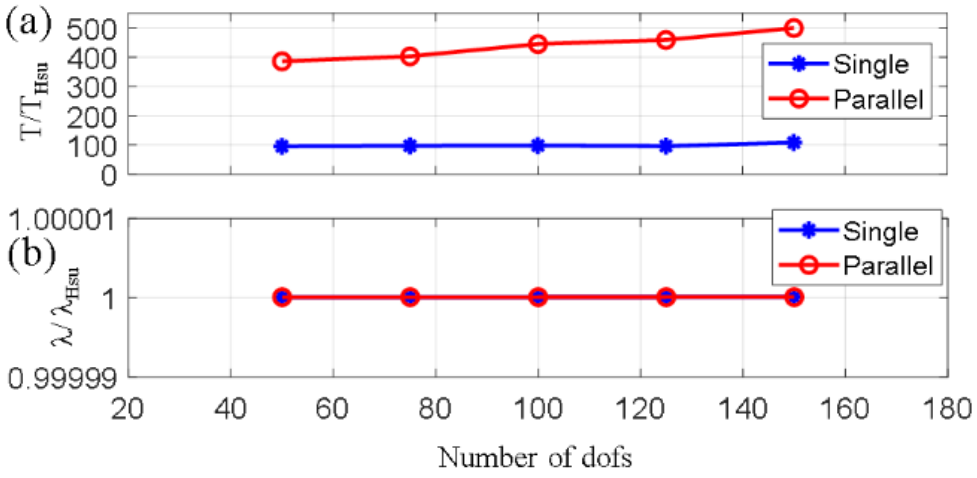

Figure 2.13 Computation speed comparison for the rotor-bearing system (q_r = 0.1, q_b = 0.0)

2.5. Comparison between the proposed method and Hill's method

References [26, 13, 29] utilize Hill's method to predict instabilities of non-axisymmetric rotor bearing systems. The method is briefly summarized in this section. According to Floquet theory, a solution of the homogeneous form of (2.29) has the form [29, 56]

$$\underline{p}(t) = \underline{p_n}(t)e^{\alpha t} \tag{2.47}$$

where $p_n(t)$ is a periodic function of time with period T_{min} and α_F is a Floquet exponent. The unknown periodic function $p_n(t)$ can be expressed by the general Fourier series

$$\underline{p_n}(t) = \sum_{j=-\infty}^{j=\infty} \underline{p_j} e^{ij2\Omega t} \tag{2.48}$$

Substituting (2.47) and its derivatives into the homogeneous form of (2.29), yields an infinite set of algebraic equations for the unknown terms in (2.48) which can be stated in matrix form as

$$\begin{bmatrix} \ddots & \vdots & \vdots & \vdots & \vdots & \vdots & \iddots \\ \cdots & \underline{A}_{-2} & \underline{B} & & & & \cdots \\ \cdots & \underline{C} & \underline{A}_{-1} & \underline{B} & & & \cdots \\ \cdots & & \underline{C} & \underline{A}_{0} & \underline{B} & & \cdots \\ \cdots & & & \underline{C} & \underline{A}_{+1} & \underline{B} & \cdots \\ \cdots & & & & \underline{C} & \underline{A}_{+2} & \cdots \\ \iddots & \vdots & \vdots & \vdots & \vdots & \vdots & \ddots \end{bmatrix} \begin{Bmatrix} \vdots \\ p_{-2} \\ p_{-1} \\ p_0 \\ p_{+1} \\ p_{+2} \\ \vdots \end{Bmatrix} = \begin{Bmatrix} \vdots \\ 0 \\ 0 \\ 0 \\ 0 \\ 0 \\ \vdots \end{Bmatrix} \tag{2.49}$$

where $\underline{\boldsymbol{A}}_j = -\underline{\boldsymbol{M}}^R(\boldsymbol{\alpha}^2 + \mathbf{4}\boldsymbol{j\Omega} + \mathbf{4}\boldsymbol{j}^2\boldsymbol{\Omega}^2) + \underline{\boldsymbol{C}}^R(\boldsymbol{\alpha} + \mathbf{2}\boldsymbol{j\Omega})\boldsymbol{i} + \underline{\boldsymbol{K}}_0^R$, $\underline{\boldsymbol{B}} = \left(\underline{\boldsymbol{K}}_{\boldsymbol{c}}^R + \boldsymbol{i}\underline{\boldsymbol{K}}_{\boldsymbol{s}}^R\right)/\mathbf{2}$, $\underline{\boldsymbol{C}} = \left(\underline{\boldsymbol{K}}_{\boldsymbol{c}}^R - \boldsymbol{i}\underline{\boldsymbol{K}}_{\boldsymbol{s}}^R\right)/\mathbf{2}$. $\underline{\boldsymbol{K}}_0^R$, $\underline{\boldsymbol{K}}_{\boldsymbol{c}}^R$, and $\underline{\boldsymbol{K}}_{\boldsymbol{s}}^R$ are the coefficient matrix of the constant term, the coefficient matrix of the cosine term and the coefficient matrix of the sine term of the reduced stiffness matrix $\underline{\boldsymbol{K}}^R$, respectively. The determinant associated with (2.49) is called Hill's infinite determinant, and an eigenproblem linked with it can be used to predict the stability of periodically time-varying systems. Approximate solutions for the eigenproblem can be obtained by truncating the matrix in Equation (2.49). The maximum value of j, j_{max} is the truncation number and it has to be determined properly for an accurate solution. In the prior research [26, 13, 29], various values of j_{max} have been used in the range from 2 to 5. Parametrically excited Jeffcott rotor models both in the inertial coordinate system and in the rotor-fixed coordinate system [57] were presented to verify applications of Hill's method. The equation of motion of the Jeffcott rotor model in the inertial coordinate system can be written

$$
\begin{aligned}
&m\ddot{x} + (c_r + c_b)\dot{x} + \left(\overline{k_\iota} + k_x + {k_i}' \cos 2\Omega t\right)x + (c_r\Omega + {k_i}' \sin 2\Omega t)y \\
&\qquad = m\Omega^2 a \cos \Omega t \\
&m\ddot{y} + (c_r + c_b)\dot{y} + \left(\overline{k_\iota} + k_y + {k_i}' \cos 2\Omega t\right)y + (c_r\Omega + {k_i}' \sin 2\Omega t)x \\
&\qquad = m\Omega^2 a \sin \Omega t
\end{aligned}
\tag{2.50}
$$

where $\overline{k_\iota} = \frac{k_\upsilon + k_\eta}{2}, {k_i}' = \frac{k_\upsilon - k_\eta}{2}$. Equation (2.50) can be transformed into the rotor-fixed coordinate system as

$$
\begin{aligned}
&m\ddot{\upsilon} + (c_r + c_b)\dot{\upsilon} + \left(\overline{k_r} + k_\upsilon + {k_r}' \cos 2\Omega t - m\Omega^2\right)\upsilon - 2m\Omega\dot{\eta} \\
&\qquad - (c_b\Omega + {k_r}' \sin 2\Omega t)\eta = m\Omega^2 a \\
&m\ddot{\eta} + (c_r + c_b)\dot{\eta} + \left(\overline{k_r} + k_\eta - {k_r}' \cos 2\Omega t - m\Omega^2\right)\eta + 2m\Omega\dot{\upsilon} \\
&\qquad + (c_b\Omega - {k_r}' \sin 2\Omega t)\upsilon = 0
\end{aligned}
\tag{2.51}
$$

where $\overline{k_r} = \frac{k_x + k_y}{2}, {k_r}' = \frac{k_x - k_y}{2}$, m = 75.8 kg, $cr = cb$ = 0, k_υ = 1.25e^6 N/m, k_η = 5.0e^6 N/m, k_x = 1.0e^7, k_y = 1.0e^6. Figure 2.14 shows the results from instability prediction from both Hill's method and Hsu's method in both reference frames. The convergence of Hill's method is achieved by j_{max} = 2. Hill's method in the rotor-fixed coordinate system predicts instabilities in the speed ranges around Ω = 180 rad/s and from Ω = 200 rad/s to Ω = 340 rad/s, whereas unstable speed ranges determined by Hsu's methods are from Ω = 200 rad/s to Ω = 253 rad/s and from Ω = 300 rad/s to Ω = 340 rad/s. Time-transient, numerical integration is performed to verify the results. Figure 2.15 shows the

nodal displacements in the x-axis vs. number of revolutions at rotor spin speeds: Ω = 220 rad/s, Ω = 280 rad/s and Ω = 320 rad/s. The system is marginally stable only when Ω = 280 rad/s, hence, the results imply that Hill's method in the rotor-fixed coordinate system inaccurately predicts at the speed range from Ω = 253 rad/s to Ω = 300 rad/s.

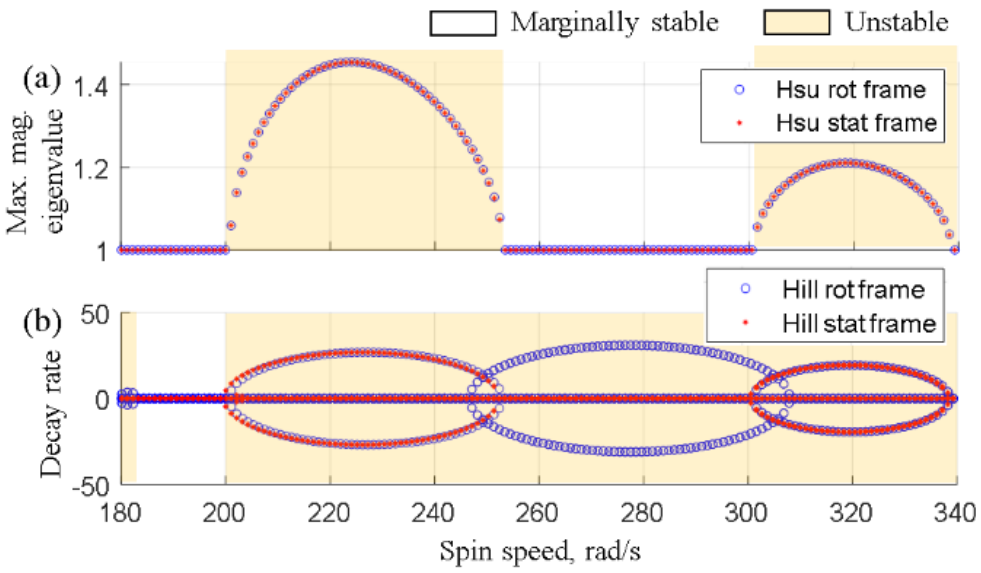

Figure 2.14 Stability predictions of the Jeffcott rotor-bearing model by (a) Hsu's method, (b) Hill's method (jmax=2)

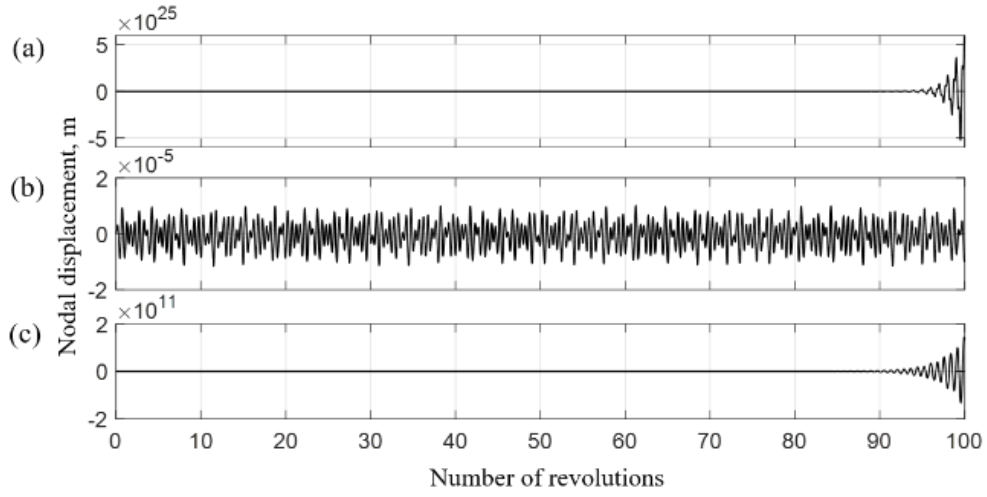

Figure 2.15 y axis displacement of the Jeffcott rotor at rotor spin speed: (a) Ω = 220 rad/s, (b) Ω = 280 rad/s, (c) Ω = 320 rad/s

Hill's method is also tested with the 3D solid rotor bearing system in Figure 2.5 (q_r=0.1). Figure 2.16 compares the two methods for both the isotropic bearings (q_b=0.0) and asymmetric bearings (q_b=0.1) cases. The convergence of Hill's method is achieved by j_{max} = 3. While the instability predictions for both methods agree well in the isotropic bearings, both methods present different stability predictions when it comes to the asymmetric bearing case. As shown in Figure 2.16, Hill's method predicts that the system become unstable at the speed range from Ω = 883 rad/s to Ω = 918 rad/s, whereas Hsu's method gives the opposite prediction on the speed range from Ω = 883 rad/s to Ω = 900 rad/s. As verified by time-transient, numerical integration in Figure 2.10 the system (q_r=0.1, q_b=0.1) is diverging at Ω = 885 rad/s and it implies that Hsu's method predicts the unstable speed ranges accurately for the 3D solid rotor bearing system in the rotor-fixed coordinate system, and Hill's does not. Figure 2.17 illustrates computation

time ratios of Hill's method to Hsu's method vs. the number of dofs in terms of j_{max}. The graphs show that the computational speed becomes slow as j_{max} of Hill's method increases and Hsu's method becomes more advantageous than Hill's method as the number of dofs increases. For example, at 500 dofs, Hsu's method is 63 times, 181 times and 423 times faster than Hill's method for j_{max} = 2, j_{max} = 3 and j_{max} = 4, respectively.

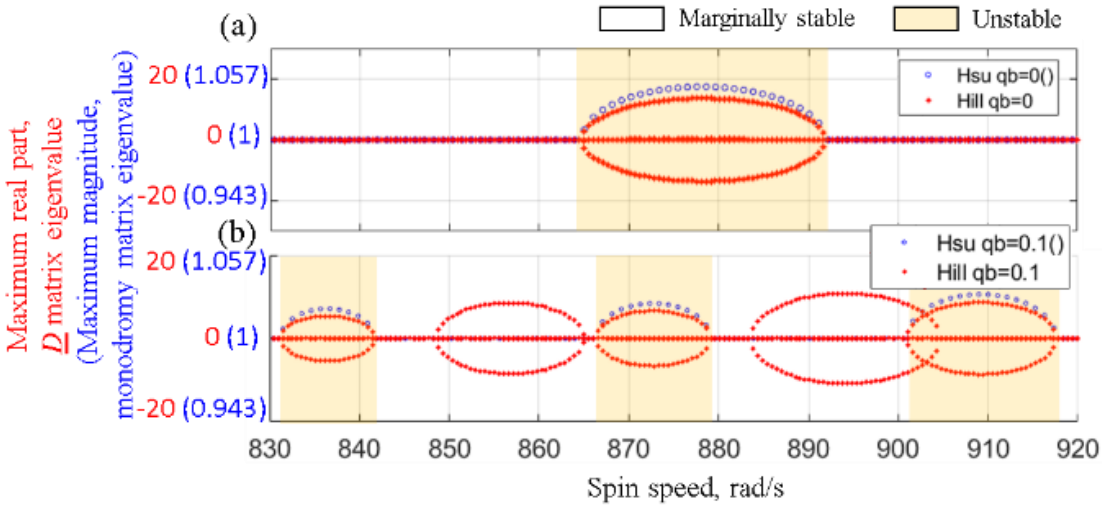

Figure 2.16 Stability predictions by Hsu's method and Hill's method (jmax=3) for (a) q_r = 0.1, q_b = 0.0, (b) q_r = 0.1, q_b = 0.1

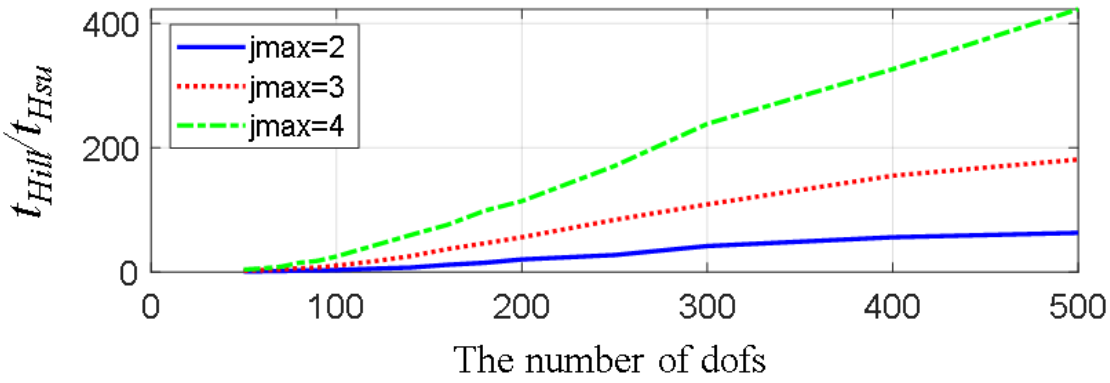

Figure 2.17 Computation time comparison between Hsu's method and Hill's method

2.6. Non-parametric instabilities detection

This section provides examples that verify the proposed method may be used to detect non-parametric instabilities, such as classical oil whirl instability. This is demonstrated using a Timoshenko beam element model of the shaft, and stiffness and damping representations of the fluid film journal bearings. The steel shaft model has a 0.1 m diameter, 2.0 m length and 20 kg disk in the middle. The 2-axial groove fluid film bearings are modeled with 10° X 2 oil groove angles, 0.05 m bearing length, 100 μm assembled bearing clearance, 200 μm machined bearing clearance and 9.37 mPas absolute viscosity of the lubricant [58]. The homogeneous system matrix differential equation can be expressed as

$$\underline{\boldsymbol{M}_T}\ddot{\underline{\boldsymbol{q}}}(t) + \underline{\boldsymbol{C}_T}\dot{\underline{\boldsymbol{q}}}(t) + \underline{\boldsymbol{K}_T}\underline{\boldsymbol{q}}(t) = \underline{\boldsymbol{0}} \tag{2.52}$$

Equation (2.52) can be converted into a first order form as

$$\underline{\dot{\boldsymbol{X}}}(t) = \underline{\boldsymbol{D}}\,\underline{\boldsymbol{X}}(t) \tag{2.53}$$

The coefficient matrix $B(t)$ in Eq. (2.31) becomes the constant matrix $\underline{\boldsymbol{D}}$. Then $\underline{\boldsymbol{H}}_M$ in Eq. (2.37) becomes

$$\underline{\boldsymbol{H}}_{\boldsymbol{M}} = \underline{\boldsymbol{I}}_N exp\left(T_{min}\,\underline{\boldsymbol{D}}\right) \tag{2.54}$$

Let ν be an eigenvector of $\underline{\boldsymbol{D}}$ with corresponding eigenvalue $\lambda = \alpha + \beta i$, then ν is also an eigenvector of $T_{min}\,\underline{\boldsymbol{D}}$ with eigenvalue $\tilde{\lambda} = T_{min}\alpha + T_{min}\beta i$. By reference [59] ν is an eigenvector of the matrix exponential $\underline{\boldsymbol{H}}_{\boldsymbol{M}}$ with corresponding eigenvalue $\hat{\lambda} = e^{\tilde{\lambda}}$, and the magnitude of the eigenvalue is $\left|\hat{\lambda}\right| = \left|e^{T_{min}\alpha + T_{min}\beta i}\right| = e^{T_{min}\alpha}$. Then α and $\left|\hat{\lambda}\right|$ are related by

$$\begin{aligned} &if\ \alpha \le 0, \left|\hat{\lambda}\right| \le 1 \\ &if\ \alpha > 0, \left|\hat{\lambda}\right| > 1, \end{aligned} \tag{2.55}$$

Therefore, the stability of the system is solely determined by the eigenvalues of $\underline{\boldsymbol{D}}$ regardless of the non-zero constant T_{min}, The above shows the equivalence of determining stability either by searching for Monodromy matrix eigenvalues of

magnitude greater than 1, or by searching for real parts of eigenvalues of $\underline{\boldsymbol{D}}$ that are positive, for the non-parametrically excited case. Figure 2.18 shows the stability results for both (a) the Monodromy matrix method and (b) conventional eigenvalue method. It can be concluded that the proposed method can accurately predict instabilities in rotor-bearing systems where both parametric and non-parametric instabilities exist.

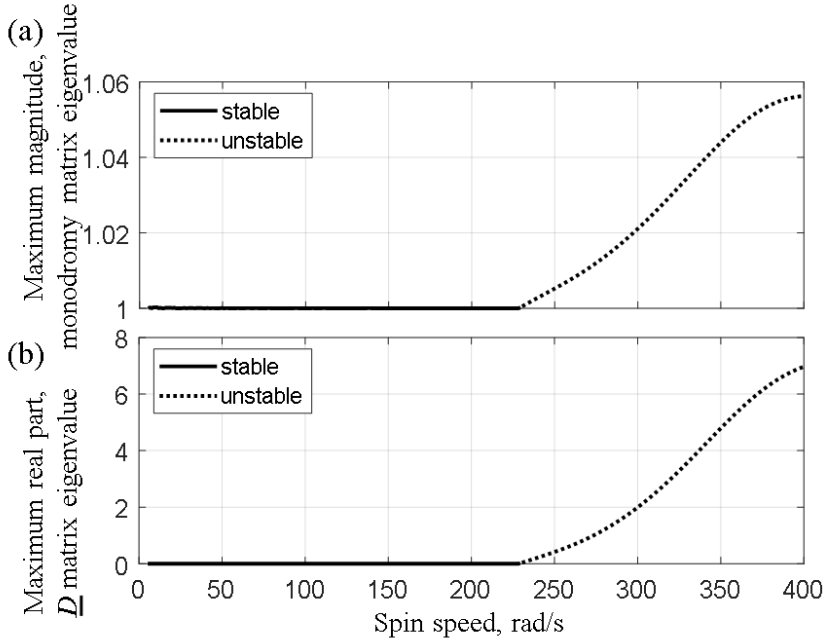

Figure 2.18 Axisymmetric Timoshenko beam rotor on the fluid film journal bearing (a) maximum magnitude, monodromy matrix eigenvalue vs. spin speed, (b) maximum real part, $\underline{\boldsymbol{D}}$ matrix eigenvalue vs. spin speed

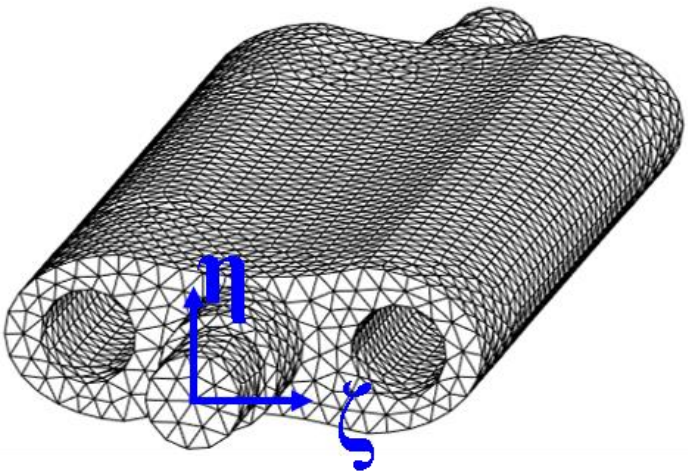

Figure 2.19 Mesh of the Root impeller

2.7. Root Impeller Case Study

Bishop and Parkinson examined a second order forced vibration on 2-pole turbogenerators [60] due to the 2 planes of unequal rotor stiffness interacting with gravity loading. Similarly, other turbo machines that have multiple poles have non-axisymmetric rotors, such as Root type impellers. Figure 2.19 shows a Root impeller that are non-axisymmetric, having shaft stiffness in the two principal axes that are not identical. In this section, the stability of the Root impeller is analyzed with respect to an influence of bearing stiffness asymmetry and bearing damping. The properties of steel are used in the FE model. Table 2.2 lists the bearing coefficients with respect to q_b. Figure 2.20 shows the maximum magnitude, monodromy matrix eigenvalue vs. spin

speed ratio vs. bearing damping ratio for the Root impeller. The unstable range spans from 325 rad/s to 333 rad/s with the damping ratio ζ = 0%. The magnitude and width of the unstable range gradually decrease as ζ increases, and the unstable range vanishes for ζ = 1.0%.

Table 2.2 Bearing stiffness coefficients for the Root impeller

Bearing stiffness coefficients	q_b	0.00	0.02	0.05	0.10	0.20
	k_{b_xx} (N/m)	$1.5e^7$	$1.47e^7$	$1.43e^7$	$1.35e^7$	$1.2e^7$
	k_{b_yy} (N/m)	$1.5e^7$	$1.53e^7$	$1.58e^7$	$1.65e^7$	$1.8e^7$

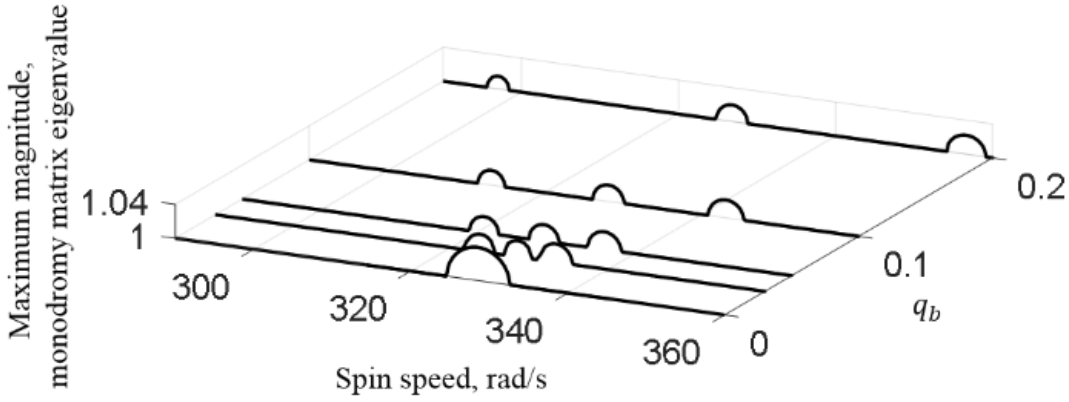

Figure 2.20 Maximum magnitude, monodromy matrix eigenvalue vs. spin speed vs. ζ for the Root impeller with (q_b = 0)

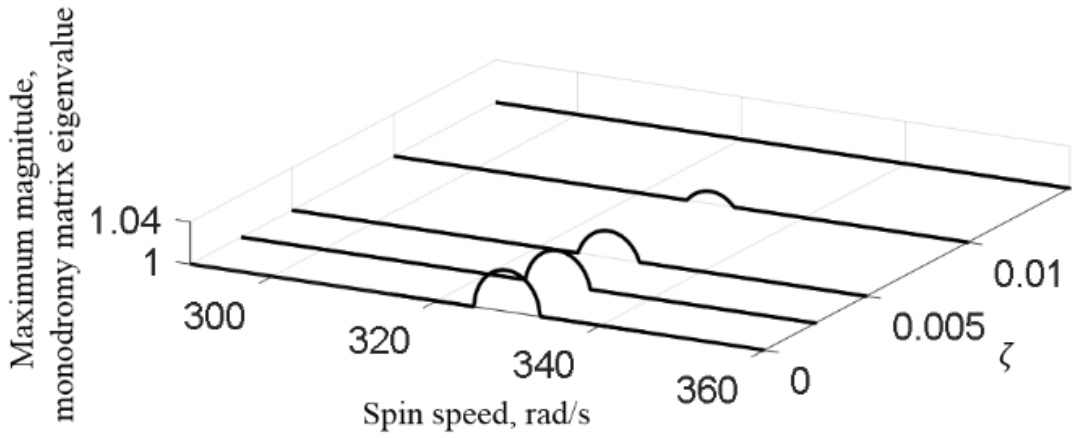

Figure 2.21 Maximum magnitude, monodromy matrix eigenvalue vs. spin speed vs. q_b for the Root impeller

Figure 2.21 illustrates the variation of the unstable range due to change in the bearing asymmetry parameter q_b. The unstable range begins to split into the three separated unstable intervals as q_b increases. The total width of the three unstable ranges after full separation is 54% wider than the width of the unstable range with the isotropic bearings. The first range moves toward the lower speed, and the third range approaches the higher speed, while the second range tends to remain in the vicinity of its original range as the bearing asymmetry increases. The stability evaluation results can be verified by direct time-transient, numerical integration. Figure 2.22 plots the nodal displacements at the bearing nodes in the y-axis versus the number of revolutions for the Root impeller with q_b = 0.00 and ζ = 0%. The rotor-bearing system is marginally stable at 320 rad/s and 340 rad/s, but diverges at 330 rad/s as predicted in Figure 2.20. Figure 2.23 shows the unstable speed ranges when a cross-coupled stiffness of $k_{b\_xy} = -k_{b\_yx} = 7.5\text{e}^5$ N/m is

added to the model at the bearing location. A comparison of Figure 2.21 with Figure 2.23 shows that unstable sub-ranges are combined or merged when cross-coupled stiffness is included. The Root impeller example illustrates how parametrically excited instabilities may occur when the rotor speed is in the vicinity of the two natural frequencies that are the lowest bending modes corresponding to the two-principal rotor stiffnesses being in series with the same (isotropic) bearing stiffness, at zero rpm. The unstable speed range may be split into isolated sub ranges by the presence of bearing asymmetry.

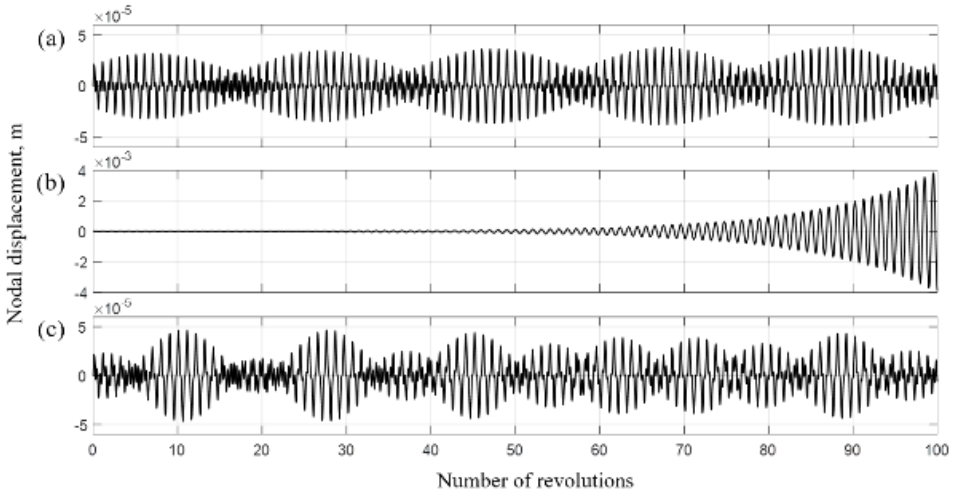

Figure 2.22 Bearing y nodal displacement at the bearing location for the root impeller with (q_b = 0.0, ζ = 0.0) at speeds: (a) **Ω**=320 rad/s, (b) **Ω**=330 rad/s, (c) **Ω**=340 rad/s

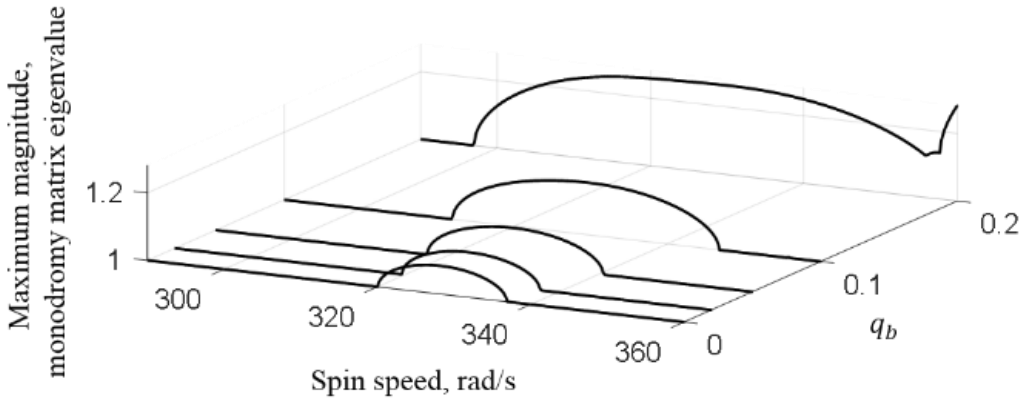

Figure 2.23 Maximum magnitude, monodromy matrix eigenvalue vs. spin speed vs. q_b for the Root impeller with $k_{b\_xy} = -k_{b\_yx} = 7.5e^5$ N/m

2.8. Conclusion

An efficient method was presented for rotordynamic stability simulation of systems with non-axisymmetric rotors and bearings, modeled with 3D solid finite elements. Ten (10) node quadratic tetrahedron elements were developed for modelling the non-axisymmetric rotor. Guyan reduction was utilized to reduce the dimension of the matrix differential equation to efficiently evaluate its monodromy matrices. Parametric instabilities in non-axisymmetric rotor-bearing systems were determined with Floquet theory, exploiting Hsu's method to discretize the Monodromy matrix. Numerical integration and a Routh-Hurwitz test were utilized to validate the approach for a Jeffcott rotor model with rectangular cross section. Use of Hsu's method and parallel computation for evaluation of Monodromy matrices accelerated the computation time by a factor of 400 or more. The approximate Hsu approach was demonstrated to be highly accurate with a large order model example. Parametric studies were conducted to

determine the effect of varying bearing and rotor asymmetry on the intensity of the instability and the speed ranges over which it will occur. The prior method using Hill's infinite determinant was compared with the proposed method using Hsu's method. The presented results imply that applications of Hill's method may be limited to the inertial coordinate system or to small level of bearing asymmetry in the rotor-fixed coordinate system, whereas the proposed method in this paper using Hsu's method accurately predicts the instability of the 3D solid rotor-bearing systems having complex geometries which require a large number of dofs and description in the rotor-fixed coordinate system without limitation of the level of bearing asymmetry. It was also shown that the proposed method becomes more advantageous as the number of dofs increases with respect to computational efficiency. A demonstration model with a Timoshenko beam rotor and fluid film journal bearings was developed to show that the proposed method can detect both parametric and non-parametric instabilities. A Root type impeller example was presented to illustrate the possibility of parametric instability (resonance) for practical, non-axisymmetric rotors. The system exhibited unstable behavior at spin speeds near the first bending modes, undamped natural frequencies. The unstable speed range split into the three parts and its total width increased by 54 % as the asymmetry of the bearings increased. A 1.5% bearing damping ratio was shown to suffice to suppress the parametric instability for the Root impeller model.

3. 3D SOLID FINITE ELEMENT CONTACT MODEL FOR ROTORDYNAMIC ANALYSIS: EXPERIMENT AND SIMULATION*

3.1. Finite Element Formulation

3.1.1. Equations of Motion of Rotor-Bearing System

The focus of the present study is accurate predictions for arbitrary geometry, rotor-bearing systems with internal, preloaded contact interfaces. The geometry is best modeled with 3D solid finite elements. A standard form for the equations of motion of a rotor-bearing system is

$$\underline{\boldsymbol{M}}\ddot{\underline{\boldsymbol{q}}}(t) + \underline{\boldsymbol{C}}(t)\dot{\underline{\boldsymbol{q}}}(t) + \underline{\boldsymbol{K}}(t)\underline{\boldsymbol{q}}(t) = \underline{\boldsymbol{F}}(t) \tag{3.1}$$

where $\underline{\boldsymbol{M}}$, $\underline{\boldsymbol{C}}(t)$, $\underline{\boldsymbol{K}}(t)$, $\boldsymbol{F}(t)$ *and* $\underline{\boldsymbol{q}}(t)$ are the mass matrix, the damping matrix, the stiffness matrix, the external force vector, and the nodal displacement vector, respectively. The methodology of this paper can be applied to three generalized rotor-bearing system types: (1) axisymmetric rotors with orthotropic bearings, (2) non-axisymmetric rotors with isotropic bearings, and (3) non-axisymmetric rotors with orthotropic bearings. For axisymmetric rotors with orthotropic bearings, the rotors are described in the inertial coordinate system, and bearing dynamic coefficients are independent of time. Thus,

---

* Reprinted in part with permission from "3D Solid Finite Element Contact Model for Rotordynamic Analysis: Experiment and Simulation," by Oh, J., Kim, B., and Palazzolo, A., 2020. *ASME J. Vib. Acoust.*,

time-dependent components in $\underline{\boldsymbol{C}}(t)$, $\underline{\boldsymbol{K}}(t)$ are eliminated, and free and forced responses may be easily obtained. Non-axisymmetric rotors with isotropic bearings can be modeled in a rotor-fixed coordinate system, where the coordinate system rotates with the spin speed of the rotor. Both the rotor and the bearing stiffness, mass and damping representations are time-independent in the rotor-fixed coordinate system since the coordinate system is fixed to the rotor, and the bearings are isotropic. Therefore, a standard linear time invariant analysis LTI can be performed for the type 2 systems as well. Closed-form solutions are generally unavailable [1] for type 3 systems, however stability can be evaluated by using Floquet type methods [20]. Type 2 rotor-bearing with contact models are treated in the present paper, while the systems in the other types can be approached in a similar manner.

3.1.2. Finite Element Formulation for Rotor-Bearing Systems

The 3D solid finite element method has the advantage of modeling complex geometrical characteristics of the system without a loss of accuracy from using simplifying assumptions. In Equation (3.1), $\underline{\boldsymbol{K}}$ includes the stress stiffness matrix $\underline{\boldsymbol{K}}_{\sigma}$ which implements the stress-stiffening effect into the finite element model. The stress-stiffening effect is an important consideration in preloaded structural analyses. Similar with a violin string, the resistance to bending deformation increases if a member is under axial tension. In contrast, the bending stiffness decreases if the member has axial compressive stress [11]. The stress-stiffening effect on the response of a stacked rotor

assembly may be significant as the preload increases. The finite element formulation of the stress stiffness matrix is summarized as follows.

The formulation of the stress stiffness matrix is [11, 9]

$$\underline{\boldsymbol{K}}_{\sigma}{}^{e} = \int_{\mathrm{V}_e} \underline{\boldsymbol{G}}^{T} \underline{\boldsymbol{S}}_{\mathbf{0}} \, \underline{\boldsymbol{G}} \, d\mathrm{V}_e \tag{3.2}$$

$$\underline{\boldsymbol{S}}_{\mathbf{0}} = \begin{bmatrix} \underline{\boldsymbol{s}} & \underline{\mathbf{0}} & \underline{\mathbf{0}} \\ \underline{\mathbf{0}} & \underline{\boldsymbol{s}} & \underline{\mathbf{0}} \\ \underline{\mathbf{0}} & \underline{\mathbf{0}} & \underline{\boldsymbol{s}} \end{bmatrix} \tag{3.3}$$

$$\underline{\boldsymbol{s}} = \begin{bmatrix} \sigma_{xx} & \tau_{xy} & \tau_{zx} \\ \tau_{xy} & \sigma_{yy} & \tau_{yz} \\ \tau_{zx} & \tau_{yz} & \sigma_{zz} \end{bmatrix} \tag{3.4}$$

The numerical integration form of the matrix with Gauss quadrature can be represented as

$$\underline{\boldsymbol{K}}_{\sigma}{}^{e} = \sum_{\alpha=1}^{n_G} \sum_{\beta=1}^{n_G} \sum_{\gamma=1}^{n_G} w_{\alpha} w_{\beta} w_{\gamma} \, \underline{\boldsymbol{J}}_{\boldsymbol{G}}{}^{\boldsymbol{e}^{T}} \, \underline{\boldsymbol{G}}^{\boldsymbol{e}^{T}} \underline{\boldsymbol{S}}_{\mathbf{0}}{}^{\boldsymbol{e}} \underline{\boldsymbol{G}}^{\boldsymbol{e}} \underline{\boldsymbol{J}}_{\boldsymbol{G}}{}^{\boldsymbol{e}} \, det\left(\underline{\boldsymbol{J}}^{\boldsymbol{e}}\right) \tag{3.5}$$

$$\underline{\boldsymbol{J}}_{\boldsymbol{G}}{}^{e} = \begin{bmatrix} \underline{\boldsymbol{J}}^{\boldsymbol{e}-\mathbf{1}} & \underline{\mathbf{0}} & \underline{\mathbf{0}} \\ \underline{\mathbf{0}} & \underline{\boldsymbol{J}}^{\boldsymbol{e}-\mathbf{1}} & \underline{\mathbf{0}} \\ \underline{\mathbf{0}} & \underline{\mathbf{0}} & \underline{\boldsymbol{J}}^{\boldsymbol{e}-\mathbf{1}} \end{bmatrix} \tag{3.6}$$

$$\underline{\boldsymbol{J}}^{\boldsymbol{e}} = \begin{bmatrix} \frac{\partial x_1}{\partial \xi_1} & \frac{\partial x_2}{\partial \xi_1} & \frac{\partial x_3}{\partial \xi_1} \\ \frac{\partial x_1}{\partial \xi_2} & \frac{\partial x_2}{\partial \xi_2} & \frac{\partial x_3}{\partial \xi_2} \\ \frac{\partial x_1}{\partial \xi_3} & \frac{\partial x_2}{\partial \xi_3} & \frac{\partial x_3}{\partial \xi_3} \end{bmatrix} \tag{3.7}$$

$$\underline{\boldsymbol{G}}^{\boldsymbol{e}} = \begin{bmatrix} \frac{\partial N_1}{\partial \xi_1} & 0 & 0 & & \frac{\partial N_n}{\partial \xi_1} & 0 & 0 \\ 0 & \frac{\partial N_1}{\partial \xi_1} & 0 & & 0 & \frac{\partial N_n}{\partial \xi_1} & 0 \\ 0 & 0 & \frac{\partial N_1}{\partial \xi_1} & & 0 & 0 & \frac{\partial N_n}{\partial \xi_1} \\ \frac{\partial N_1}{\partial \xi_2} & 0 & 0 & & \frac{\partial N_n}{\partial \xi_2} & 0 & 0 \\ 0 & \frac{\partial N_1}{\partial \xi_2} & 0 & \dots & 0 & \frac{\partial N_n}{\partial \xi_2} & 0 \\ 0 & 0 & \frac{\partial N_1}{\partial \xi_2} & & 0 & 0 & \frac{\partial N_n}{\partial \xi_2} \\ \frac{\partial N_1}{\partial \xi_3} & 0 & 0 & & \frac{\partial N_n}{\partial \xi_3} & 0 & 0 \\ 0 & \frac{\partial N_1}{\partial \xi_3} & 0 & & 0 & \frac{\partial N_n}{\partial \xi_3} & 0 \\ 0 & 0 & \frac{\partial N_1}{\partial \xi_3} & & 0 & 0 & \frac{\partial N_n}{\partial \xi_3} \end{bmatrix} \tag{3.8}$$

where x_1, x_2 and x_3 are element geometry coordinates, and ξ_1, ξ_2 and ξ_3 are natural coordinates, N_1 and N_n are the 1st and nth shape functions, respectively.

3.1.3. Finite Element Formulation of Contact Element

A contact element is used to model the contact stiffness between two different domains that share a preloaded interface. In rotor-bearing systems, a rotor may have multiple contact interfaces via coupling joints, such as Butt, Hirth, or Curvic joints. The contact element is a zero-thickness surface element [11] which defines contact stiffness between two contacting faces. Figure 3.1 illustrates the contact element between two domains. The shaded faces in the middle of the two layers of the hexahedron elements represent the contact elements, and one of the elements is highlighted to visualize unit vectors at the contact face. The unit vector $\underline{\boldsymbol{e}}_n^e$ is normal to the contact plane, and $\underline{\boldsymbol{e}}_{t1}^e$ and $\underline{\boldsymbol{e}}_{t2}^e$ are orthogonal unit vectors tangent to the contact plane. Contact nodes $\underline{\boldsymbol{x}}_1 \sim \underline{\boldsymbol{x}}_4$ belong to the upper domain, whereas $\underline{\boldsymbol{x}}_5 \sim \underline{\boldsymbol{x}}_8$ belong to the counter domain, and they are paired as shown in Figure 3.1 which indicates that the contact nodes are coincident due to the conformality of the mesh at the interface. Conformality of interface meshes is a basic assumption of the present study, while non-conformal meshes may be dealt with using interpolation methods.

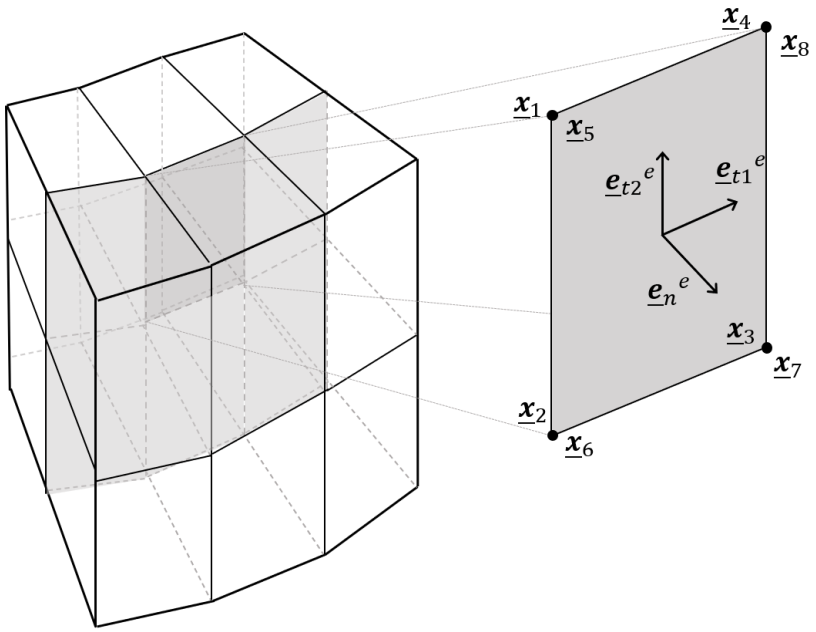

Figure 3.1 Contact elements (coupled with hexahedron elements)

The finite element formulation for the contact stiffness matrix of the contact element can be derived from the potential energy of contact interfaces [11]

$$\begin{aligned} \Pi_c^e &= \frac{1}{2}\int_{S_e} \left(\underline{\boldsymbol{u}}^{\boldsymbol{e}}\right)^T \underline{\boldsymbol{k}}_{\boldsymbol{c}}{}^e \, \underline{\boldsymbol{u}}^e \, dS_e = \frac{1}{2}\int_{S_e} \left(\underline{\boldsymbol{d}}^{\boldsymbol{e}}\right)^T \left(\underline{\boldsymbol{N}}_{\boldsymbol{i}}{}^{\boldsymbol{e}}\right)^T \underline{\boldsymbol{k}}_{\boldsymbol{c}}{}^e \underline{\boldsymbol{N}}_{\boldsymbol{i}}{}^{\boldsymbol{e}} \, \underline{\boldsymbol{d}}^e \, dS_e \\ &= \frac{1}{2}\left(\underline{\boldsymbol{d}}^{\boldsymbol{e}}\right)^T \int_{S_e} \left(\underline{\boldsymbol{N}}_{\boldsymbol{i}}{}^{\boldsymbol{e}}\right)^T \underline{\boldsymbol{k}}_{\boldsymbol{c}}{}^e \underline{\boldsymbol{N}}_{\boldsymbol{i}}{}^{\boldsymbol{e}} dS_e \; \underline{\boldsymbol{d}}^e \end{aligned} \tag{3.9}$$

where $\Pi_c{}^e$, $\underline{\boldsymbol{u}}_e$, $\underline{\boldsymbol{k}}_c{}^e$, $\underline{\boldsymbol{d}}^e$, and $\underline{\boldsymbol{N}}_i{}^e$ are the potential energy of the contact element, the element displacement vector, the element contact stiffness coefficient matrix for a unit area, the element nodal dof vector, and the element inter-domain shape function matrix, respectively.

$$\underline{\boldsymbol{h}}^{\boldsymbol{e}} = \int_{S_e} \left(\underline{\boldsymbol{N}}_{\boldsymbol{i}}^{\boldsymbol{e}}\right)^T \underline{\boldsymbol{k}}_{\boldsymbol{c}}{}^{e} \underline{\boldsymbol{N}}_{\boldsymbol{i}}^{\boldsymbol{e}} \; dS_e \tag{3.10}$$

$$\underline{\boldsymbol{k}}_{\boldsymbol{c}}{}^{e} = \left(\underline{\boldsymbol{e}}_n{}^{e}\right)^T k_{cn}{}^{e} \, \underline{\boldsymbol{e}}_n{}^{e} + \left(\underline{\boldsymbol{e}}_{t1}{}^{e}\right)^T k_{ct1}{}^{e} \, \underline{\boldsymbol{e}}_{t1}{}^{e} + \left(\underline{\boldsymbol{e}}_{t2}{}^{e}\right)^T k_{ct2}{}^{e} \, \underline{\boldsymbol{e}}_{t2}{}^{e} \tag{3.11}$$

where $\underline{\boldsymbol{h}}^{e}$ is the element contact stiffness matrix. The element normal contact stiffness corresponding to $\underline{\boldsymbol{e}}_n{}^{e}$ is $k_{cn}{}^{e}$. The tangential stiffnesses corresponding to $\underline{\boldsymbol{e}}_{t1}{}^{e}$ and $\underline{\boldsymbol{e}}_{t2}{}^{e}$, are $k_{ct1}{}^{e}$ and $k_{ct2}{}^{e}$, respectively. The inter-domain shape function matrix defines the displacement field across the contact plane between two elements in contact. For the case of a conformal mesh on the contact plane, $\underline{\boldsymbol{N}}_i{}^{e}$ can be represented as

$$\underline{\boldsymbol{N}}_i{}^{e} = \left[\begin{array}{cccccc|cccccc} -N_1 & 0 & 0 & -N_{ns} & 0 & 0 & N_1 & 0 & 0 & N_{ns} & 0 & 0 \\ 0 & -N_1 & 0 & 0 & -N_{ns} & 0 & 0 & N_1 & 0 & 0 & N_{ns} & 0 \\ 0 & 0 & -N_1 & 0 & 0 & -N_{ns} & 0 & 0 & N_1 & 0 & 0 & N_{ns} \end{array}\right] \tag{3.12}$$

where *ns* is the number of face nodes, which is 4 for a hexahedron face in this paper, and N_1 and N_{ns} are the shape functions of the first node and ns^{th} node of the element, respectively. The element contact stiffness matrix is evaluated with the following Gauss quadrature formula [9]

$$\underline{\boldsymbol{h}}^{e} = \sum_{\alpha=1}^{n_G} \sum_{\beta=1}^{n_G} w_\alpha w_\beta \underline{\boldsymbol{N}}^{\boldsymbol{e}}\left(\xi_{1\alpha}, \xi_{2\beta}\right)^T \underline{\boldsymbol{k}}_{\boldsymbol{c}}{}^{e} \underline{\boldsymbol{N}}^{\boldsymbol{e}}\left(\xi_{1\alpha}, \xi_{2\beta}\right) det\left(\underline{\boldsymbol{J}}\left(\xi_{1\alpha}, \xi_{2\beta}\right)\right) \tag{3.13}$$

where n_G is the number of Gauss quadrature integration points, $det(\underline{\boldsymbol{J}})$ is the determinant of the Jacobian matrix, $\xi_{1\alpha}$, $\xi_{2\beta}$ are Gauss quadrature integration points in the natural coordinate system and w_α, w_β are the corresponding weight factors.

The size of $\underline{\boldsymbol{h}}^e$ is *6*ns* by *6*ns*. For example, the size of $\underline{\boldsymbol{h}}^e$ for the linear hexahedron element is 24 by 24. The matrix $\underline{\boldsymbol{h}}^e$ of each element is assembled into the global stiffness matrix in Equation (3.1), according to the node connectivity of the system, as

$$\underline{\boldsymbol{M}}\underline{\ddot{\boldsymbol{q}}}(t) + \underline{\boldsymbol{C}}\underline{\dot{\boldsymbol{q}}}(t) + \left\{\underline{\boldsymbol{K}} + \underline{\boldsymbol{K}}_C\right\}\underline{\boldsymbol{q}}(t) = \underline{\boldsymbol{F}}(t) \tag{3.14}$$

where $\underline{\boldsymbol{K}}_c$ is the assembled contact stiffness matrix. Equation (3.14). with external force terms removed, is written in first order (state-space) form as

$$\begin{gathered}\underline{\dot{\boldsymbol{X}}} = \underline{\boldsymbol{A}}\,\underline{\boldsymbol{X}} \\ \underline{\boldsymbol{A}} = \begin{bmatrix} -\underline{\boldsymbol{M}}^{-1}\underline{\boldsymbol{C}} & -\underline{\boldsymbol{M}}^{-1}\left(\underline{\boldsymbol{K}} + \underline{\boldsymbol{K}}_C\right) \\ \underline{\boldsymbol{I}} & \underline{\boldsymbol{0}} \end{bmatrix}\end{gathered} \tag{3.15}$$

where $\underline{\boldsymbol{I}}$ and $\underline{\boldsymbol{0}}$ are the identity matrix and the null matrix. Damped natural frequencies can be obtained from the imaginary parts of the eigenvalues of $\underline{\boldsymbol{A}}$, and stability can be evaluated from the real parts of the eigenvalues of A.

3.1.4. Statistical Model of Contact Stiffness at Contact interfaces

Peak height distributions of engineering surfaces may be considered as having Gaussian distributions [33]. For homogeneous, random isotropic Gaussian surfaces, a statistical contact model that is referred to as the GW contact model was developed by Greenwood and Williamson. The GW contact model mainly requires a surface profile and plane-stress modulus *E'* which can be calculated by

$$\frac{1}{E'} = \frac{1-{\gamma_1}^2}{E_1} + \frac{1-{\gamma_2}^2}{E_2} \tag{3.16}$$

where E and γ are elastic modulus and Poisson's ratio, respectively, while subscripts 1 and 2 refer to the two bodies in contact at the interface. A surface profile *z(x)* may be obtained using a surface roughness measurement device. The three main surface roughness parameters for the relation between contact pressure and contact stiffness can then be evaluated from the measured surface profile *z(x)*. These parameters are η_s indicating the area density, R_s the average radius of the asperity, and σ_s the standard deviation of asperity height. The equations for calculating each parameter are given as follows [61]

$$\eta_s = \frac{m_4/m_2}{6\pi\sqrt{3}} \tag{3.17}$$

$$R_s = \frac{3}{8}\sqrt{\frac{\pi}{m_4}} \tag{3.18}$$

$$\sigma_s{}^2 = \left(1 - \frac{0.8968}{\alpha}\right) m_0 \tag{3.19}$$

$$m_0 = mean(z(x)^2) \tag{3.20}$$

$$m_2 = mean\left(\left(\frac{dz(x)}{dx}\right)^2\right) \tag{3.21}$$

$$m_4 = mean\left(\left(\frac{d^2z(x)}{dx^2}\right)^2\right) \tag{3.22}$$

$$\alpha = \frac{m_0 m_4}{m_2{}^2} \tag{3.23}$$

where m_0, m_2, and m_4 are the zeroth, second, and fourth spectral moments of the profile, respectively. In order to consider surface roughness parameters for a contact plane between two domains whose surface roughnesses are different from one another, composite surface roughness parameters can be utilized [33, 62]. The composite spectral moments for the composite surface are calculated from the spectral moments of each surface by

$$m_{n,p}{}^2 = m_{n,s1}{}^2 + m_{n,s2}{}^2 \quad (n = 0, 2, 4) \tag{3.24}$$

where subscripts *p*, *s1*, and *s2* indicate composite, surface 1 and surface 2, respectively. Then, the composite rough surface parameters are generated using Equation (3.17) - (3.19) for the composite spectral moments. An explicit relation is then utilized to calculate the contact stiffness from the surface roughness parameters, for a given contact pressure [33]

$$P_c = \frac{4}{3}\eta_s E {R_s}^{0.5} {\sigma_s}^{1.5} F_{1.5}(h) \tag{3.25}$$

$$k_{cn} = 2\eta E {R_s}^{0.5} {\sigma_s}^{0.5} F_{0.5}(h) \tag{3.26}$$

where P_c is the contact pressure, k_{cn} is the normal contact stiffness in a unit area, and h is the standardized separation (defined as d/σ_s, where d is distance between the two reference planes of the two different surfaces). A solution of $F_n(h)$ is defined by the parabolic cylinder function

$$\begin{aligned} F_n(h) = \int_h^\infty (s-h)^n \phi^*(s) = \frac{1}{\sqrt{2\pi}} \int_h^\infty (s-h)^n e^{-\frac{1}{2}s^2} ds = \\ = \frac{n!}{\sqrt{2\pi}} e^{-\frac{1}{2}h^2} U(n+0.5, h) \end{aligned} \tag{3.27}$$

where U is Whittaker function, and $\phi^*(s)$ is the Gaussian distribution function and n equals to 0.5 or 1.5. The terms $F_{0.5}$ and $F_{1.5}$ can be determined using the relations

$$U(1,x) = 2\pi^{-\frac{1}{2}}\left(\frac{1}{2}x\right)^{\frac{3}{2}}\left(-K_{\frac{1}{4}} + K_{\frac{3}{4}}\right)$$
$$U(2,x) = 2\cdot\frac{2}{3}\pi^{-\frac{1}{2}}\left(\frac{1}{2}x\right)^{\frac{5}{2}}\left(2K_{\frac{1}{4}} - 3K_{\frac{3}{4}} + K_{\frac{5}{4}}\right) \quad (3.28)$$

where K is Modified Bessel function [63]. Then k_{ct}^{e} can also be obtained by [64]

$$k_{ct}{}^{e} = \frac{\pi(1-\upsilon)}{2(2-\upsilon)}k_{cn}{}^{e} \quad (3.29)$$

An example sensitivity study is presented to illustrate the dependence of k_{cn}^{e} on the 3 surface roughness parameters (Eqs.(3.17) - (3.19)) η_s, R_s and σ_s. Consider the 9 "sample" surfaces listed in Table 3.1. The material parameters E' and υ are set 210 GPa and 0.3 for both surfaces. It is assumed that both contacting surfaces have the same roughness and spectral moments for calculating the composite spectral moments and GW parameters. Figure 3.2 shows the contact stiffness versus contact pressure for each surface. The R_s values increases 100 times from surface 1 to surface 3 in Figure 3.2 (a). The surface roughness parameters η_s and σ_s are varied in the same manner for cases 4-6 (Figure 3.2 (b)) and 7-9 (Figure 3.2 (c)), respectively. The contact stiffness increases monotonically with increasing R_s or η_s, and decreases monotonically with increasing σ_s. The parameter σ_s has the greatest influence on the contact stiffness.

Table 3.1 Surface roughness parameters for the sensitivity test

	R_s (μm)	η_s ($1/m^2$)	σ_s (μm)
Surface 1	0.1	1.0×10^{10}	1
Surface 2	1	1.0×10^{10}	1
Surface 3	10	1.0×10^{10}	1
Surface 4	1	1.0×10^{9}	1
Surface 5	1	1.0×10^{10}	1
Surface 6	1	1.0×10^{11}	1
Surface 7	1	1.0×10^{10}	0.1
Surface 8	1	1.0×10^{10}	1
Surface 9	1	1.0×10^{10}	10

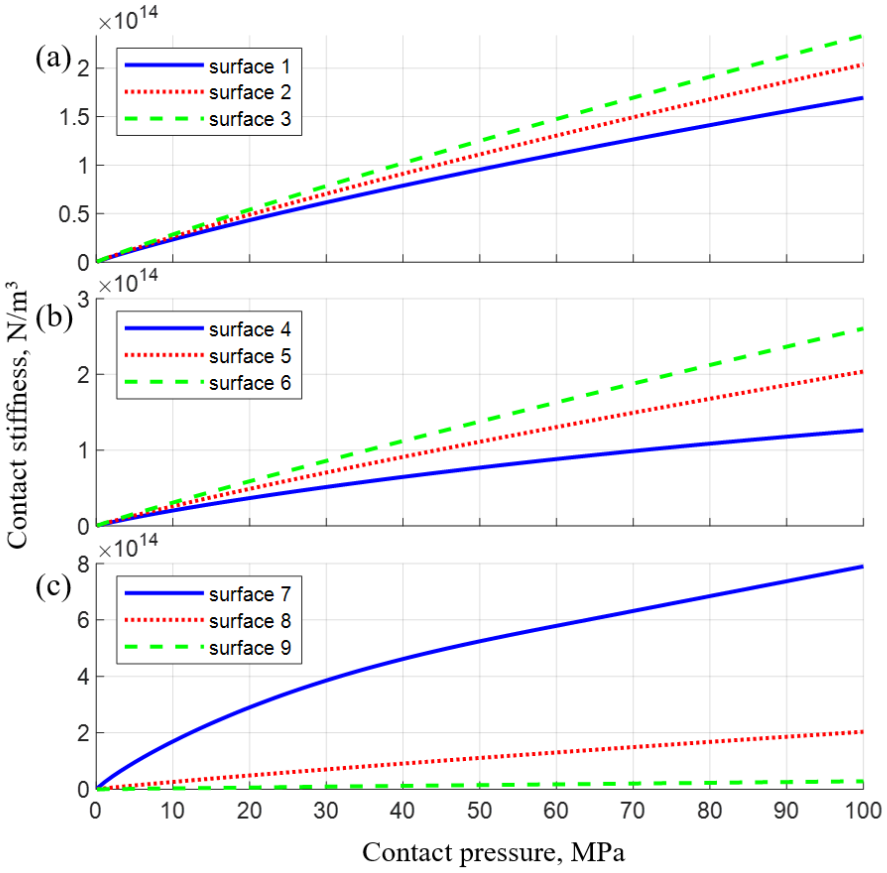

Figure 3.2 Contact stiffness sensitivity analysis vs. the surface roughness parameters

3.2. Experimental Setting

The primary objective of the test apparatus is to investigate the effect of axial preload and surface roughness at the contact joints, on the natural frequencies of a rotor assembly. A test rotor is fastened together with multiple parts, using an axial through-bolt. as shown in Figure 3.3.

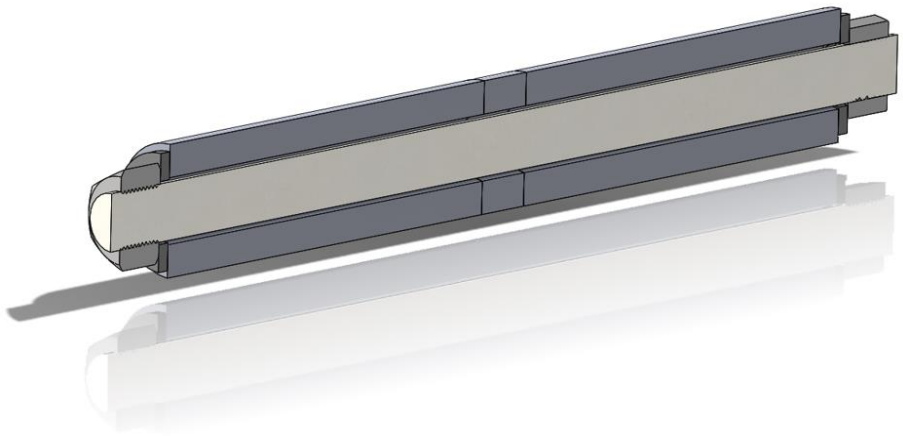

Figure 3.3 Cross sectional view of the test rotor assembly

Table 3.2 lists the properties of each part of the rotor assembly. The diameter values D_{out} of the through bolt, and D_{in} of the nut indicate the major diameters. The through-bolt and nuts are fine thread with 14 threads per 25.4 mm, and the size of pitch is 1.814 mm.

Table 3.2 Properties of the test rotor assembly

	D_{out} (mm)	D_{in} (mm)	L (mm)	E (GPa)	ρ (kg/m^3)	υ
Outer annular shaft	50.8	25.4	152.4	205	8202	0.3
Center joint	50.8	25.4	20.32	205	8202	0.3
Through-bolt	22.23	-	381.00	205	7837	0.3
Nut	33.34	22.23	19.05	205	8202	0.3
Washer	45.21	24.00	4.32	205	7929	0.3

Torque is applied to the through-bolt and the nut, resulting in clamping (preload) forces exerted on the outer annular shafts of the rotor assembly [65]. The force produces tension in the through-bolt and compression in the outer annular shafts. The tensile and compressive forces are considered to be equal, and the compressive force can be measured by a strain gauge system. Figure 3.4 shows the test configuration, and Figure 3.5 shows the strain gage instrumented rotor suspended for free-free modal testing.

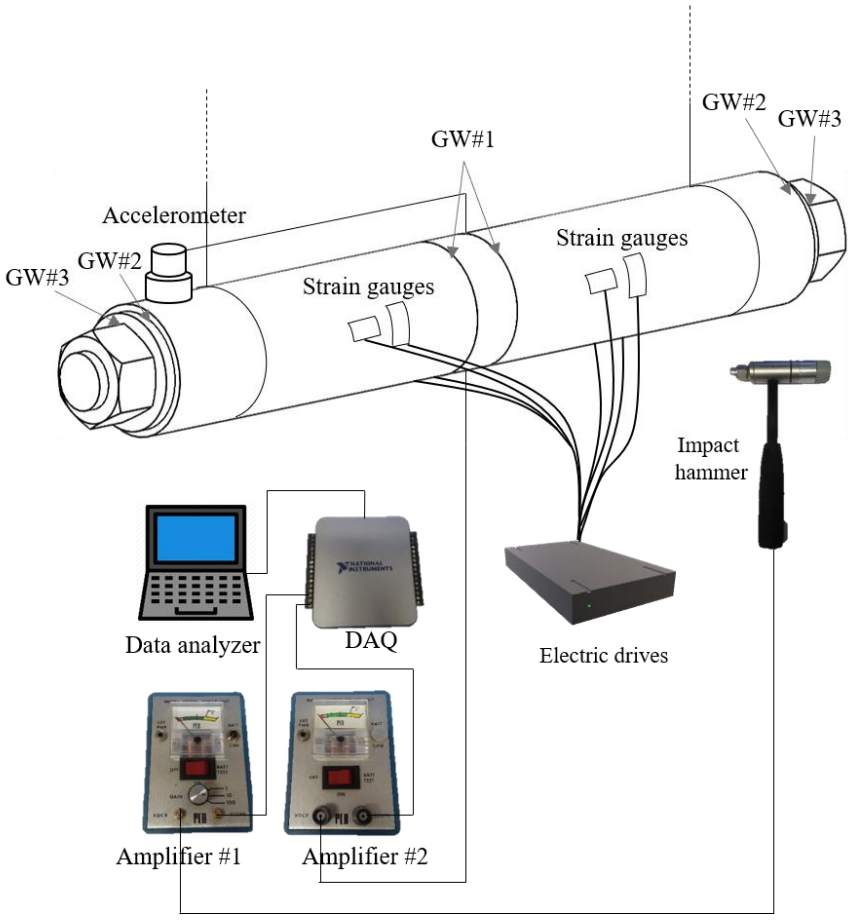

Figure 3.4 The test configuration for measuring preload and flexural natural frequencies

The axial preload force is measured with a 4 - strain gage, full bridge configuration. Two sets of the strain gauge system are installed on each side of the rotor assembly. The second set was added to obtain a second measurement for validation purposes, and both sets always showed very close agreement in axial load prediction. The resolution and the maximum measurable force of the strain gauge system are 0.267 N and 726 kN, respectively. An impact hammer is used to impulse the string supported rotor assembly, in order to measure the free-free natural frequencies. The acceleration of the rotor assembly is measured with a model PCB U353 B33 accelerometer and model PCB 480C02 signal conditioner. The broadband resolution of the accelerometer is 0.005 m/s^2 rms, and the measurement uncertainty of the acceleration amplitude is ± 5 % within the frequency range from 1 to 4000 Hz.

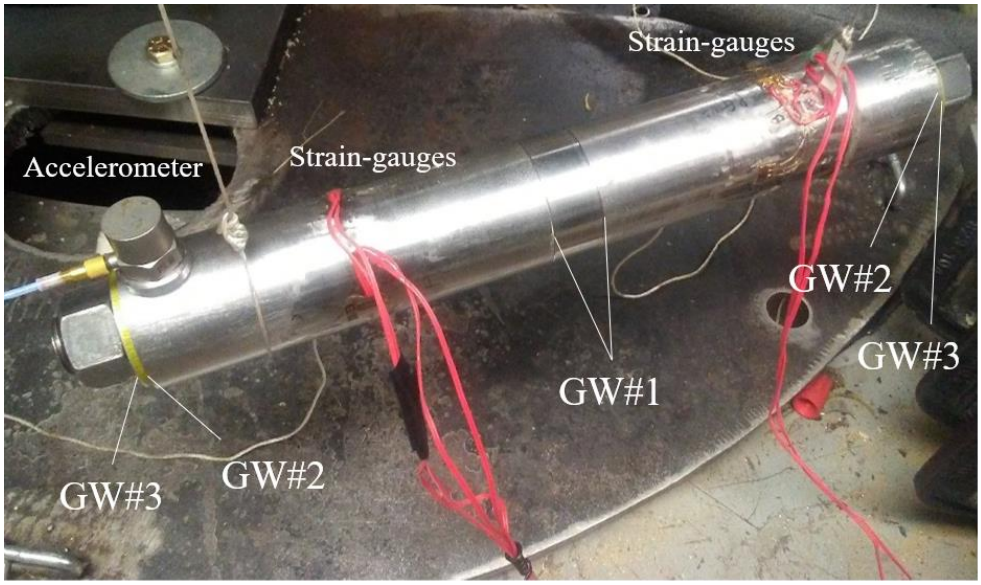

Figure 3.5 Photo of the strain gage instrumented, axially preloaded test shaft

The accelerometer output is recorded with a model NI USB-6002 data acquisition system with a sampling rate of 10,000 samples/sec. The natural frequencies are identified from the accelerometer output and an FFT analyzer, with a frequency resolution of 0.33 Hz. The composite surface roughness at the joints of the rotor assembly is varied by using multiple center joints with various surface roughnesses, while the remaining parts of the rotor assembly are retained. A stylus type surface profiler (Mitutoyo Surftest SJ-210) is used to measure surface roughness with a measurement resolution of 1.6 nm for the height of the surface profile. The probe travels with a linear path, sampling 8,000 points per single measurement. Table 3.3 lists the measured surface roughness parameters for 3 different joints, and for the contact face of the annular shaft. Each surface is measured 10 times in distributed positions, and the averaged values and the relative standard uncertainty (u_{rel}) for the measurement surfaces are listed Table 3.3. The u_{rel} are calculated from [66]

$$u_{rel} = \frac{\sqrt{\sum_i^{n_m}\left(\sigma_{s_i} - \sum_i^{n_m}\sigma_{s_i}/n_m\right)^2/(n_m - 1)}}{\sum_i^{n_m}\sigma_{s_i}/n_m} \tag{3.30}$$

, where n_m is the number of measurements. Composite type surface roughness parameters are calculated via Equations (3.17) - (3.24), for example, the spectral moments m_0, m_2, m_4 of *BJ_Ap* are calculated from the corresponding spectral moments of *BJ_A* and the *Shaft*. For a qualitative comparison, *BJ_A*, *BJ_B*, and *BJ_C* represent smooth, medium, and rough surfaces, respectively. Figure 3.6 compares the probability

distribution functions for the tested rough surfaces *BJ_A*, *BJ_B*, and *BJ_C* and the stand normal distribution. In this figure z* is the centered and scaled height of surface as

$$z^* = \frac{z - \overline{z}}{\sigma_z} \tag{3.31}$$

where $\overline{z}$, σ_z are the mean height and the standard deviation of the height, respectively. One practical method to evaluate Gaussian distribution of the surface is the Kolmogorov-Smirnov test [62], and the test for each surface accepts the null hypothesis at the 5% significance level.

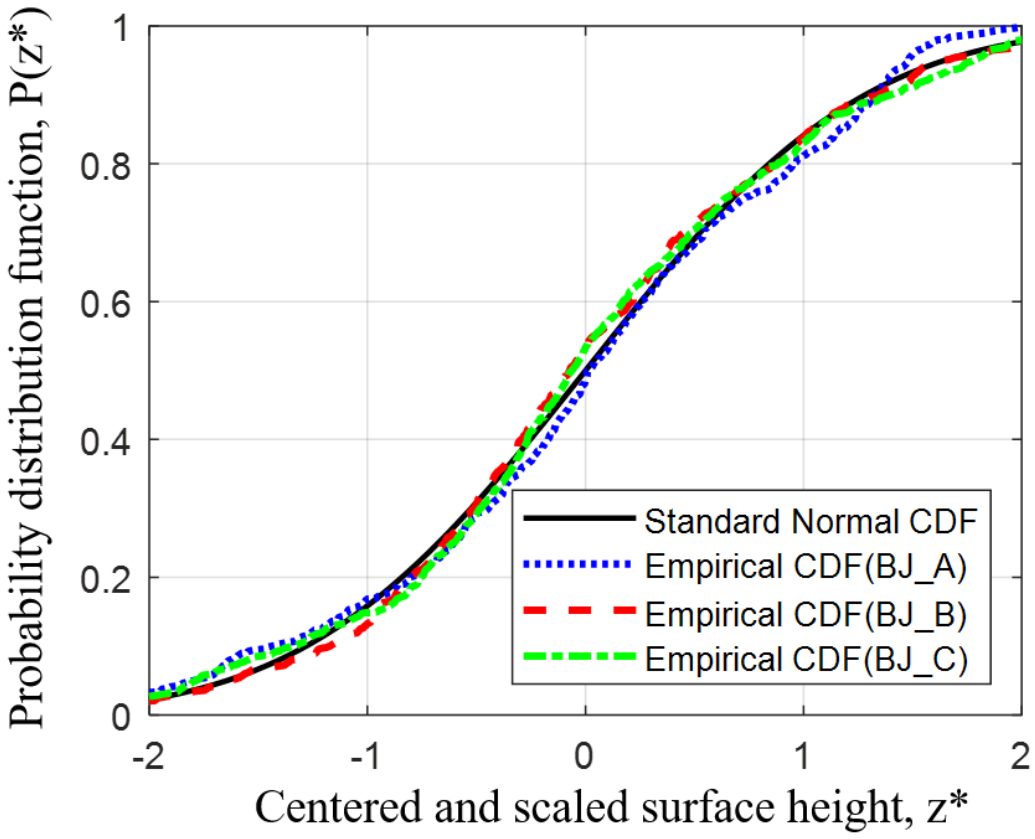

Figure 3.6 Probability distribution functions for the standard normal distribution and test rough surfaces

Table 3.3 Measured surface roughness parameters for the test assembly

Type	Surface		m_0	m_2	m_4	α	R_s (μm)	η_s (10^{-10} $1/m^2$)	σ_s (μm)	u_{rel} (%)
Single	*BJ_A*		0.2690	0.0035	0.0031	66.3267	11.9577	2.7059	0.5151	9.32
	BJ_B		11.1630	0.0815	0.0833	139.9086	2.3032	3.1673	3.3304	8.05
	BJ_C		49.2146	0.1151	0.1873	695.5993	1.5360	5.0436	7.0108	12.30
	Shaft		2.4529	0.0349	0.0562	113.2693	2.8044	4.9931	1.5600	15.13
	Nut		4.6046	0.0607	0.0354	44.3110	3.5323	1.8096	2.1240	10.06
	Washer		6.1802	0.0201	0.0406	621.8337	3.2984	6.2664	2.4842	7.15
Composite	*GW#1*	*BJ_Ap*	2.4676	0.0351	0.0563	112.9570	2.8022	4.9751	1.5646	-
		BJ_Bp	11.4293	0.0887	0.1005	146.0490	2.0971	3.5125	3.3703	-
		BJ_Cp	49.2757	0.1203	0.1955	665.9758	1.5032	5.0394	7.0149	-
	GW#2 (Nut-Shaft)		5.2172	0.0700	0.0664	70.7588	2.5790	2.9424	2.2696	-
	GW#3 (Washer-Nut)		6.6492	0.0403	0.0693	284.3040	2.5243	5.3377	2.5745	-

Natural frequencies are measured with preload increments of approximately 10 kN. The temperature of the rotor assembly was maintained with room temperature in the range 23 ˚C to 24 ˚C during the measurements. The mode utilized for the comparative study is the first bending mode of the outer shaft. Figure 3.7 plots the measured natural frequencies versus preload for *BJ_Ap*. The estimated uncertainties of measurement are ± 0.33 Hz for the natural frequency. The relative uncertainty for the preload is 2.25 %. The legends *Experiment BJ_Ap #1* and *Experiment BJ_Ap #2* represent the first attempt and the second attempt, respectively. *Interpolated BJ_Ap#1* indicates spline interpolation values of *BJ_Ap#1* which is included to quantitively evaluate the repeatability. The average relative difference between *BJ_Ap #1* and *BJ_Ap #2* is within 0.29 %, which infers acceptable repeatability of the test.

As shown in Figure 3.7, the measured natural frequency increases as preload increases until 100 kN preload, and tends to converge. The natural frequency curve in Figure 3.7 may account for a combined result of the asperity effect and the stress-stiffening effect. As contact pressure at the contact surface increases, the contact stiffness increases, resulting in an increase of the natural frequency. On the other hand, the outer shaft of the rotor assembly is under compressive stress due to the preload. Hence, the resistance to bending deformation may be reduced. The contribution of each effect will be evaluated with the simulation model in the following section. Figure 3.8 shows the experimental results for 3 different configurations. The natural frequencies for each case tend to have converged values near a preload of 100 kN, while *BJ_Cp* shows the biggest rate of change followed by *BJ_Bp* and *BJ_Ap*, respectively.

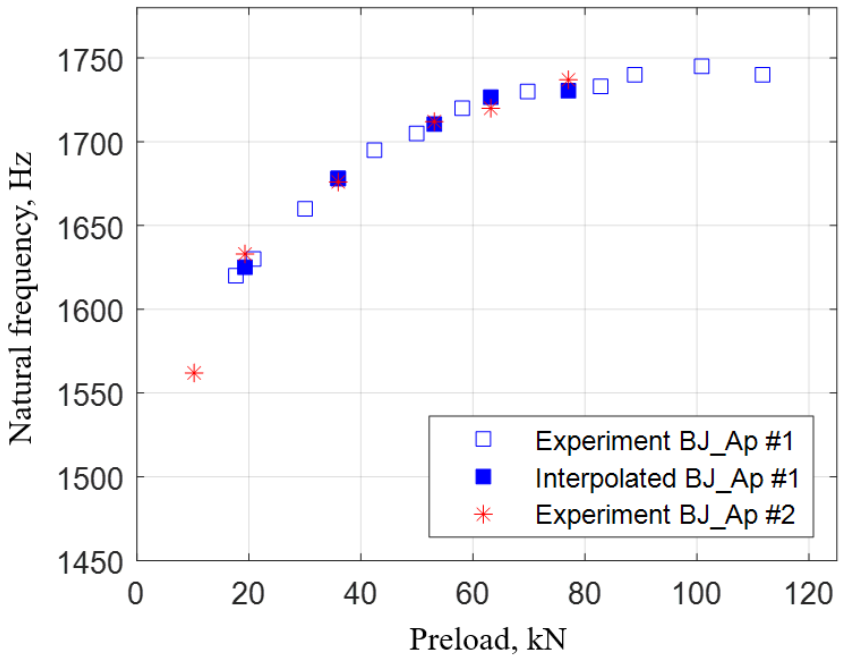

Figure 3.7 Measured natural frequencies vs. preload for BJ_Ap#1 and BJ_Ap#2

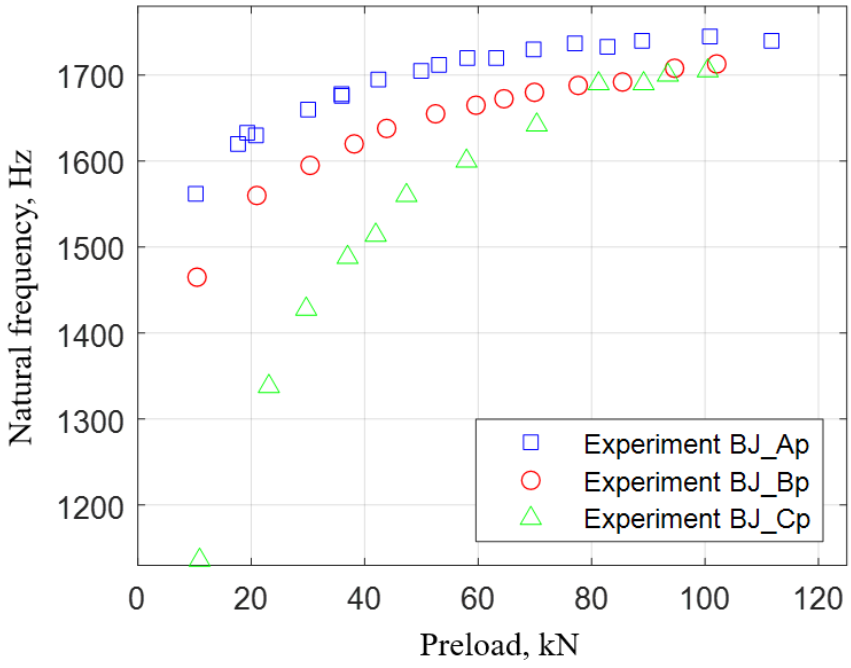

Figure 3.8 Measured natural frequencies vs. preload for BJ_Ap, BJ_Bp, BJ_Cp

3.3. Simulation Model

3.3.1. Finite Element Model

A computer simulation model with 3D solid elements and the contact model outlined above, was developed to compare with the measured results. The geometry of the prediction model is shown in Figure 3.3, and separate meshes are generated for each part of the rotor assembly. The FEM mesh consists entirely of 8-node hexahedron elements, and the meshes of the contacting parts are conformal at shared interfaces (joints). High order tetrahedron elements, such as 10-node quadratic tetrahedron

elements, can also be used for more complex geometries as long as the nodes are coincident at interfaces. A grid test for convergence is shown in Figure 3.9, and a converged mesh is illustrated in Figure 3.10.

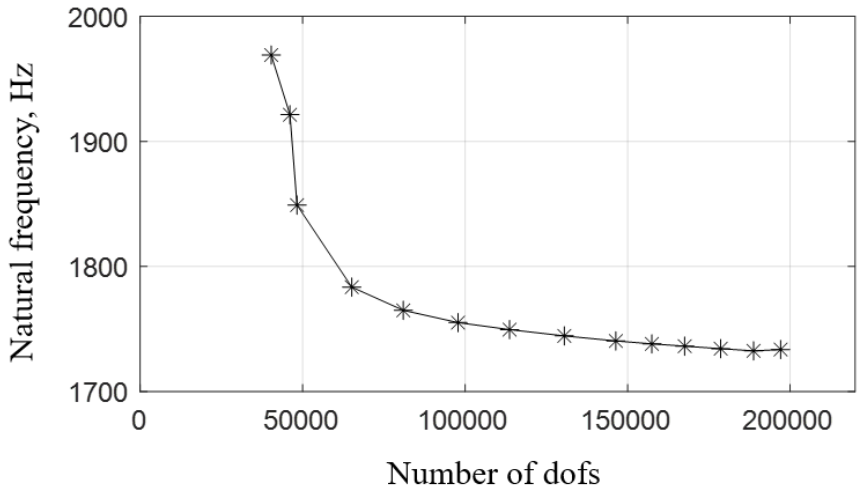

Figure 3.9 Grid test for the test rotor prediction model

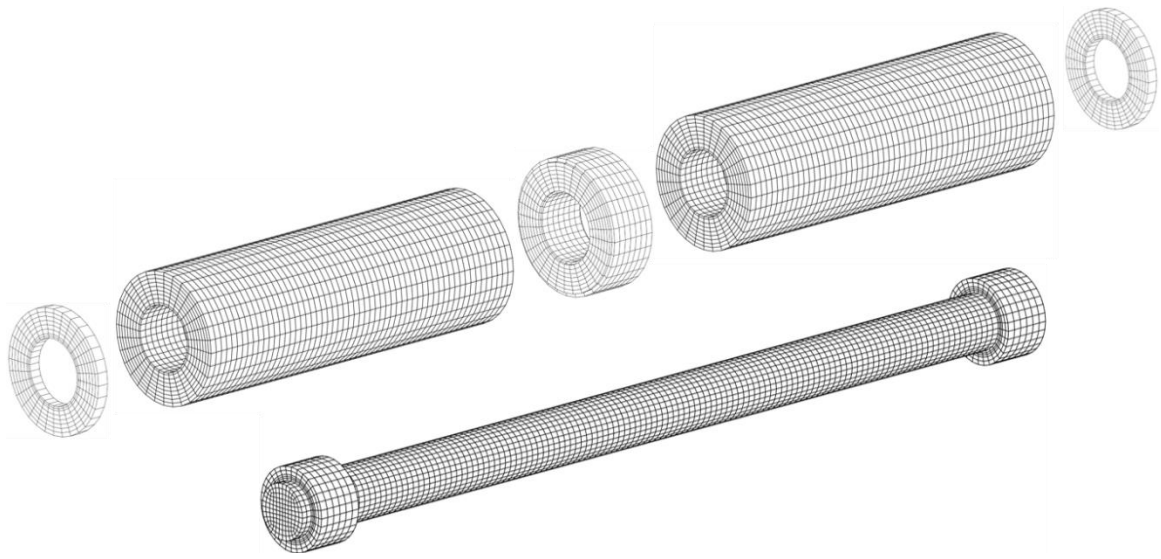

Figure 3.10 Mesh of the test rotor prediction model

The finite element model of the entire rotor assembly is composed of 55,584 linear hexahedron elements, 63,961 nodes, and 191,883 degrees of freedom. In total, 6 contact faces are modeled with the contact stiffness elements developed above. It is assumed that the contact effect between the through-bolt and the nuts is negligible for the mode shape of interest. The contact nodes at the interfaces are highlighted in Figure 3.11, and the contact elements defined in Equation (3.13) are generated at each contact plane. The measured GW parameters are assigned to calculate contact stiffness at each interface.

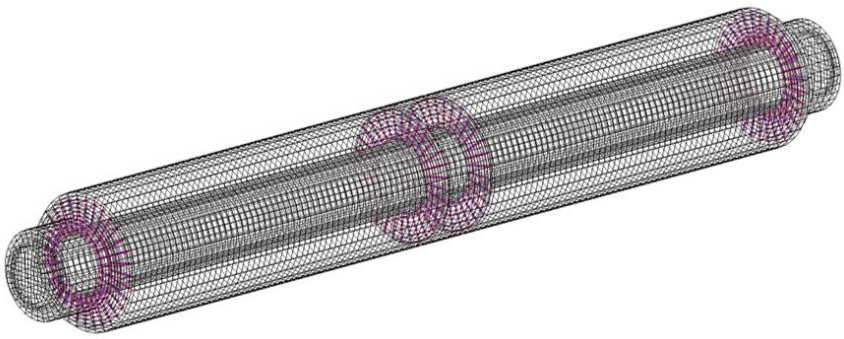

Figure 3.11 Contact nodes of the test rotor model

3.3.2. Contact Modeling Method

The determination of contact stiffnesses is an important step in determining the natural frequencies of the preloaded rotor assembly. Preload is set as an input boundary condition at a joint and the corresponding contact stiffnesses are then calculated. A set of element faces is selected for imposing boundary pressure fields that are obtained from the preload. Figure 3.12 highlights the boundary faces where the nuts and the washers are in contact. Boundary pressure fields are imposed to both faces of two different

domains with the same magnitude and the opposite directions. For *boundary face 1* as noted in Figure 3.12, $-P_{bc}$ and P_{bc} are imposed to the right-hand-side face of the nut and the left-hand-side face of the washer, where P_{bc} is equal to the preload divided by the area. This results in a tensile load applied to the through bolt, and compression load applied to the shaft. Contact pressure fields for all other contact interfaces are determined from the calculated stresses at the interface. The stresses corresponding to contact pressure should be normal to the contact face which can be obtained by the tensor transformation of the nodal stress tensors using the normal vector of the contact face.

Define two separated sub-assemblies as the outer member sub-assembly (OMA) and the inner member sub-assembly (IMA), since stress analyses are carried out separately for the two sub-assemblies. The OMA consists of the washers, the annular shafts, and the center joint, and the IMA is composed of the through-bolt and the nuts. Fictitious soft springs with relatively small stiffnesses (1.0×10^5 N/m) are applied to both the OMA and IMA, in order to remove the singularity in the stiffness matrix associated with rigid body motion. This is a standard practice and varying the soft spring stiffness confirmed that it did not affect the calculated results. The soft springs are included only when stress analysis is performed and otherwise removed. The implicit relation for the system stiffness matrix is summarized as

$$\underline{\boldsymbol{K}} = \underline{\boldsymbol{K}}_{sys} + \underline{\boldsymbol{K}}_{\sigma}\left(\underline{\boldsymbol{\sigma}}\left(\underline{\boldsymbol{K}}\right)\right) + \underline{\boldsymbol{K}}_{c}\left(\underline{\boldsymbol{\sigma}}\left(\underline{\boldsymbol{K}}\right)\right) \tag{3.32}$$

, where $\underline{\boldsymbol{K}}$ is the total stiffness matrix of the OMA and IMA combined, $\underline{\boldsymbol{K}}_{sys}$ is the constant system stiffness matrix without contact stiffness and stress stiffness, $\underline{\boldsymbol{K}}_{\sigma}$ is the

stress stiffness matrix, $\underline{\boldsymbol{K}}_c$ is the contact stiffness matrix and $\underline{\boldsymbol{\sigma}}$ is the stress tensor. An iterative method is applied to solve Equation (3.32). Figure 3.13 explains this iterative procedure with a flowchart.

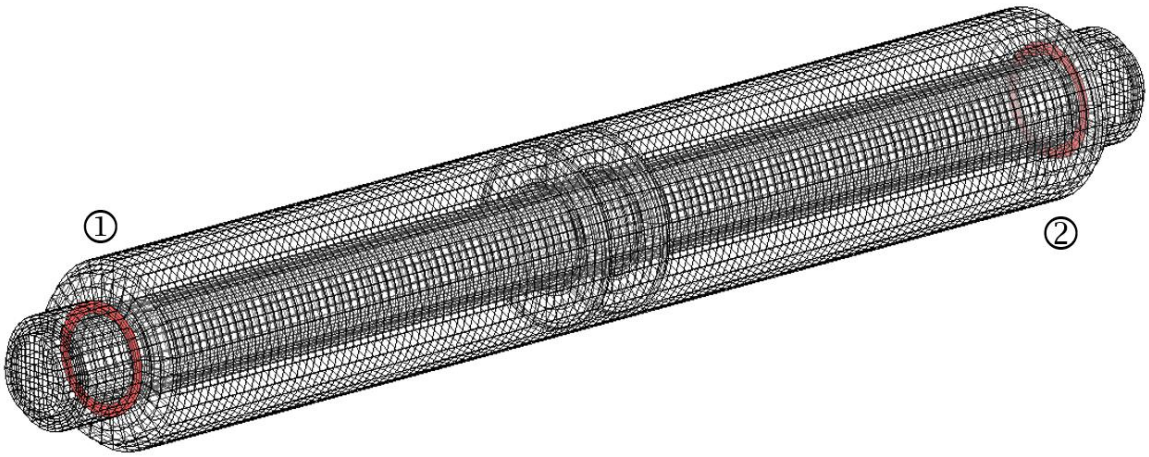

Figure 3.12 Boundary faces for the test rotor model

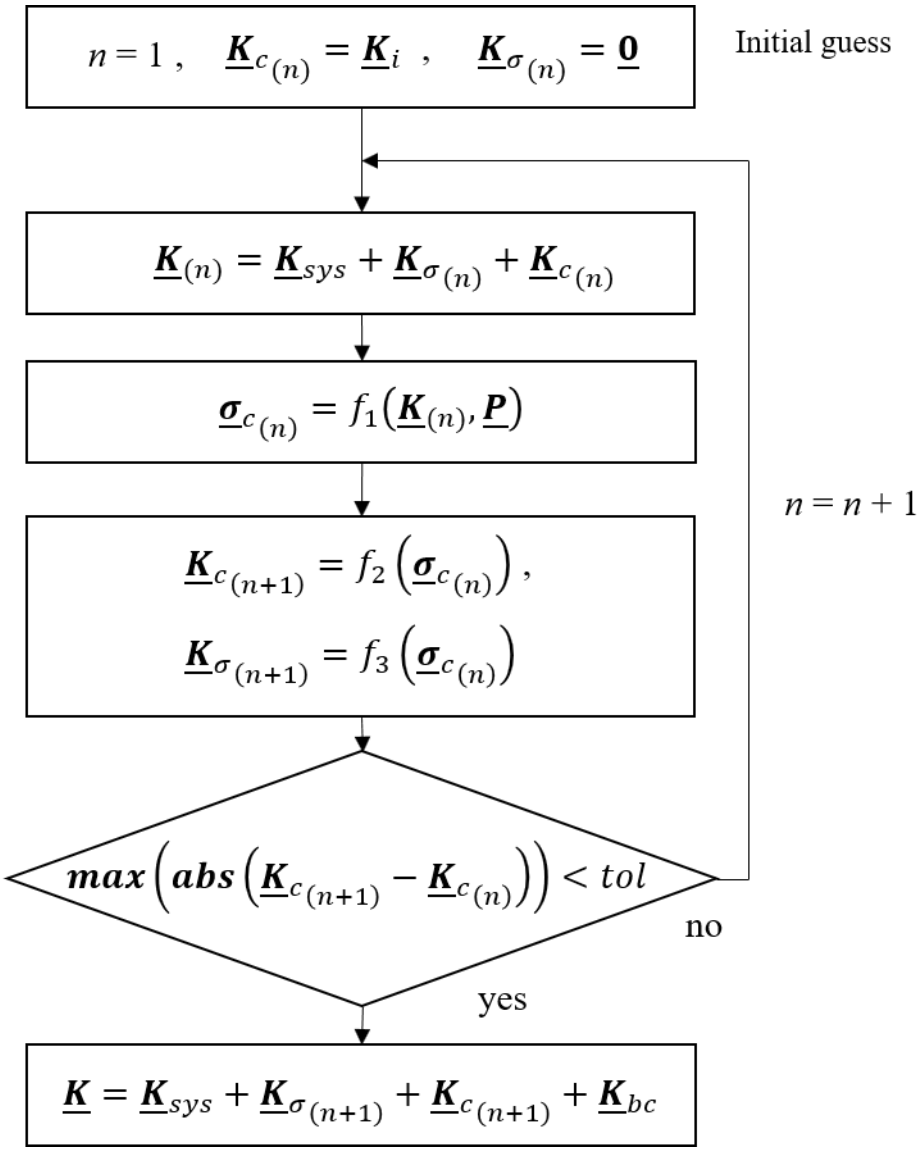

Figure 3.13 Flowchart for $\underline{\mathbf{K}}$ calculation

In this flowchart $\underline{\boldsymbol{K}}_c$ has the initial guess $\underline{\boldsymbol{K}}_i$, and $\underline{\boldsymbol{K}}_\sigma$ is initialized with a null matrix. By following the flowchart, $\underline{\boldsymbol{K}}_{(1)}$ is the sum of $\underline{\boldsymbol{K}}_{sys}$ and $\underline{\boldsymbol{K}}_{c(1)}$, and then $\underline{\boldsymbol{\sigma}}_{c(1)}$ can be calculated with $\underline{\boldsymbol{K}}_{(1)}$ and the pressure boundary conditions $\underline{\boldsymbol{P}}$. The matrices $\underline{\boldsymbol{K}}_{c(2)}$ and $\underline{\boldsymbol{K}}_{\sigma(2)}$ can be obtained by Equation (3.25) - (3.28), after $\underline{\boldsymbol{\sigma}}_{c(1)}$ is determined. Each component of

abs($\underline{\boldsymbol{K}}_{c(2)}$ - $\underline{\boldsymbol{K}}_{c(1)}$) is evaluated and the total stiffness matrix is determined by the matrix sum of all the stiffness matrices in the current iteration, 2 in this instance, if the evaluated value is smaller than *tol* , a tolerance set by the analyst. Otherwise, $\underline{\boldsymbol{K}}_{c(2)}$ and $\underline{\boldsymbol{K}}_{\sigma(2)}$ are set as initial matrices for the next iteration. The loop continues until $\underline{\boldsymbol{K}}_{c}$ shows term wise convergence. The total stiffness matrix is determined by the matrix sum of all the stiffness matrices in the last iteration after convergence is obtained. Note that $\underline{\boldsymbol{K}}_{bc}$ is a contact stiffness matrix for the boundary faces where the boundary pressure fields are imposed. The matrix $\underline{\boldsymbol{K}}_{bc}$ is integrated into the system matrix at the final stage of the procedure, connecting the OMA and IMA. The matrix $\underline{\boldsymbol{K}}_{bc}$ is a constant matrix since the boundary pressure fields determine the contact stiffness of the boundary faces. Figure 3.14 shows the axial(z) direction (σ_{zz}) stress contours over a cross-section, for a converged $\underline{\boldsymbol{K}}$ with a 120 kN preload. Figure 3.15 shows the axial stress contour of the contact center joint for a 120 kN preload, providing the pressure in the radial and the axial direction. The present modeling approach obtains the interface pressures from the σ_{zz}, and in turn determines the contact stiffness from the contact pressure and formulae (3.25) - (3.26).

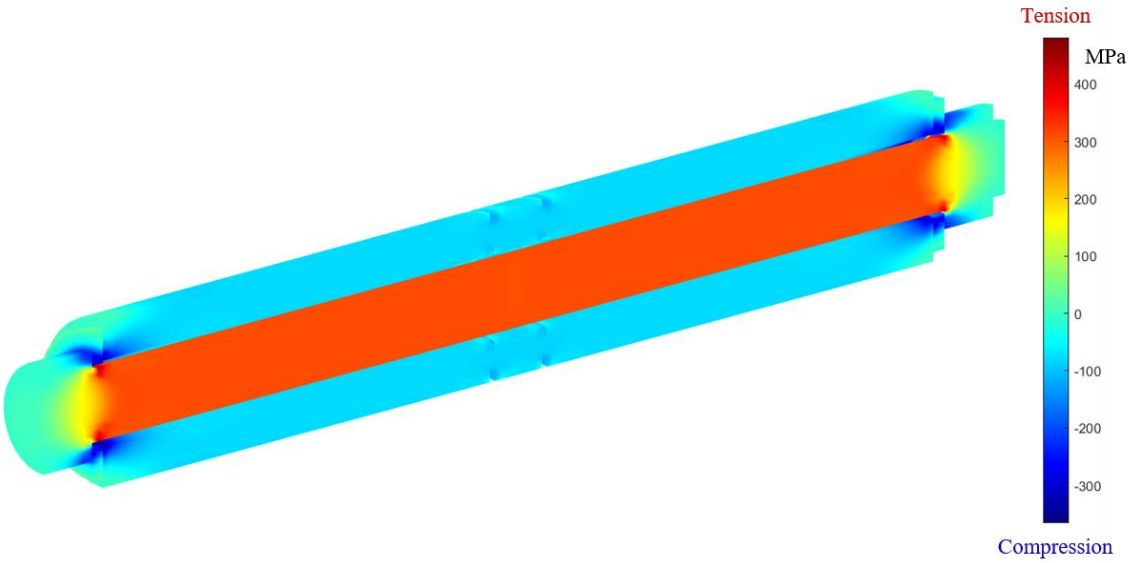

Figure 3.14 Cross-section view of the stress distribution in the axial direction for the test rotor assembly with a 120 kN preload

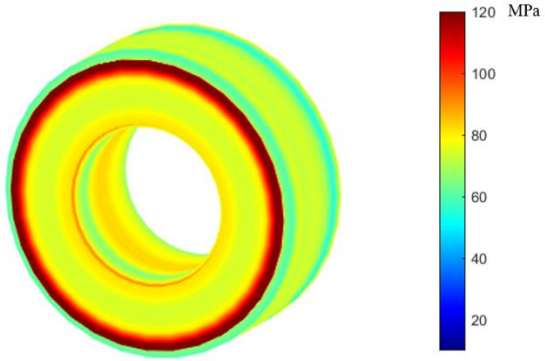

Figure 3.15 Axial stress contour of the contact center joint of the test rotor assembly with a 120 kN preload

Figure 3.16 Free-free 1st bending mode shape of the rotor with BJ_Ap at preload 60 kN

As discussed earlier, OMA and IMA are predicted to be under compression and tension, respectively. Free-free natural frequencies of the preloaded rotor are predicted for the calculated contact stiffness and stress-stiffness. Figure 3.16 illustrates the 1st bending mode shape of the rotor with *BJ_Ap* at preload 60 kN. Predictions and measurements of rotor natural frequencies are made for preloads of 10, 20, 40, 60, 90, and 120 kN. Figure 3.17 compares the measurements and the predictions for the rotor assembly configuration *BJ_Ap*. Stress stiffening is seen to have a softening effect at high preloads.

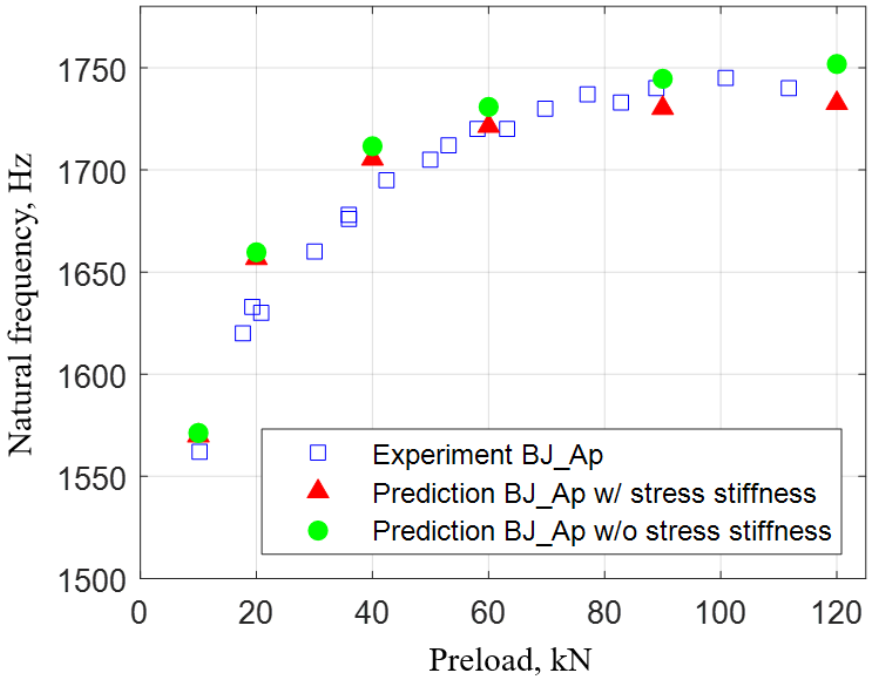

Figure 3.17 Natural frequency vs. preload for the test rotor assembly configuration BJ_Ap

3.3.3. Experimental Validation

Figure 3.18 shows a comparison between the measurements and the predictions with stress stiffening effect for the rotor assembly configurations *BJ_Ap*, *BJ_Bp* and *BJ_Cp*. The average absolute errors of the configurations BJ_Ap, BJ_Bp and BJ_Cp are 30.75 Hz (1.84%), 23.76 Hz (1.48%), and 79.46 Hz (5.6%), respectively. The maximum absolute errors of the configurations BJ_Ap, BJ_Bp and BJ_Cp are 48.47 Hz (2.97%), 36.42 Hz (2.10%), and 116.59 Hz (6.56%), respectively.

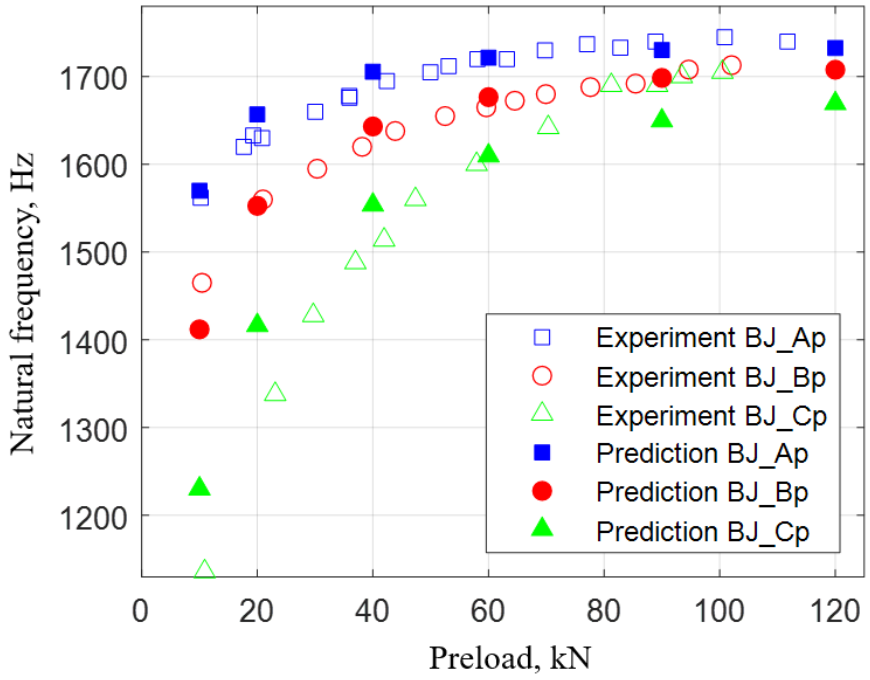

Figure 3.18 Comparison between the experiments and the predictions of the test rotor assembly

3.4. Application: Overhung Rotor-Bearing System

The preceding example clearly reveals the significant effects of joint surface roughness on the lowest bending mode of a short, non-rotating shaft assembly with free-free boundary conditions. In actual machinery, the rotating assemblies are often geometrically complex, rotate at high speeds and are supported by hydrodynamic, hydrostatic, or rolling element bearings. To address this case, the next example considers an industrial class machinery rotor with an overhung impeller [67]. The actual connection of the impeller on the shaft may be different, but it is modelled as an axially

preloaded connection for illustrating the method presented. In that regard, one could view the connection in the model as an impeller with a loose fit with the shaft, being retained with a locknut. The dynamic coefficients of the tilting pad journal bearings are numerically calculated with the given bearing parameters by solving Reynold's equation, or with CFD, as shown in Figure 3.19 [68, 69, 70, 71, 72, 73, 74].

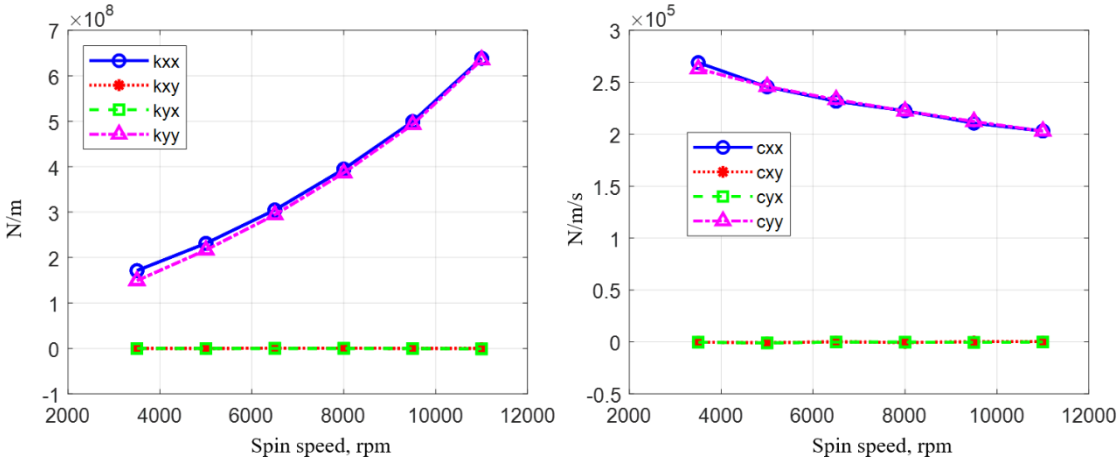

Figure 3.19 Dynamic coefficients of the support bearings

A rotor-fixed coordinate system is selected to describe the rotor-bearing system since the bearings are essentially isotropic, within the operating range as shown in Figure 3.19. The example rotor is axisymmetric so an inertial coordinate system could be used. However, the rotor fixed coordinates are used to present a more general approach that could be used for non-axisymmetric rotors or interfaces, such as a Hirth joint. An equation of motion of a rotor-bearing system in the rotor-fixed coordinate system can be represented as [22]

$$\underline{\boldsymbol{M}}\ddot{\underline{\boldsymbol{q}}}(t) + \left\{2\Omega\underline{\boldsymbol{C}}_{\boldsymbol{R}} + \underline{\boldsymbol{C}}_{\boldsymbol{b,r}}\right\}\dot{\underline{\boldsymbol{q}}}(t) + \left\{\underline{\boldsymbol{K}}_s - \Omega^2\underline{\boldsymbol{K}}_d + \underline{\boldsymbol{K}}_\sigma + \underline{\boldsymbol{K}}_{\boldsymbol{b,r}}\right\}\underline{\boldsymbol{q}}(t) = \Omega^2\underline{\boldsymbol{f}}_c \quad (3.33)$$

where $\underline{\boldsymbol{C}}_R$, $\underline{\boldsymbol{C}}_{b,r}$, $\underline{\boldsymbol{K}}_s$, $\underline{\boldsymbol{K}}_d$, $\underline{\boldsymbol{K}}_\sigma$, $\underline{\boldsymbol{K}}_{b,r}$, and $\underline{\boldsymbol{f}}_c$ are the Coriolis matrix, the bearing damping matrix in the rotor-fixed coordinate system, the structural stiffness matrix, the dynamic stiffness matrix, the stress-stiffness matrix, the bearing stiffness matrix in the rotor-fixed coordinate system, and the centrifugal force vector, and the mass matrix is identical to $\underline{\boldsymbol{M}}$ defined in Equation (3.1). For bearings in the rotor-fixed coordinate system, $\underline{C}_{b,r}$ and $\underline{K}_{b,r}$ are not identical to the bearing coefficient matrices in the inertial coordinate system. The detailed derivation for $\underline{\boldsymbol{C}}_{b,r}$ and $\underline{\boldsymbol{K}}_{b,r}$ is provided by [20]. Figure 3.20 illustrates the rotor-bearing system assembly and the meshes. A grid test was carried out as shown in Figure 3.21.

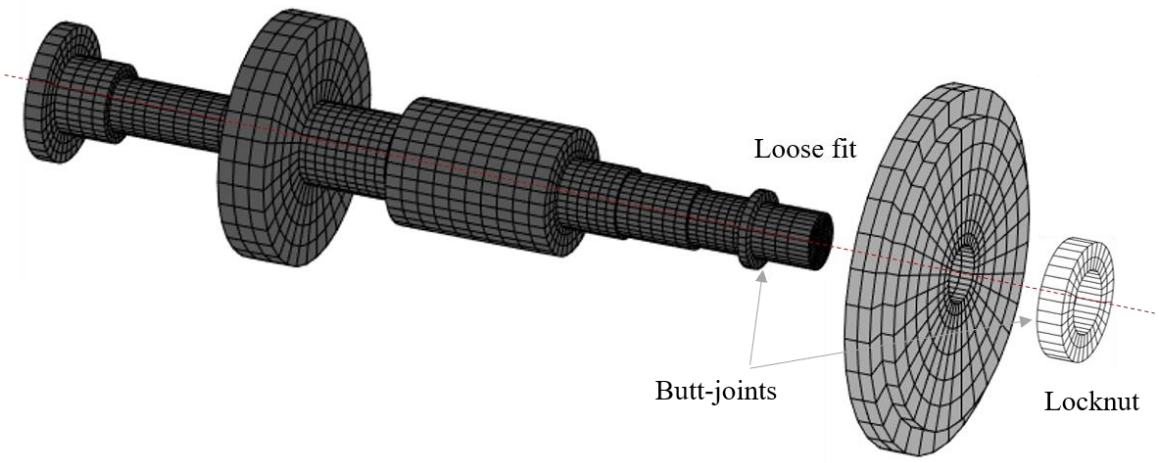

Figure 3.20 Overhung type rotor [67]

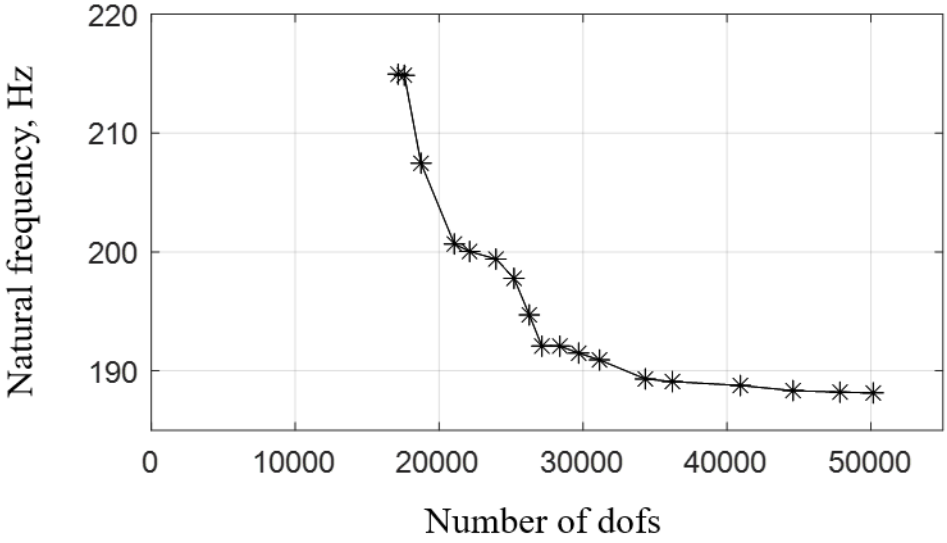

Figure 3.21 Grid test of the overhung rotor-bearing system

Clamping forces are applied to the impeller disk by the locknut. Figure 3.22 shows the contact nodes at the interfaces between the main shaft and the impeller disk.

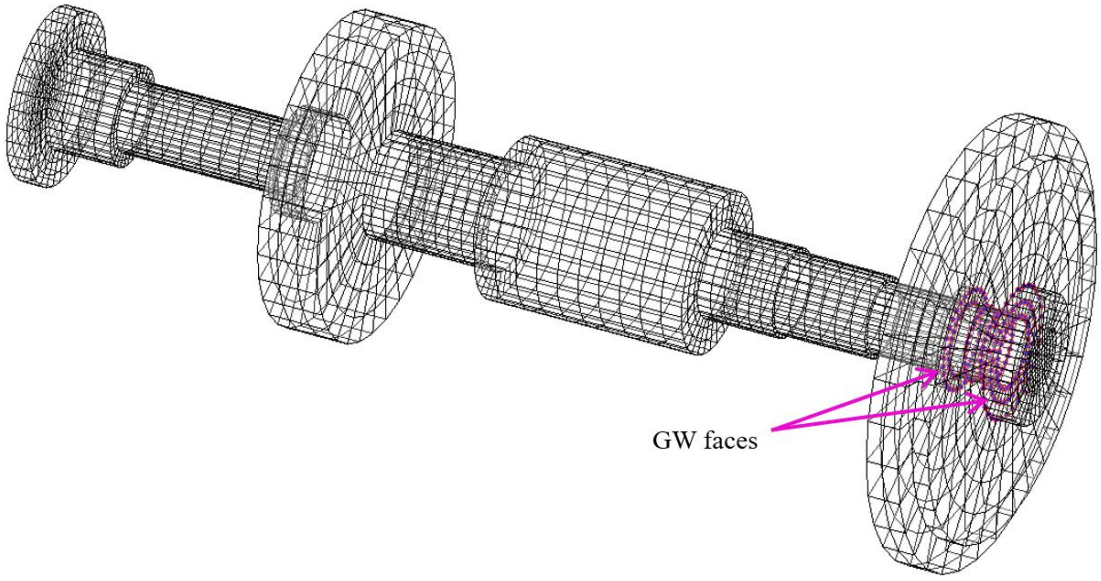

Figure 3.22 Contact nodes of the overhung type rotor-bearing system

The force term in Equation (3.33) is considered in the prediction model when the spin speed is nonzero, and Guyan reduction [75] is utilized for calculating eigenvalues. Three different interface conditions are evaluated, and the surface roughness parameters are listed in Table 3.4.

Table 3.4 Surface roughness parameters for the overhung rotor-bearing system

	R_s (μm)	η_s ($1/m^2$)	σ_s (μm)
Interface 1	1.0	1.0×10^{10}	1.0
Interface 2	1.0	1.0×10^{10}	2.0
Interface 3	1.0	1.0×10^{10}	3.0

The Campbell diagrams are plotted in Figure 3.23 and Figure 3.24 in rotor-fixed coordinates and inertial coordinates, respectively, using Equation (3.34) [22].

$$\omega_{fixed,forward} = \omega_{rotating,forward} + \Omega$$
$$\omega_{fixed,backward} = \omega_{rotating,backward} - \Omega \tag{3.34}$$

They are utilized to identify the critical speeds of the rotor-bearing system. The damped natural frequencies can be obtained in a similar way as described in Equation (3.15) with the reduced system matrices. The spin softening effect [22] and the linear bearing model in Figure 3.19 strongly influence the natural frequencies of the rotor with respect to spin speed. These effects amplify the deviation of the natural frequencies between the rotors with different levels of surface roughness as shown in Figure 3.25. Critical speeds of a rotor-bearing system in the rotor-fixed coordinate system can be determined as the speed

ranges where the damped natural frequencies encounter the horizontal axis [22]. In the present analysis, the critical speeds corresponding to the bending modes are considered. Figure 3.26 plots critical speeds versus preload for various levels of surface roughness in the rotor-bearing system. The critical speed increases 41.38 %, 36.69 %, and 33.33 % for Interface1, Interface2, and Interface3, respectively, over the given preload range. For 1000 kN preload, the relative differences between Interface1 and Interface2, Interface 2 and Interface 3, and Interface 1 and Interface 3 are 7.32 %, 5.26 %, 12.20 %, respectively.

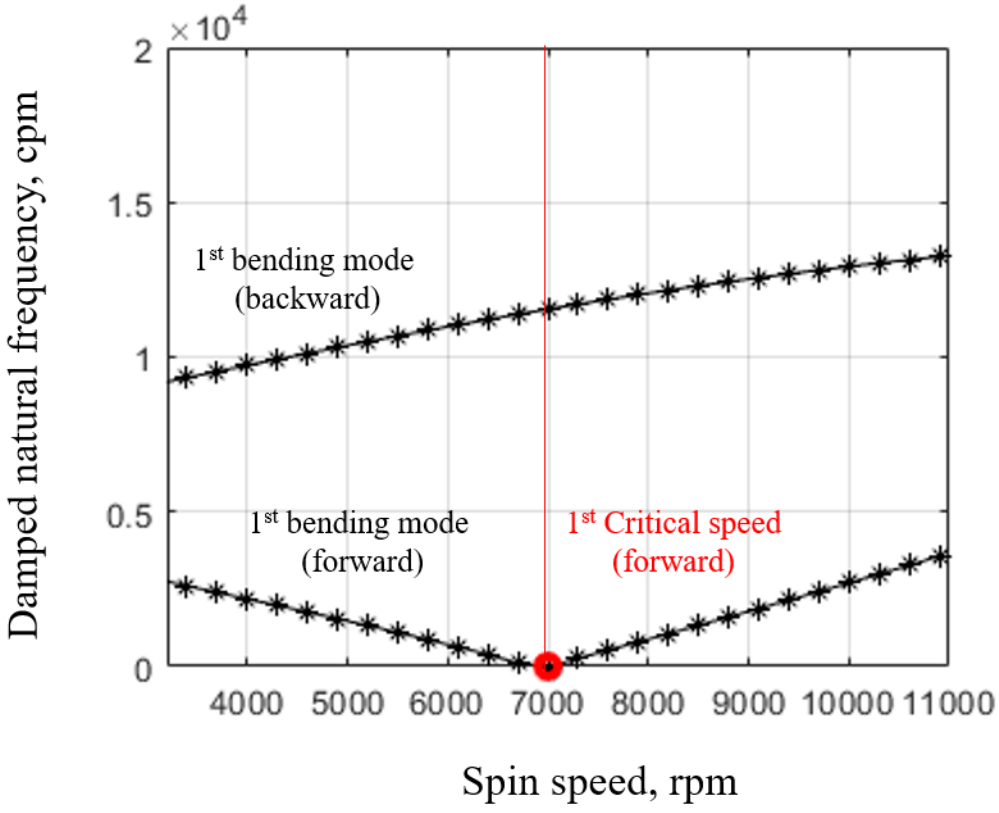

Figure 3.23 Damped natural frequency vs. spin speed in the rotor-fixed coordinates for interface model 2 in Table 4 with a 50 kN preload

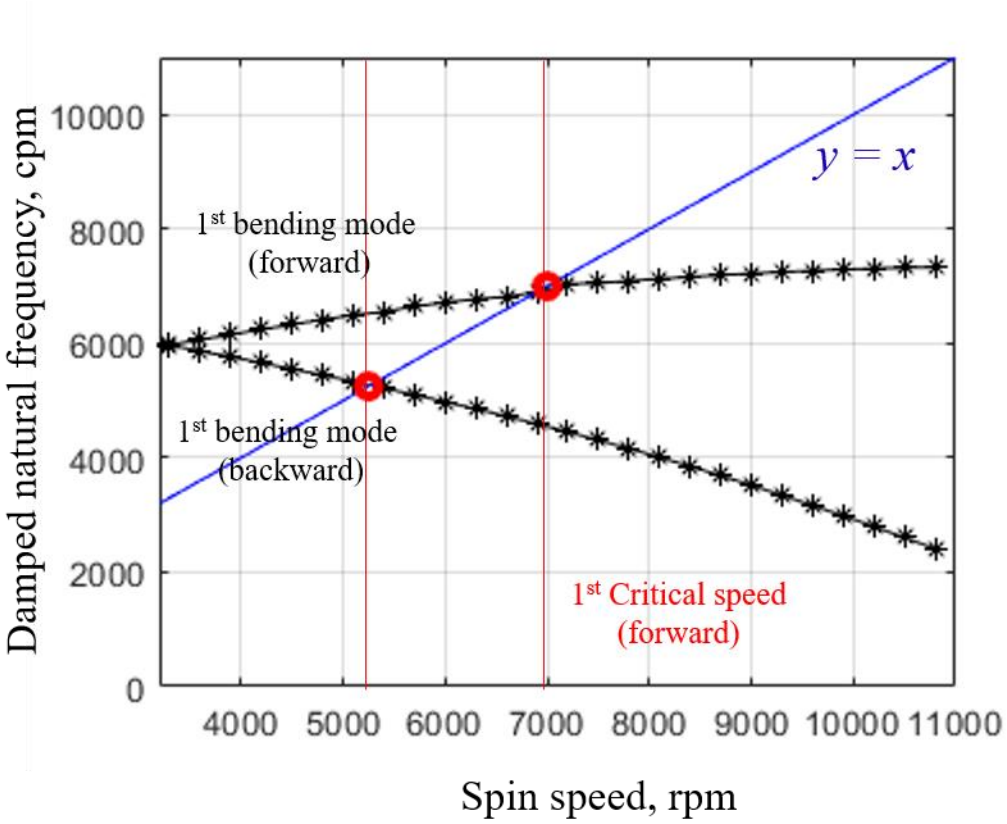

Figure 3.24 Damped natural frequency vs. spin speed in the inertial coordinates for interface model 2 in Table 4 with a 50 kN preload

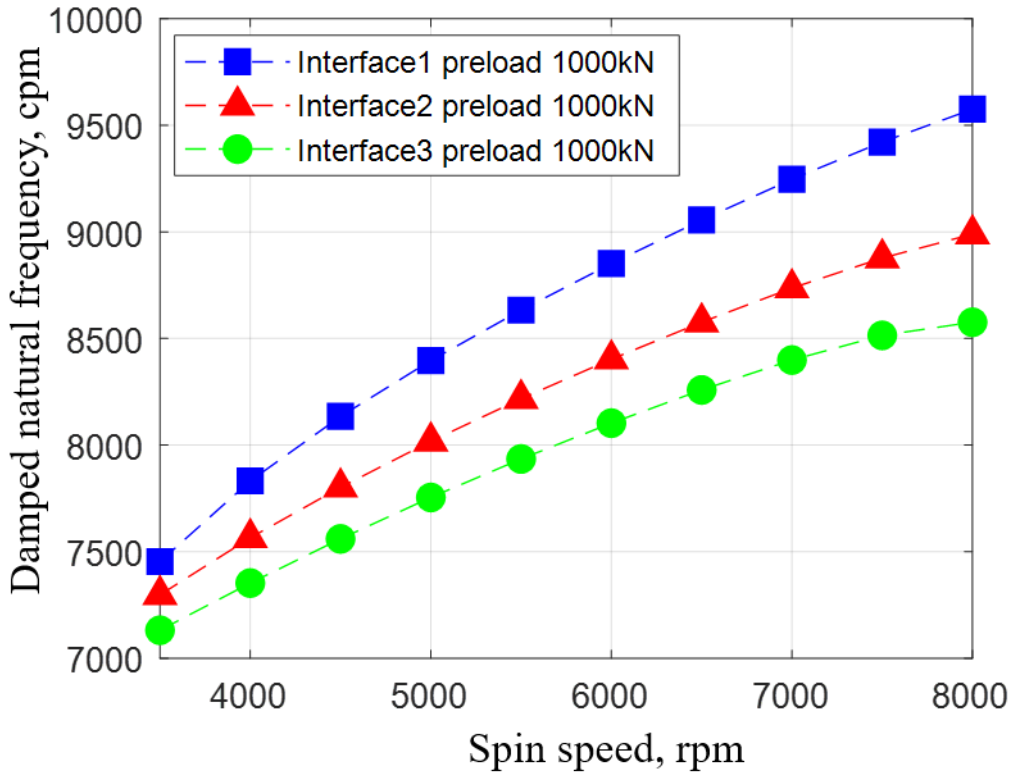

Figure 3.25 Damped natural frequency vs. spin speed vs. surface roughness at preload 1000 kN

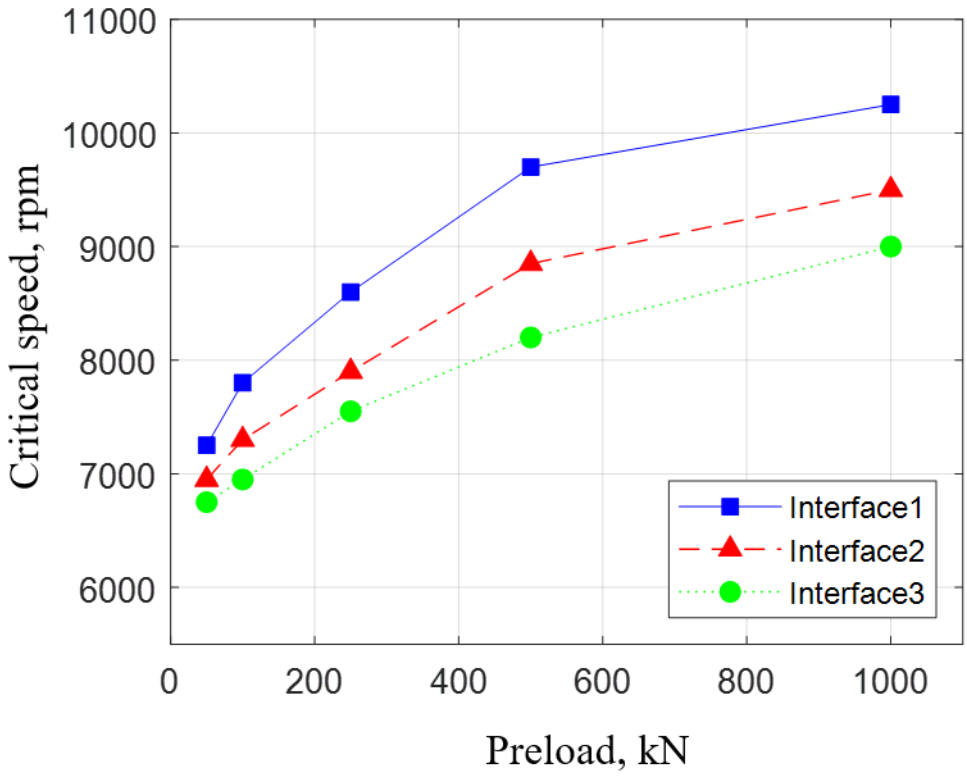

Figure 3.26 Critical speeds vs. preload for three interface models

3.5. Conclusion

The author presented a new high-fidelity, 3D solid element, finite contact method for the rotordynamic modeling of a rotor assembly with multiple preloaded parts and joints. A contact element for 3D solid finite element rotordynamic model was introduced, and a finite element formulation for the contact element was presented. The contact element can be used for direct applications of statistics-based contact theories to the 3D solid finite element rotordynamic model. A test rig was built to validate the proposed contact modeling method. Multiple configurations, for various degrees of

roughness at contact interfaces, were tested along with varying internal shaft preloads, and natural frequencies were measured. A prediction model for the test configurations was developed. An iterative calculation algorithm was introduced in order to solve the implicit equations between contact stiffness and stress distribution. Converged stress distributions of the rotor assembly, and contact stiffness at the interfaces in the test configurations were obtained for various degrees of interface roughness and preloads. Next, the natural frequencies of the rotor assembly were calculated and compared with the experimental results. The prediction results accurately follow the trend of the measurement with respect to the level of interface surface roughness and the increase of preloads. An overhung impeller type rotor bearing system simulation model was presented for demonstrating practical applications of the proposed modeling method. The simulation results demonstrate that the predicted critical speeds vary with respect to preload and contact surface roughness. The largest deviation of the predicted critical speeds between two different surfaces was 12.20 % for the rotor-bearing system.

4. STANDALONE 3D SOLID FINITE ELEMENT ROTORDYNAMIC (SFER) CODE

Although many commercial finite element codes provide finite element system matrices and their solutions for general structures, special treatments are necessary when it comes to rotating machinery with spin speeds [1]. Furthermore, in such cases of complicated algorithms with multiple computational steps, considering thermal and structural aspects of the structure simultaneously, an integrated finite element simulation environment is required. The integrated finite element simulation environment provides a comprehensive understanding of each step and deals with complex problem efficiently by minimizing communication traffic loads.

4.1. Element Matrices

4.1.1. Hexahedron Elements

8-node linear hexahedron elements are one of the common elements for finite element analyses along with 10-node quadratic tetrahedron elements. This element is also called brick element. The element satisfies acceptable accuracy in broad ranges of applications with good computational efficiency [76]. The detailed derivation can be found in several finite element text books [9]. The hexahedron elements are used to generate structured mesh of rotor structures.

A simple geometry annular steel shaft is used to validate the hexahedron finite element code as shown in Figure 4.1. The outer diameter of the shaft is 50.8 mm, the inner diameter of the shaft is 25.4 mm, and the axial length of the shaft is 609.6 mm.

Nominal values for elastic modulus and Poisson's ratio of 210 GPa and 0.3 are used in natural frequency calculation, respectively. Density of the shaft is obtained by measured mass of the shaft: 7.27 kg. The calculated results by SFER and the measured results are compared for the 3 lowest natural frequencies, and the values are listed in Table 4.1. The average error is within 2.0 %. The detailed information of the measurement devices are provided in 'Test Apparatus' of Chapter 3.

Figure 4.1 Photo of the simple annular steel shaft

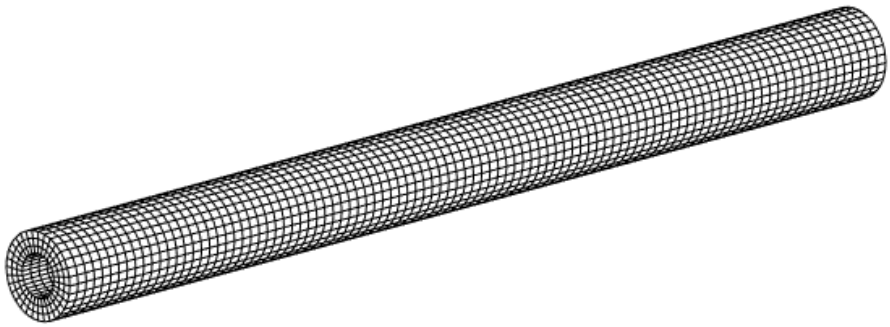

Figure 4.2 Hexahedron finite element mesh for the simple annular steel shaft

Table 4.1 Comparison between experimenta and SFER

	Experiment	SFER	Error
1st bending mode (Hz)	683.9	672.0	1.7%
2nd bending mode (Hz)	1807.0	1770.2	2.0%
3rd bending mode (Hz)	3340.0	3272.3	2.0%
Average			1.9%

4.1.2. Tetrahedron Elements

10-node quadratic tetrahedron elements are employed in solid finite element modeling of the code. Tetrahedron element is widely used in the area of finite element modeling with its advantage of automatic mesh generation with unstructured mesh. A 10-node quadratic tetrahedron element contains 10 nodes and 6 faces. There is a simpler tetrahedron element, which is called linear tetrahedron with 4 nodes. Using linear tetrahedron can reduce computation load for it has smaller number of node. However, linear tetrahedron is considered improper finite element in structural analysis. On the contrary, 10-node quadratic tetrahedron elements show robust performance in finite element analysis [76]. There are several commercial meshing software available, such as ANSYS Meshing, ICEM CFD, Gambit, SolidWorks, and MATLAB.

The developed 10-node quadratic tetrahedron solid finite element model are validated by comparing with two other methods and linear tetrahedron model. Two different spinning speed range are used for validation of rotordynamic analysis

performance. Circular pipe with 0.1m outer diameter, 0.05m inner diameter and 1m length is modeled by 4-kind method: Timoshenko beam, ANSYS, 4-node tetrahedron, 10-node tetrahedron.

Table 4.2 10-node tetrahedron element validation (0 rpm)

	Timoshenko	ANSYS brick	4-node Tetrahedron	4-node w.r.t. Beam	4-node w.r.t. ANSYS	10-node Tetrahedron	10-node w.r.t. Beam	10-node w.r.t. ANSYS
1st bending	29057	29056	29708	2.2%	2.2%	28493	1.9%	1.9%
1st bending	29060	29064	29740	2.3%	2.3%	28602	1.6%	1.6%
2nd bending	75327	75198	77225	2.5%	2.7%	74041	1.7%	1.5%
2nd bending	75377	75222	77358	2.6%	2.8%	74312	1.4%	1.2%
3rd bending	137674	136308	141136	2.5%	3.5%	135274	1.7%	0.8%
3rd bending	137926	136356	141838	2.8%	4.0%	135588	1.7%	0.6%
4th bending	212334	206616	200513	5.6%	3.0%	207438	2.3%	0.4%
4th bending	213037	206700	216323	1.5%	4.7%	207797	2.5%	0.5%
1st torsional	94297	93900	99443	5.5%	5.9%	94054	0.3%	0.2%
2nd torsional	190924	187800	200513	5.0%	6.8%	189514	0.7%	0.9%
AVG				**3.3%**	**3.8%**		**1.6%**	**1.0%**

Table 4.3 10-node tetrahedron element validation (5000 rpm)

	Timoshenko	ANSYS brick	4-node Tetrahedron	4-node w.r.t. Beam	4-node w.r.t. ANSYS	10-node Tetrahedron	10-node w.r.t. Beam	10-node w.r.t. ANSYS
1st bending	28887	28882	30263	4.8%	4.8%	28700	0.7%	0.6%
1st bending	29231	29240	29959	2.5%	2.5%	28365	3.0%	3.0%
2nd bending	75047	74856	77742	3.6%	3.9%	74471	0.8%	0.5%
2nd bending	75658	75564	77125	1.9%	2.1%	73860	2.4%	2.3%
3rd bending	137409	135810	141969	3.3%	4.5%	135831	1.1%	0.0%
3rd bending	138192	136860	141152	2.1%	3.1%	135011	2.3%	1.4%
4th bending	212200	205974	217703	2.6%	5.7%	208085	1.9%	1.0%
4th bending	213171	207342	216894	1.7%	4.6%	207133	2.8%	0.1%
1st torsional	94297	93900	99442	5.5%	5.9%	93919	0.4%	0.0%
2nd torsional	190924	187806	200511	5.0%	6.8%	189443	0.8%	0.9%
AVG				**3.3%**	**4.4%**		**1.6%**	**1.0%**

Table 4.2 and Table 4.3 show the validation result with 0 rpm and 5000 rpm of spinning speed respectively. 10-node tetrahedron element shows better performance than 4-node tetrahedron element and it has 1.6% and 1.0% differences from Timoshenko beam model and ANSYS model respectively.

An experiment is set up to validate the developed solid finite element code. The shaft-disk assembly was built mainly for the validation of the Morton code of VCEL as shown in Figure 4.3. The free-free vibration test results are exploited to validate SFER code. The test rotor weighs 365.83 lbs (165.94 kg). The rotor is hung by a pair of ropes and excited by an impact hammer. The corresponding acceleration data is obtained by an accelerometer, and an FFT analyzer is used to obtain the natural frequencies of the rotor.

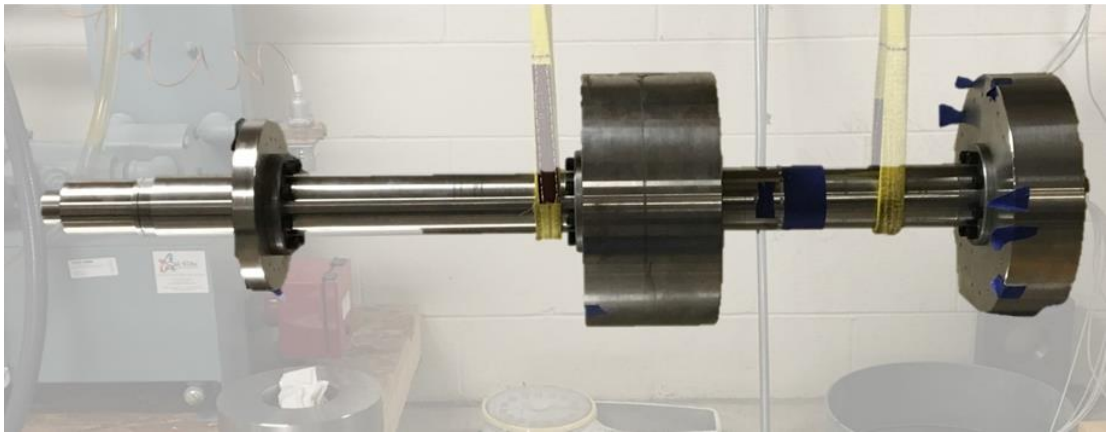

Figure 4.3 Photo of Morton test rotor (free-free vibration test)

To develop a numerical FE model, a 3D solid drawing is developed as shown in Figure 4.4. Then the drawing is imported to generate quadratic tetrahedron element mesh.

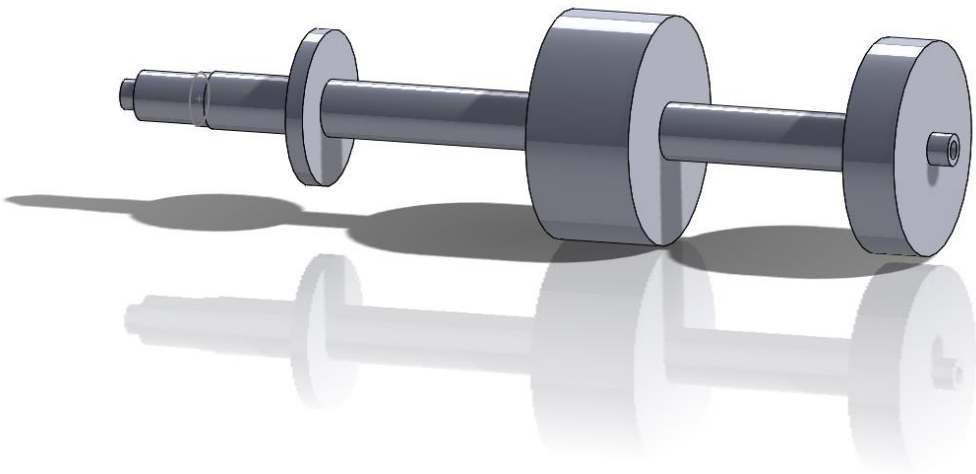

Figure 4.4 3D drawing for Morton test rotor

Figure 4.5 plots a grid test of the test rotor by SFER code. It shows that the 4 lowest natural frequencies of the bending modes tend to converge around 80,000 dofs.

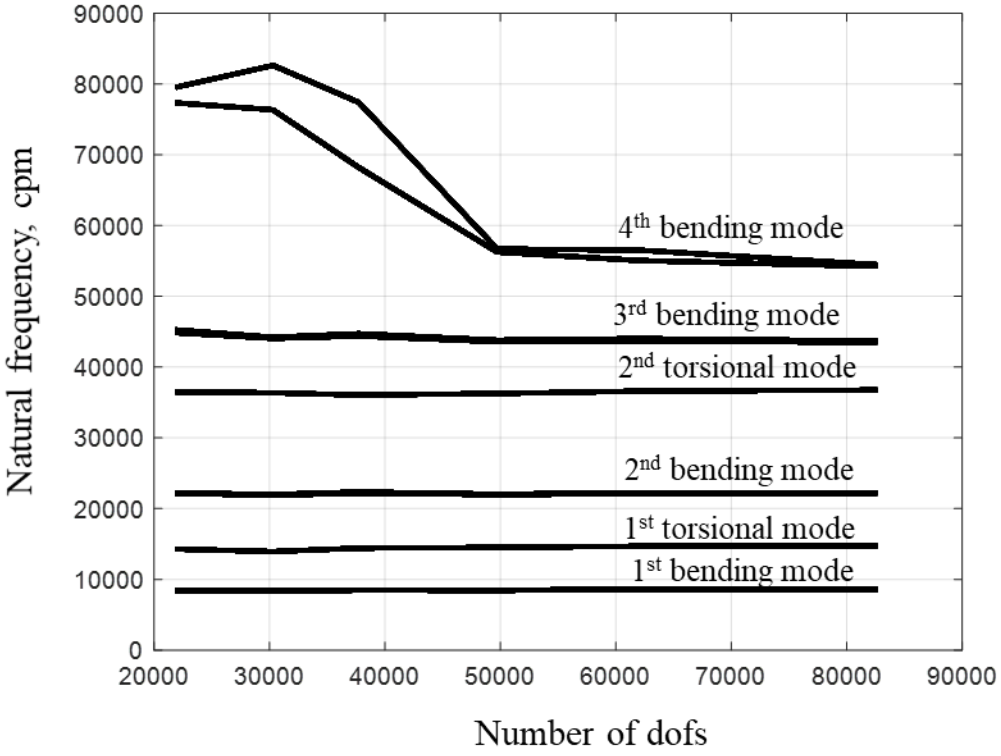

Figure 4.5 Grid test for Morton test rotor SFER results

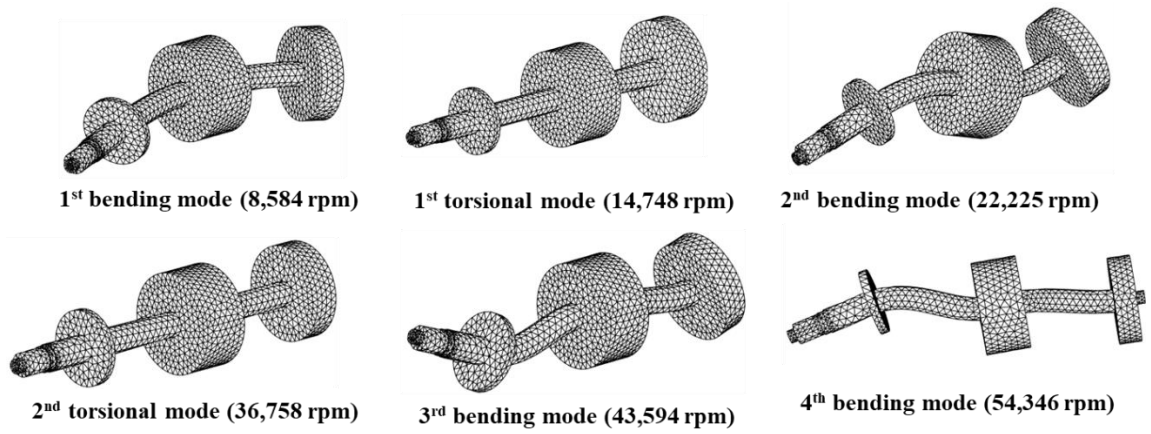

Figure 4.6 Mode shapes of Morton test rotor

Table 4.4 Comparison between SFER and measurement for Morton rotor

	Experiment	SFER	error
1st bending mode	146 Hz	143 Hz	2.0 %
2nd bending mode	389 Hz	370 Hz	4.8 %
3rd bending mode	687 Hz	727 Hz	5.8 %
4th bending mode	893 Hz	906 Hz	1.4 %
Average Error		3.5%	

As shown in Figure 4.6, mode shapes of the test rotor are plotted to distinguish each mode from the calculated natural frequencies, and the converged results are illustrated. Table 4.4 shows the comparison results between experimental measurement data and the calculated results from SFER code, and the average error is within 3.5 %.

4.2. Multiphysics Analysis Algorithm

Solid finite element model accounts for the detailed geometrical characteristics of the complex-shaped rotor. In addition, this approach may also improve accuracy of the numerical model by considering thermal and stress distribution of the rotor in regard

to rotordynamic analyses. As illustrated in Figure 4.7, thermal and stress distribution of the rotor affects the rotordynamic behavior of rotor-bearing systems, and these effects can be explained by adopting stress-stiffening effect. There are various sources that have the rotor thermally assorted within itself. Temperature variation within the rotor induces thermal expansion and thermal stress. Besides, centrifugal stress and preloads introduce stress distribution of the rotor. These various sources of stress within the rotor are taken in the form of stress-stiffness into the system stiffness matrix as shown in equation (3.32).

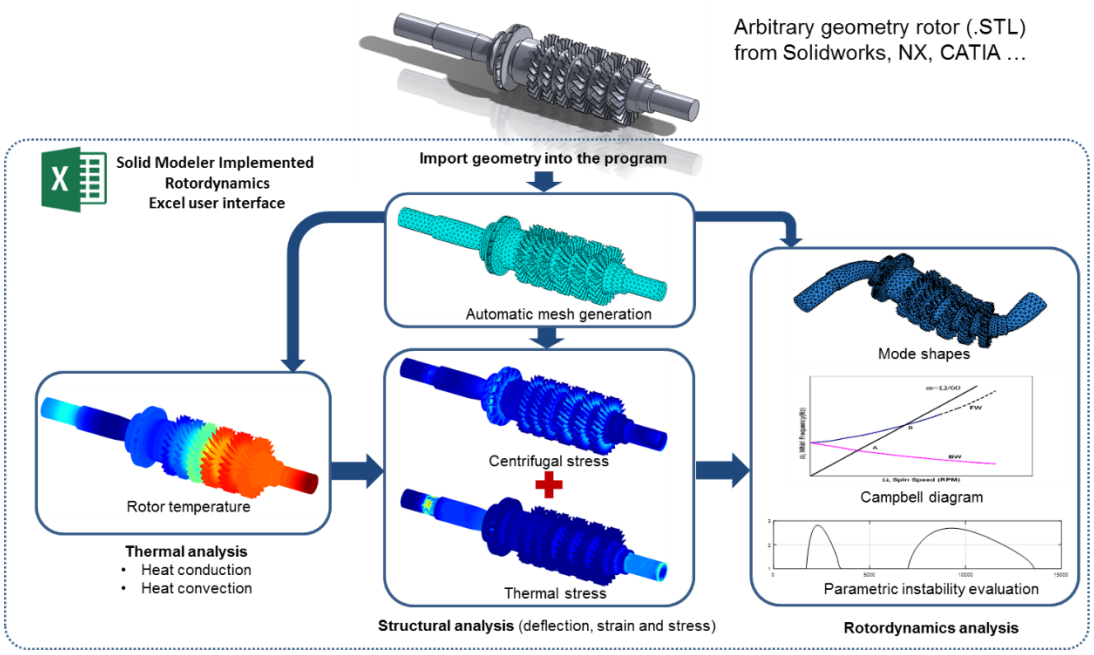

Figure 4.7 Flowchart for Multiphysics rotordynamic analysis

4.3. Floquet Method

The theoretical derivation of Floquet method is provided in section 2.2.1. This section is intended to provide specific details of the implementation of Floquet method into the code.

4.3.1. Integration Algorithm

The selection of the reference coordinate differs the algorithm significantly. Properly isolated time-variant coefficients may enhance overall computational efficiency in the code. In order to evaluate stability of the system, it is required to obtain $\underline{\boldsymbol{H}}_M(K)$, the discretized Monodromy matrix in equation (2.37), is reproduced as,

$$\underline{\boldsymbol{H}}_{\boldsymbol{M}}(K) = \underline{\boldsymbol{I}}_N exp\left(\Delta_K \underline{\boldsymbol{B}}_K\right) exp\left(\Delta_{K-1} \underline{\boldsymbol{B}}_{K-1}\right) \cdots exp\left(\Delta_1 \underline{\boldsymbol{B}}_1\right) \tag{4.1}$$

$\underline{\boldsymbol{B}}_K$ is calculated n_K times according to the number of discretization. The number n_K should be determined after convergence tests. Equations (2.31) and (2.36) are also recalled as follows.

$$\underline{\boldsymbol{B}}(t) = \begin{bmatrix} \underline{\mathbf{0}}_N & \underline{\boldsymbol{I}}_N \\ -\left(\underline{\boldsymbol{M}}^R\right)^{-1} \underline{\boldsymbol{K}}^R(t) & -2\Omega\left(\underline{\boldsymbol{M}}^R\right)^{-1} \underline{\boldsymbol{C}}^R(t) \end{bmatrix} \tag{4.2}$$

$$\underline{\boldsymbol{B}}_k = \frac{1}{\Delta_k} \int_{t_{k-1}}^{t_k} \underline{\boldsymbol{B}}(s) ds \tag{4.3}$$

As the time-variant components of the reduced system matrices are trigonometric functions, solutions exist for the integration of equation (4.3), vanishing numerical integration. The integration of equation (4.3) may be dissembled into four parts:

$$\underline{\boldsymbol{B}}_k = \frac{1}{\Delta_k}\begin{bmatrix} \int_{t_{k-1}}^{t_k} \underline{\mathbf{0}}_N ds & \int_{t_{k-1}}^{t_k} \underline{\boldsymbol{I}}_N ds \\ -\int_{t_{k-1}}^{t_k} \left(\underline{\boldsymbol{M}}^R\right)^{-1} \underline{\boldsymbol{K}}^R(s) ds & -2\Omega \int_{t_{k-1}}^{t_k} \left(\underline{\boldsymbol{M}}^R\right)^{-1} \underline{\boldsymbol{C}}^R(s) ds \end{bmatrix} \tag{4.4}$$

Each integration for the four parts proceeds as

$$\underline{\boldsymbol{B}}_k = \frac{1}{\Delta_k}\begin{bmatrix} \underline{\mathbf{0}}_N & \underline{\boldsymbol{I}}_N \Delta_k \\ -\left(\underline{\boldsymbol{M}}^R\right)^{-1} \int_{t_{k-1}}^{t_k} \underline{\boldsymbol{K}}^R(s) ds & -2\Omega\left(\underline{\boldsymbol{M}}^R\right)^{-1} \int_{t_{k-1}}^{t_k} \underline{\boldsymbol{C}}^R(s) ds \end{bmatrix} \tag{4.5}$$

$\underline{\boldsymbol{K}}^R(s)$ and $\underline{\boldsymbol{C}}^R(s)$ in equation (4.7) are time-variant and their minimum period is 2Ω. Hence, they can be rewritten as $\underline{\boldsymbol{K}}^R(2\Omega s)$ and $\underline{\boldsymbol{C}}^R(2\Omega s)$. $\underline{\boldsymbol{K}}^R(2\Omega s)$ can be decomposed by $\underline{\boldsymbol{K}}_0{}^R$, $\underline{\boldsymbol{K}}_c{}^R(2\Omega s)$, and $\underline{\boldsymbol{K}}_s{}^R(2\Omega s)$.

$$\underline{\boldsymbol{K}}^{\boldsymbol{R}}(2\Omega s) = \underline{\boldsymbol{K}}_0^R + \underline{\boldsymbol{K}}_c^R(2\Omega s) + \underline{\boldsymbol{K}}_s^R(2\Omega s) \tag{4.6}$$

Likewise, $\underline{\boldsymbol{C}}^R(2\Omega s)$ can be decomposed by $\underline{\boldsymbol{C}}_0{}^R$, $\underline{\boldsymbol{C}}_c{}^R(2\Omega s)$, and $\underline{\boldsymbol{C}}_s{}^R(2\Omega s)$.

$$\underline{\boldsymbol{C}}^{\boldsymbol{R}}(2\Omega s) = \underline{\boldsymbol{C}}_0^R + \underline{\boldsymbol{C}}_c^R(2\Omega s) + \underline{\boldsymbol{C}}_s^R(2\Omega s) \tag{4.7}$$

Then,

$$\int_{t_{k-1}}^{t_k} \underline{\boldsymbol{K}}^R(2\Omega s)ds = \underline{\boldsymbol{K}}_0^R\Delta_k + \int_{t_{k-1}}^{t_k} \underline{\boldsymbol{K}}_c^R(2\Omega s)ds + \int_{t_{k-1}}^{t_k} \underline{\boldsymbol{K}}_s^R(2\Omega s)ds \tag{4.8}$$

$$\int_{t_{k-1}}^{t_k} \underline{\boldsymbol{C}}^R(2\Omega s)ds = \underline{\boldsymbol{C}}_0^R\Delta_k + \int_{t_{k-1}}^{t_k} \underline{\boldsymbol{C}}_c^R(2\Omega s)ds + \int_{t_{k-1}}^{t_k} \underline{\boldsymbol{C}}_s^R(2\Omega s)ds \tag{4.9}$$

Using equations (2.25) and (2.26), the solutions of (4.8) and (4.9) can be easily obtained. The program code performs the above integration repeatedly in a loop until it gets $\underline{\boldsymbol{H}}_M(K)$. One of the advantages of this approach is the fixed discretization size, which enables parallel calculations of n_K of $\underline{\boldsymbol{B}}_K$, improving computational efficiency significantly.

4.4. Contact Model

Multi-domains of a rotor structure can interact with various types of connection in the finite element model. In this work, 3 different methods are introduced: the rigid connection using kinematic constraint equations, the penalty method, and the asperity contact method. Besides, 2 types of mesh interface: conformal mesh interface and non-conformal mesh interface are discussed in the following sub-sections. Besides, thermal contact resistance model is developed and verified as well.

4.4.1. Rigid Connection

Rigid contact is intended to depict connection between two rigid surfaces. Since the surfaces are rigid, no deformation is expected during the contact. Thus, the connection is defined by kinematic constraint equations. The derivations of constraint equations and transformation matrix are given by the references [9, 11]. Using the constraint equations inevitably introduces reduced system matrices. Hence, the total number of dofs are reduced and it may result in additional multiplication computations during the integration of the multi-physics results. Different sizes of each system may lead unexpected errors in the code. To the author's experience, using constraint equations in the complex multi-physics rotordynamic models may not be recommended except some unavoidable processes, such as rotor-bearing connections with rigid planes.

4.4.2. Contact Node Search Algorithm

For the contact in a finite element model, it is important to determine contact locations [77]. Due to the nature of the discretized geometrical definitions of the finite element model using elements, faces, and nodes, the corresponding contact nodes at interfaces should be properly selected to prevent loss of accuracy in prediction. There are mainly two types of mesh interfaces: conformal mesh interface and non-conformal mesh interface. Both types are discussed in the following sections.

4.4.2.1. Conformal Mesh Interface

Conformal mesh interface can be defined as whose nodes at the interface of two different domains are coincident. An example of the structure composed of two rectangular beams is given for illustration as shown in Figure 4.8. The mesh is generated for each domain, keeping conformity at the interface as illustrated in Figure 4.9 and Figure 4.10. Some special treatments are required to ensure the conformity at interfaces during mesh generation for unstructured mesh. Many commercial tools, for example, ANSYS Meshing, ANSYS ICEM, GAMBIT, etc., provide this function along with some open-source meshers, such as Gmsh. Although contact algorithm for conformal unstructured mesh is provided in this study, the developed code does not offer functions to generate conformal unstructured mesh at the moment. Whereas, conformal structure mesh is mainly used and provided by the code, which is to be discussed in the following sections.

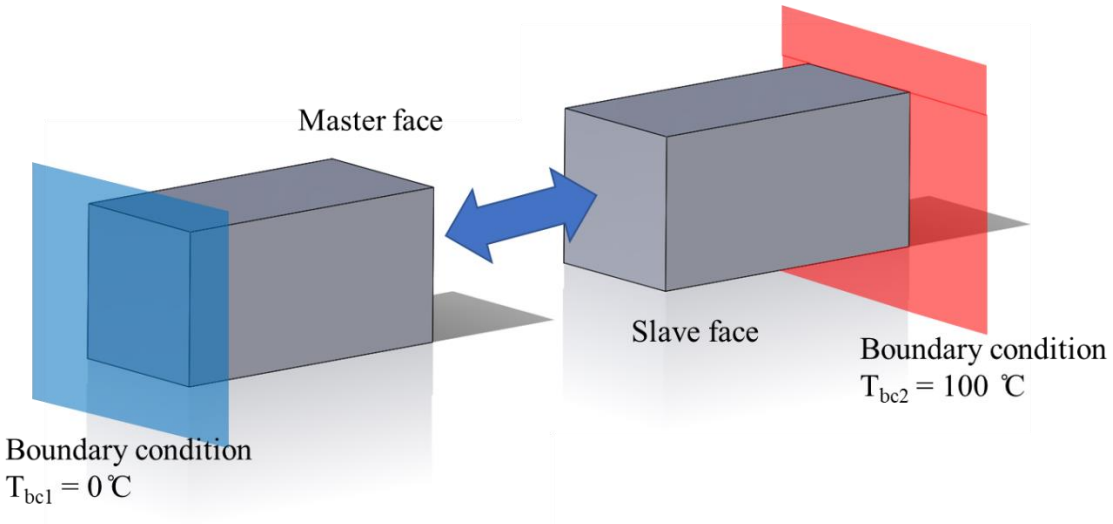

Figure 4.8 Drawing of a structure with two different domains in contact

In order to find the contact nodes at interface an algorithm called ‘contact node search algorithm’ is used. The algorithm searches the contact nodes based on geometrical proximity. The tolerance for the algorithm can be set as a certain ratio corresponding the mesh size.

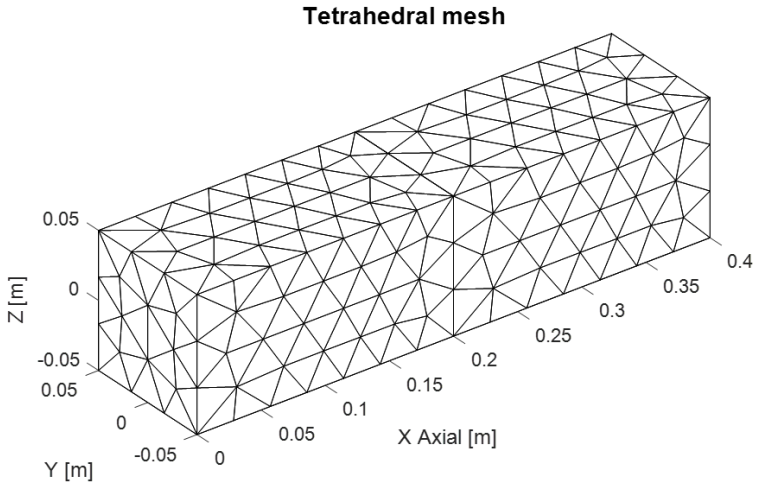

Figure 4.9 Mesh of a structure with two different domains in contact

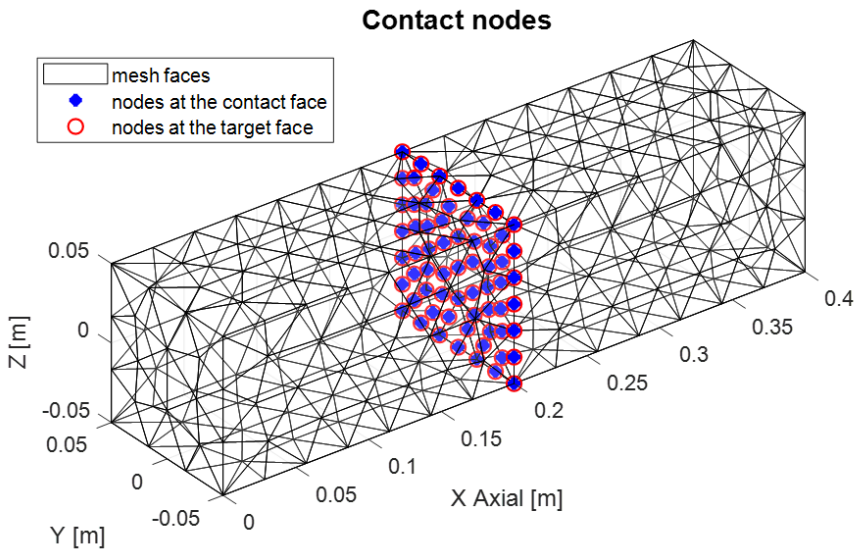

Figure 4.10 Contact nodes at interface of a structure with two different domains in contact

The boundary conditions set as fixed temperature to both ends as shown in Figure 4.8 and Figure 4.11. The constant temperature at x=0.0 m location is set as 0˚C and 100˚C at x = 0.4 m.

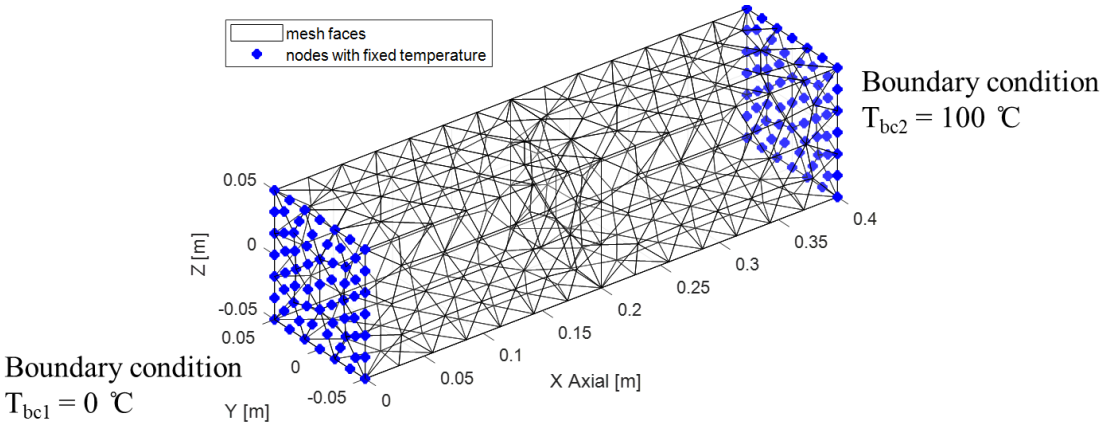

Figure 4.11 Fixed temperature boundary conditions for multi-domain square beam structure with conformal mesh interface

Figure 4.12 presents temperature distributions without and with the constraint equations between two beams. Without the constraint equations, two beams behave as separated bodies. On the other hand, the case where the constraint equations are applied shows smooth temperature gradient through the connected bodies.

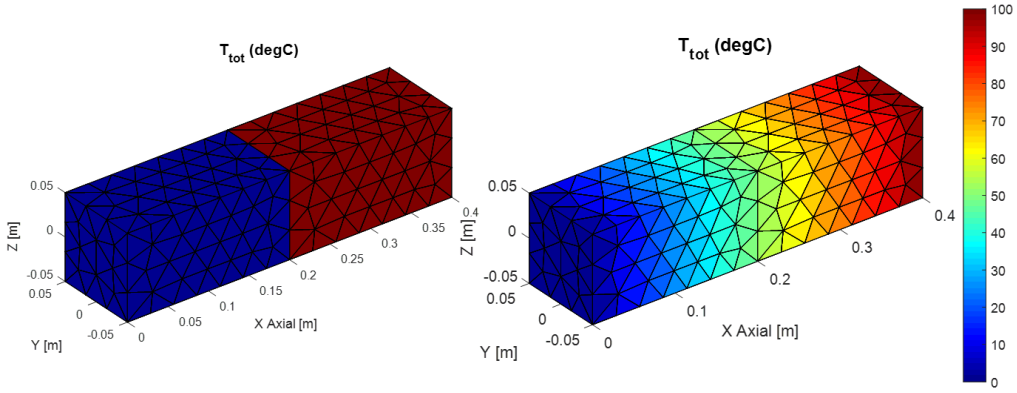

Figure 4.12 Temperature distribution for an integrated multi-domain structure

The connection algorithm for displacement field variables can also be built in the similar manner. Basic concepts are identical to thermal analysis except displacement field variables have x,y and z direction degree of freedoms while temperature field variables do not have directional degree of freedoms. Figure 4.13 and Figure 4.14 show 3D solid finite element model with displacement variable connection algorithm and its verification.

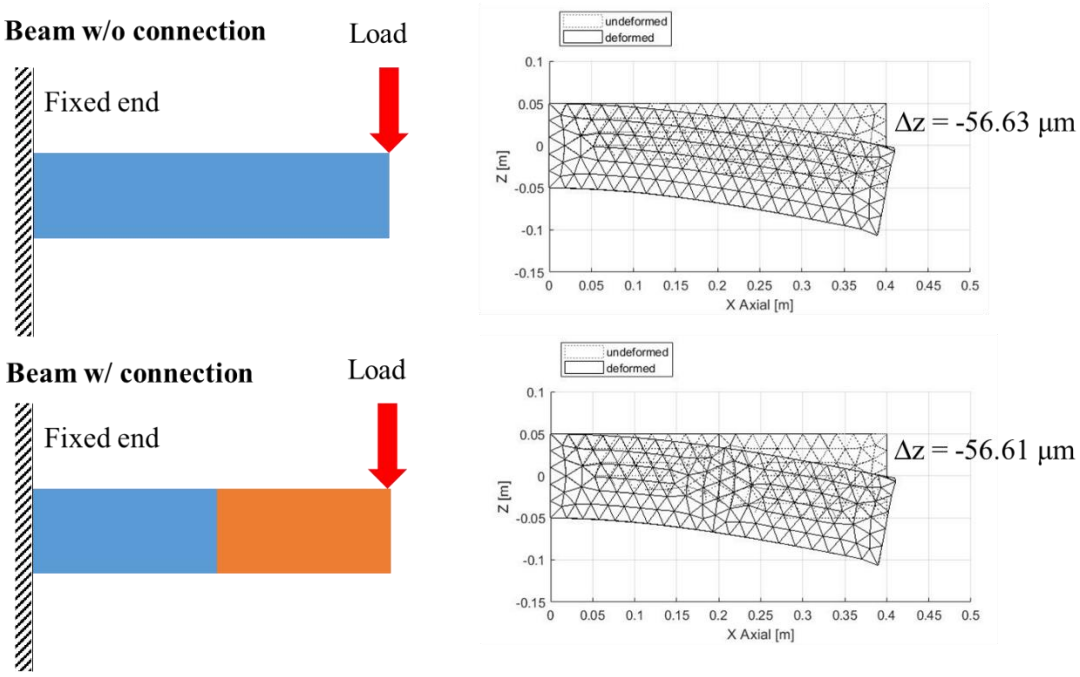

Figure 4.13 Displacement field integration for a multi-domain beam structure

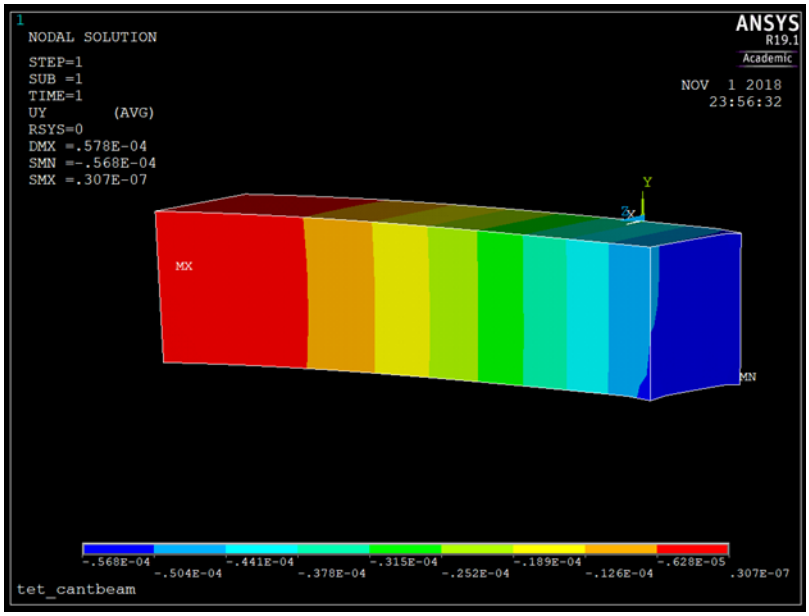

Figure 4.14 Displacement results from ANSYS APDL

Table 4.5 Comparison between monolithic structure and multi-domain interpolated structure from ANSYS APDL and SFER

	Δz (μm)	Error (%)
Monolithic structure (ANSYS APDL)	-56.80	-
Monolithic structure (SFER)	-56.63	0.3 %
Multi-domain interpolated structure (SFER)	-56.61	0.3 %

4.4.2.2. Non-Conformal Mesh Interface

For more general cases where the contact nodes are not coincident, non-conformal mesh, an interpolation method should be used to define the relations between the nodes at two different domains. Element shape functions can be used to interpolate field variables of the multi-domains. For 10-node quadratic tetrahedron element is used

in isoparametric assumption, inherently quadratic integration functions are used to generate constraint equations for non-coincident contact nodes.

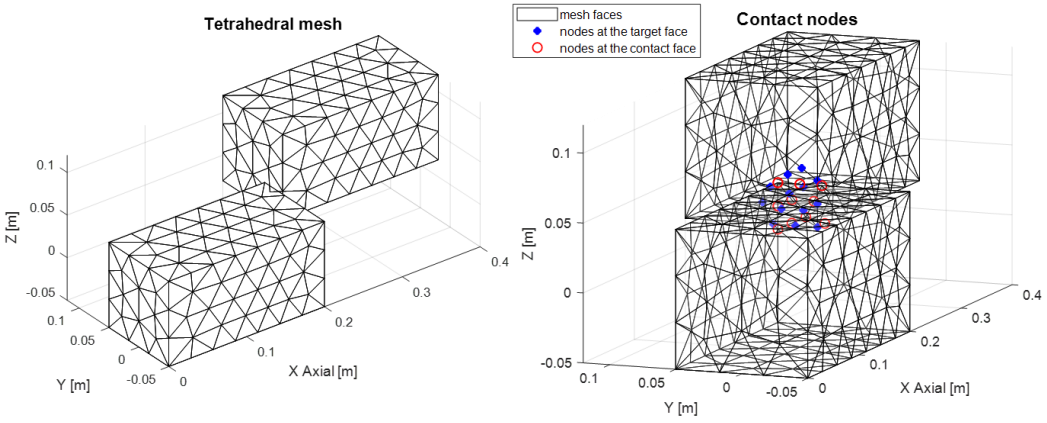

Figure 4.15 Non-conformal mesh interface

A misaligned set of square beams are designed to demonstrate non-conformal mesh interface as shown in Figure 4.15. As a first step, contact faces should be determined by the contact node search algorithm. The contact search algorithm searches a set of nodes based on their proximity.

$$abs(\underline{\boldsymbol{x}}_{i1} - \underline{\boldsymbol{x}}_{i2}) < tol_{int} \tag{4.10}$$

where $\underline{\boldsymbol{x}}_{i1}$, $\underline{\boldsymbol{x}}_{i2}$, and tol_{int} mean the surface nodes at one domain of the interface, the surface nodes at the counter domain of the interface, and tolerance of node distance, respectively. A loop for the entire surface nodes obtains the contact nodes within the defined distance. With the obtained set of nodes, a group of contact faces can also be

collected. Figure 4.16 illustrates a method to find the corresponding surface in the counter domain for a contact node.

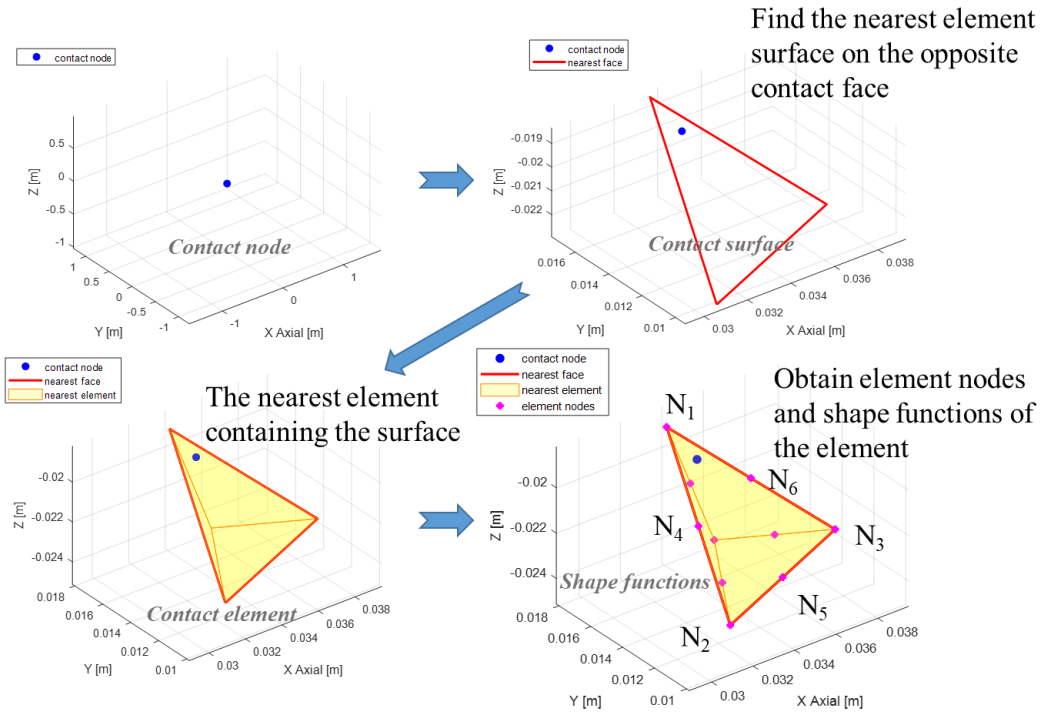

Figure 4.16 Non-conformal mesh interface contact algorithm

When it comes to planar connect as in Figure 4.15, the contact nodes at both domains lie in a flat plane. Thus, the previously described method can be directly applied. Figure 4.17 plots a temperature distribution for the geometry shown in Figure 4.15.

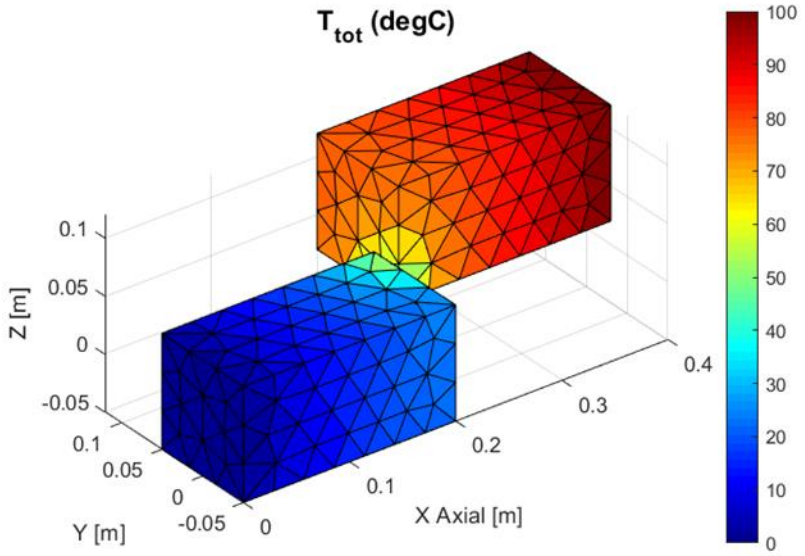

Figure 4.17 Temperature distribution

However, there should be another step for a non-planar contact, such as cylindrical contact, which is a common case for rotating machinery. For a non-planar contact case, a contact node is projected onto the counter face, generating an additional projected node as shown in Figure 4.18. Let a pair of a contact node and the corresponding counter face be found by the contact node search algorithm. A normal vector of the face can also be chosen. Following the vector, a projected node can be generated on the face from the contact node. The projected node is also exploited as a criterion to exclude the corresponding contact node as shown in Figure 4.19. The figure describes two different cases P_1 and P_2. The contact node search algorithm corresponds both P_1 and P_2 to a single face. The projected node from P_1 lies on the face, while the one from P_2 does not.

This additional step filters collected contact nodes, excluding ones outside of the contact boundaries.

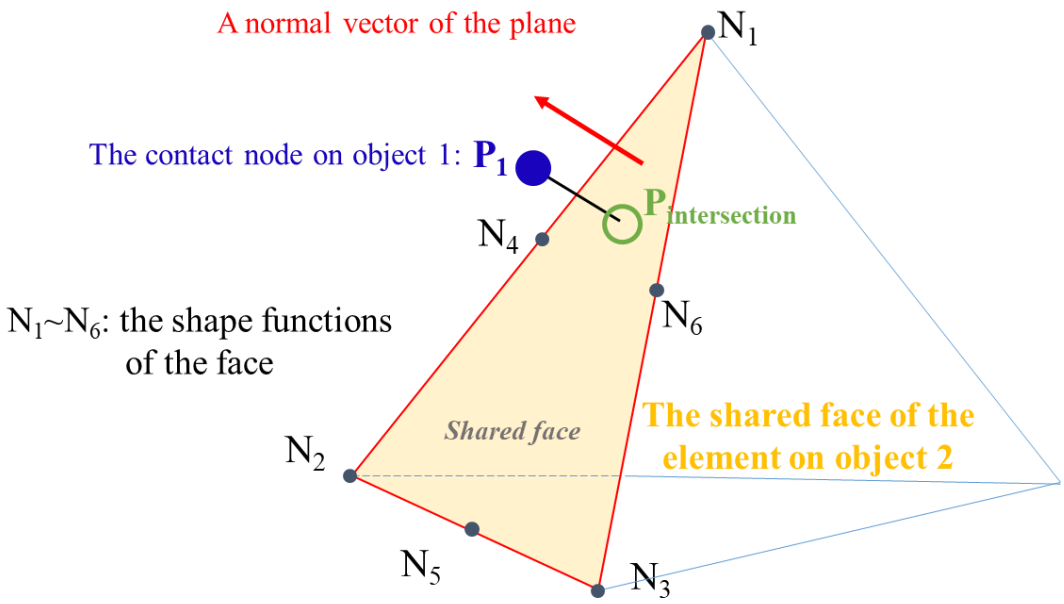

Figure 4.18 Inter-domain node projection for non-planar contact interfaces

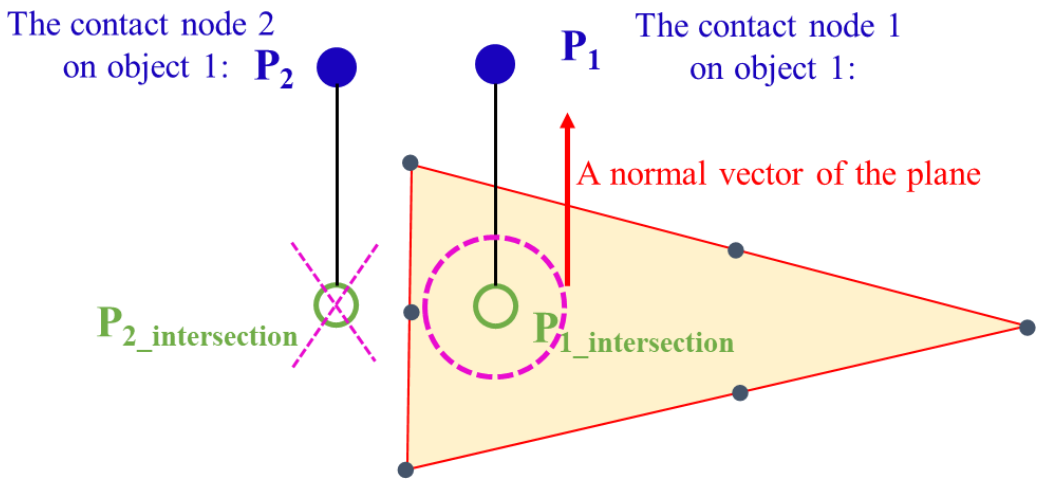

Figure 4.19 Contact node search algorithm using a projected node

As mesh gets refined, the projected distance between the contact node and the projected node decreases and the deviation between their field variables becomes small enough. Therefore, field variables can be determined by nodal values and shape functions. For example, the temperature of node P_1 in Figure 4.18 can be calculated as

$$T_{P_1} \approx T_{P_{intersection}} = N_1T_1 + N_2T_2 + N_3T_3 + N_4T_4 + N_5T_5 + N_6T_6 \qquad (4.11)$$

Figure 4.20 shows a cylindrical contact between a shaft and a disk. The two different domains do not coincide at the interface. The contact node search algorithm finds contact nodes at each domain. The contact nodes at the disk side are projected to the counter domain. Then, the constraint equations between the projected nodes and the corresponding facial nodes are established. Finally, the projected nodes are deducted from the total dofs so that the number of total dofs remains unchanged.

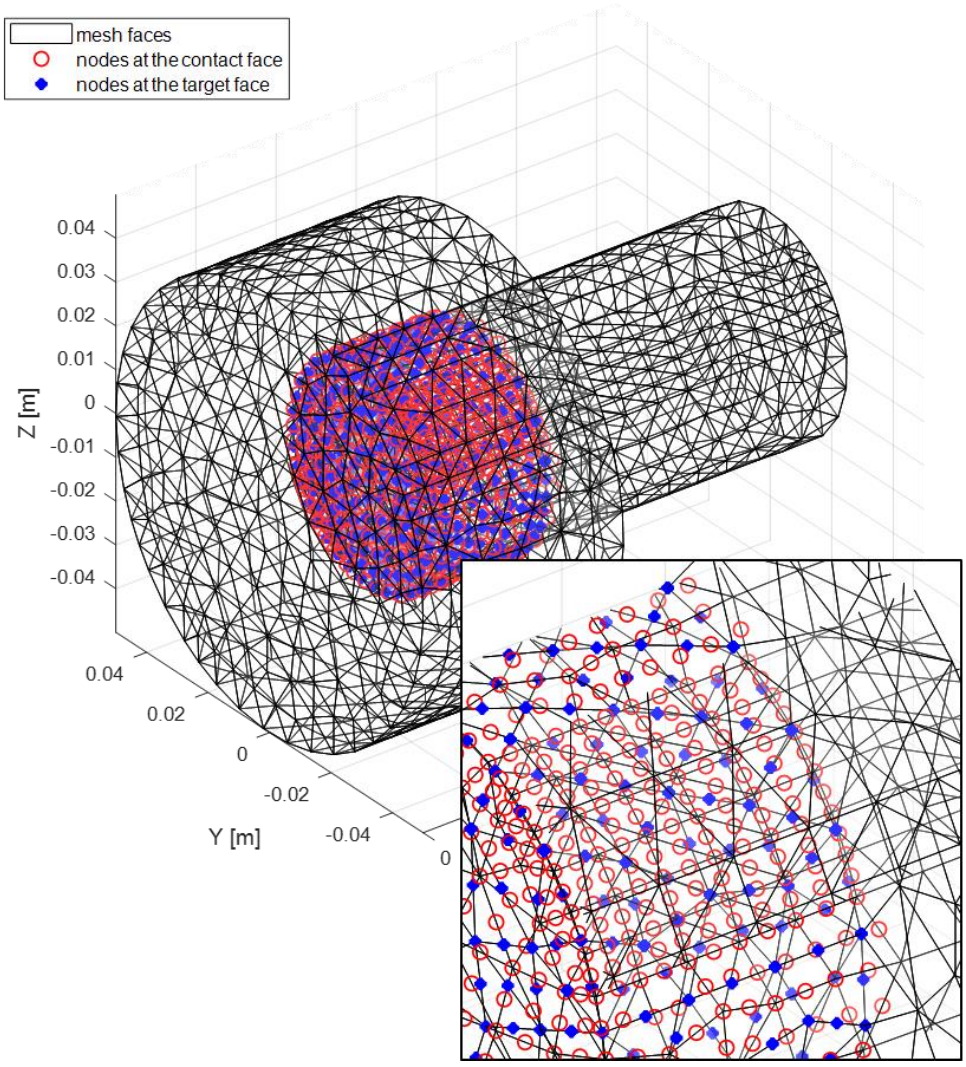

Figure 4.20 Cylindrical non-conformal contact mesh interface of a shaft-disk structure

In order to verify the non-conformal interpolation contact algorithm, two types of the same structure are compared: monolithic disk-shaft structure and interpolated two-domain disk-shaft structure. Figure 4.21 plots the temperature distributions for 3 different cases. The single-domain monolithic body plays a reference, and temperature value at point *P(0.1 m, 0 m, 0.025 m)* is compared to the multi-domain models. Table 4.6

lists the thermal properties of each case. The thermal properties of the impellers differ from one another, while the shaft maintain the same property for all the cases.

Table 4.6 Thermal properties of shaft-disk structures

	Thermal conductivity (W/m^2K)	**Thermal expansion coefficient (W/mK)**
Shaft and impeller for monolithic body	46	1.77E-05
Impeller for case 1 (99.5%)	45.77	1.76E-05
Impeller for case 2 (25.0%)	11.5	4.43E-06

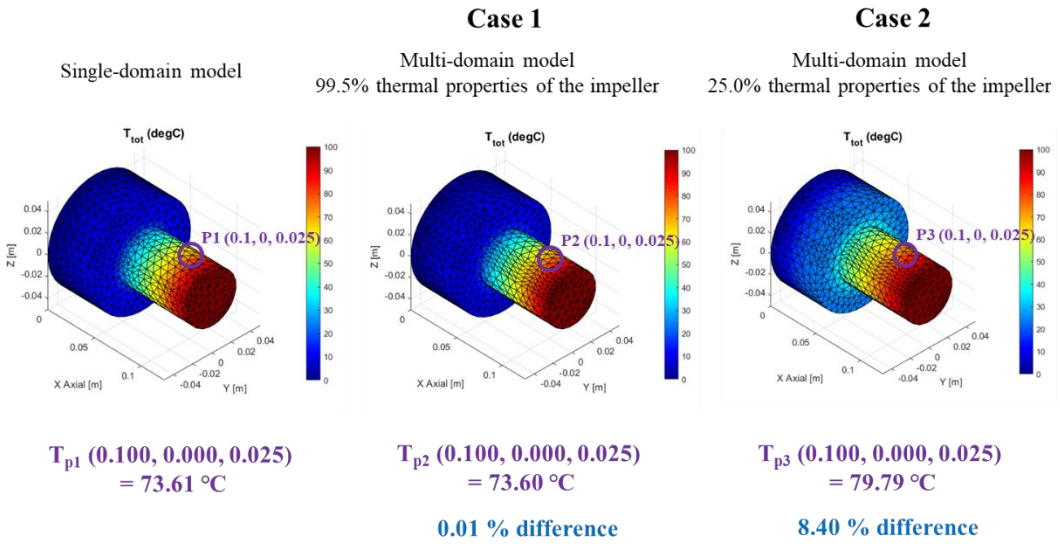

Figure 4.21 Temperature distributions for 3 types: monolithic single body, multi-domain with similar thermal properties, multi-domain with different thermal properties

Case 1 shown in Figure 4.21 plots a thermal contour similar to the one of the monolithic body, which implies the non-conformal mesh contact interpolation method connects two separated domains properly. 8.40 % deviation from the monolithic body's temperature at *P(0.1 m, 0 m, 0.025 m)* is seen in case 2 of the multi-domain model with different thermal properties.

4.4.3. Thermal contact resistance algorithm

When two objects are thermally connected, there may be thermal contact resistance which resists heat flow through interfaces [78]. Both conformal mesh interface and non-conformal mesh interface may include thermal contact resistance at their interface, and no constraint equation is used for both cases. In other words, thermal contact resistance separates the temperature variables of the two nodes at a contact point of two different domains. Including thermal contact resistance may improve the accuracy of the temperature prediction models.

4.4.3.1. Finite Element Formulation

The finite element formulation for the thermal contact resistance element can be derived from the potential energy of contact interface as [11]

$$\Pi_{tc}^{e} = \frac{1}{2}\int_{S_e} (T)^T \frac{1}{R_c{}^e}\, T dS_e = \frac{1}{2}\int_{S_e} \left(\underline{\boldsymbol{T}}^{\boldsymbol{e}}\right)^T \left(\underline{\boldsymbol{N}}_{\boldsymbol{i}}{}^{\boldsymbol{e}}\right)^T \frac{1}{R_c{}^e} \underline{\boldsymbol{N}}_{\boldsymbol{i}}{}^{\boldsymbol{e}}\, \underline{\boldsymbol{T}}^{e} dS_e$$
$$= \frac{1}{2}\left(\underline{\boldsymbol{T}}^{\boldsymbol{e}}\right)^T \int_{S_e} \left(\underline{\boldsymbol{N}}_{\boldsymbol{i}}{}^{\boldsymbol{e}}\right)^T \frac{1}{R_c{}^e} \underline{\boldsymbol{N}}_{\boldsymbol{i}}{}^{\boldsymbol{e}} dS_e\ \underline{\boldsymbol{T}}^{e} \tag{4.12}$$

where $\Pi_{tc}{}^{e}$, T, $\underline{\boldsymbol{T}}_{e}$, $R_c{}^{e}$, and $\underline{\boldsymbol{N}}_{i}{}^{e}$ are the potential energy of the thermal contact element, the temperature of the element, the element nodal temperature vector, the element thermal contact resistance for a unit area, and the element inter-domain shape function matrix, respectively.

$$\underline{\boldsymbol{h}}_{\boldsymbol{tc}}{}^{\boldsymbol{e}} = \int_{S_e} \left(\underline{\boldsymbol{N}}_{\boldsymbol{i}}{}^{\boldsymbol{e}}\right)^T \frac{1}{R_c{}^e} \underline{\boldsymbol{N}}_{\boldsymbol{i}}{}^{\boldsymbol{e}}\ dS_e \tag{4.13}$$

where $\underline{\boldsymbol{h}}_{tc}{}^{e}$ is the element thermal contact resistance matrix. The inter-domain shape function matrix defines the temperature field across the contact plane between two elements in contact. For the case of a conformal mesh on the contact plane, $\underline{\boldsymbol{N}}_{i}{}^{e}$ can be represented as

$$\underline{\boldsymbol{N}}_{i}{}^{e} = [-N_1 \quad \cdots \quad -N_{ns} | \, N_1 \quad \cdots \quad N_{ns}\,] \tag{4.14}$$

where ns is the number of face nodes, and N_1 and N_{ns} are the shape functions of the first node and ns^{th} node of the element, respectively. The element thermal contact resistance matrix is evaluated with the following Gauss quadrature formula [9]

$$\underline{\boldsymbol{h}}_{\boldsymbol{tc}}{}^{\boldsymbol{e}} = \sum_{\alpha=1}^{n_G}\sum_{\beta=1}^{n_G} w_\alpha w_\beta \underline{\boldsymbol{N}}^{\boldsymbol{e}}(\xi_{1\alpha},\xi_{2\beta})^T \frac{1}{R_c{}^e}\underline{\boldsymbol{N}}^{\boldsymbol{e}}(\xi_{1\alpha},\xi_{2\beta}) det\left(\underline{\boldsymbol{J}}(\xi_{1\alpha},\xi_{2\beta})\right) \quad (4.15)$$

where n_G is the number of Gauss quadrature integration points, $det(\underline{\boldsymbol{J}})$ is the determinant of the Jacobian matrix, $\xi_{1\alpha}$, $\xi_{2\beta}$ are Gauss quadrature integration points in the natural coordinate system and w_α, w_β are the corresponding weight factors.

4.4.3.2. Verification

The thermal contact resistance element developed in the preceding section is verified by analytical solutions. To make an analytical solution available, a simple cylindrical shaft structure is introduced as shown in Figure 4.22. The shaft is divided into two identical parts. The two separated shaft domains are in contact via thermal contact resistance. The thermal contact resistance coefficient, R_{ct} in unit of m^2K/W ranges from $1.0e^{-4}$ to $1.0e^{-1}$ in the following parametric study. Figure 4.23 draws the corresponding equivalent thermal circuit for the simple cylindrical shaft. Analytical solutions are obtained using the circuit and utilized as the reference values for verification of the developed thermal contact element. Table 4.7 lists properties of the assembly.

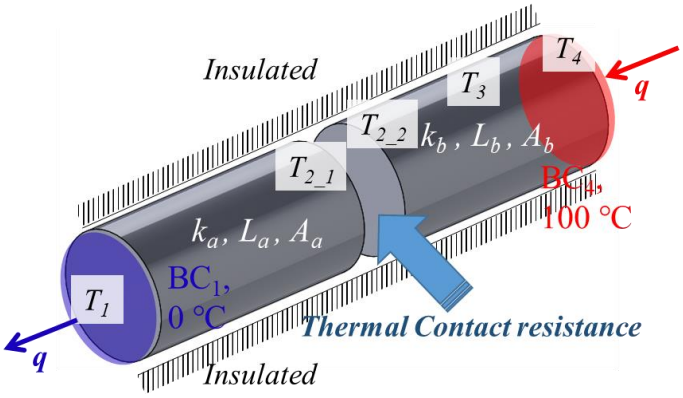

Figure 4.22 Simple cylindrical shaft structure assembly

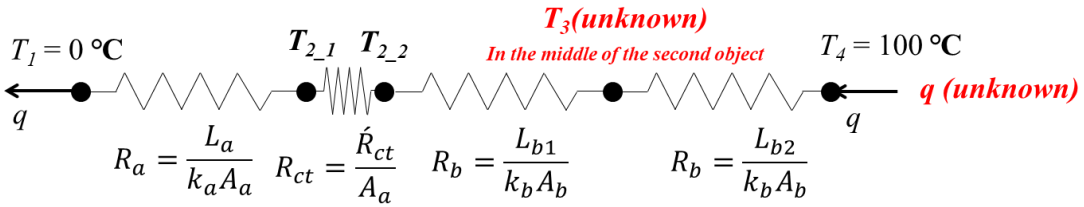

Figure 4.23 Equivalent thermal circuit for the simple cylindrical shaft structure assembly

Table 4.7 Properties of the simple cylindrical shaft structure

Part	**a**	**b1**	**b2**
Conductivity, *k* (W/mK)	60.5	15.125	15.125
Length, *L* (m)	0.1	0.05	0.05

Figure 4.24 plots temperature contours for four different thermal contact resistances: 1.0e^{-4} m^{2}K/W, 1.0e^{-3} m^{2}K/W, 1.0e^{-2} m^{2}K/W, 1.0e^{-1} m^{2}K/W. Temperature deviations become great as thermal contact resistance increases. Table 4.8 and Figure 4.25 compare

the results from the finite element analyses and preliminary solutions from the equivalent thermal circuit. The average difference is within 0.39%.

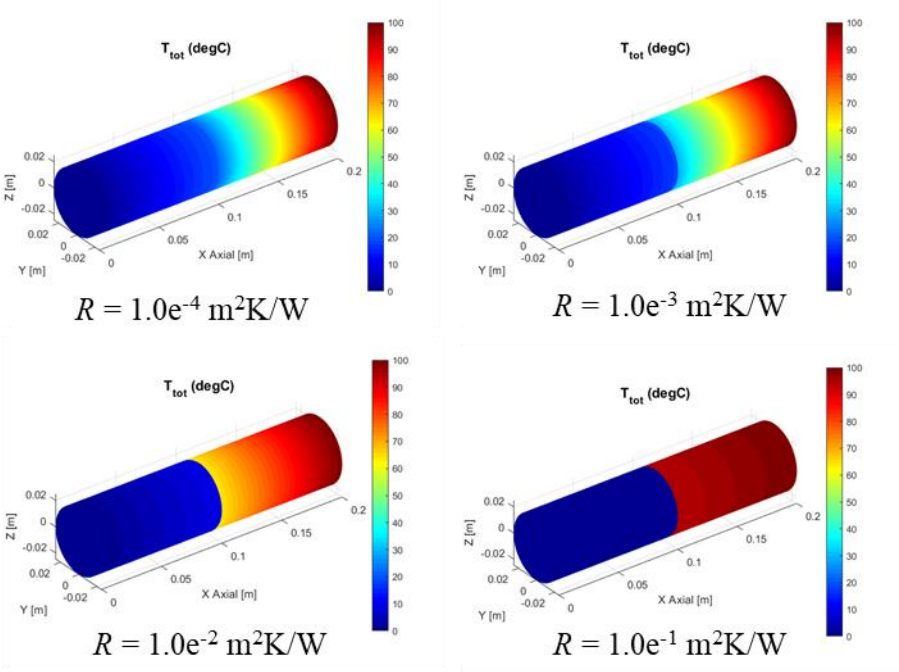

Figure 4.24 Temperature contours for various thermal contact resistances

Table 4.8 Comparison between FE model and preliminary solution from equivalent thermal circuit

Thermal contact resistance (K m²/W)	**1.00E-04**		**1.00E-03**		**1.00E-02**		**1.00E-01**	
	T3(degC)	q(W)	T3(degC)	q(W)	T3(degC)	q(W)	T3(degC)	q(W)
Preliminary solution	60.48	23.47	64.32	21.19	81.90	10.75	96.95	1.81
FE model	60.57	23.28	64.40	21.02	81.92	10.68	96.95	1.80
Error	0.15%	0.82%	0.12%	0.81%	0.02%	0.68%	0.00%	0.55%

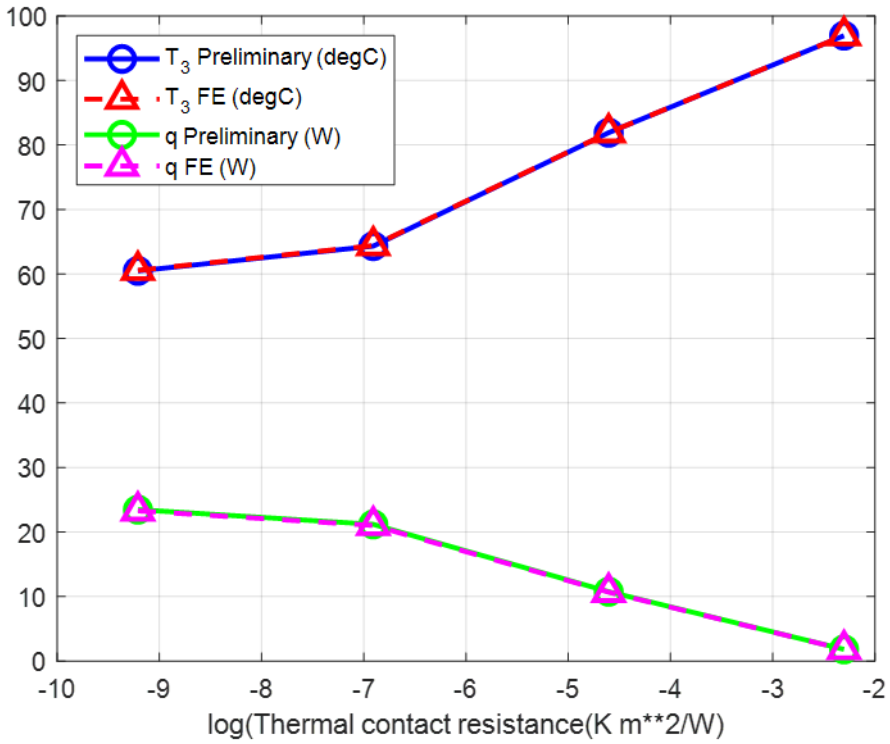

Figure 4.25 Comparison between FE model and preliminary solution from equivalent thermal circuit

4.4.4. Penalty-Based Contact Algorithm

A contact model based on the penalty method is developed. The penalty method is one of the contact modelling method using penalty number [11]. To derive the contact stiffness matrix and the contact force vector, a constraint equation is introduced as

$$\underline{\boldsymbol{t}} = \underline{\boldsymbol{C}} \cdot \underline{\boldsymbol{D}} - \underline{\boldsymbol{Q}} \tag{4.16}$$

where $\underline{\boldsymbol{t}}$, $\underline{\boldsymbol{C}}$, and $\underline{\boldsymbol{D}}$ are the indicator of violation for the impenetrate condition, the coefficient matrix, and the gap function vector, respectively. $\underline{\boldsymbol{t}} = \underline{\boldsymbol{0}}$ defines satisfaction of the constraints. And the potential energy function is augmented by a penalty function as

$$\boldsymbol{\Pi_p} = \frac{\mathbf{1}}{\mathbf{2}}\underline{\boldsymbol{D}}^{\boldsymbol{T}}\underline{\boldsymbol{K}}\,\underline{\boldsymbol{D}} - \underline{\boldsymbol{D}}^{\boldsymbol{T}}\underline{\boldsymbol{R}} + \frac{\mathbf{1}}{\mathbf{2}}\underline{\boldsymbol{t}}^{\boldsymbol{T}}\underline{\boldsymbol{\alpha}}\,\underline{\boldsymbol{t}} \tag{4.17}$$

where $\underline{\boldsymbol{t}}^{T}\underline{\boldsymbol{\alpha}}\,\underline{\boldsymbol{t}}$ /2 and $\underline{\boldsymbol{\alpha}}$ are the penalty function and a diagonal matrix of penalty number α_i. Then the stationary condition is

$$\frac{\partial \boldsymbol{\Pi_p}}{\partial \underline{\boldsymbol{D}}} = \mathbf{0} \tag{4.18}$$

By the chain rule,

$$\frac{\partial}{\partial \underline{\boldsymbol{D}}}\left(\frac{\mathbf{1}}{\mathbf{2}}\underline{\boldsymbol{t}}^{\boldsymbol{T}}\underline{\boldsymbol{\alpha}}\,\underline{\boldsymbol{t}}\right) = \frac{\partial \underline{\boldsymbol{t}}}{\partial \underline{\boldsymbol{D}}}\frac{\partial}{\partial \underline{\boldsymbol{t}}}\left(\frac{\mathbf{1}}{\mathbf{2}}\underline{\boldsymbol{t}}^{\boldsymbol{T}}\underline{\boldsymbol{\alpha}}\,\underline{\boldsymbol{t}}\right) = \underline{\boldsymbol{C}}^{\boldsymbol{T}}\underline{\boldsymbol{\alpha}}\,\underline{\boldsymbol{t}} = \underline{\boldsymbol{C}}^{\boldsymbol{T}}\underline{\boldsymbol{\alpha}}\,\left(\underline{\boldsymbol{C}}\cdot\underline{\boldsymbol{D}} - \underline{\boldsymbol{Q}}\right) \tag{4.19}$$

Hence, the stationary condition becomes

$$\frac{\partial \boldsymbol{\Pi_p}}{\partial \underline{\boldsymbol{D}}} = \left(\underline{\boldsymbol{K}} + \underline{\boldsymbol{C}}^{\boldsymbol{T}}\underline{\boldsymbol{\alpha}}\,\underline{\boldsymbol{C}}\right)\cdot\underline{\boldsymbol{D}} - \underline{\boldsymbol{R}} - \underline{\boldsymbol{C}}^{\boldsymbol{T}}\underline{\boldsymbol{\alpha}}\,\underline{\boldsymbol{Q}} = \mathbf{0} \tag{4.20}$$

$$\left(\underline{\boldsymbol{K}} + \underline{\boldsymbol{K}}_{\boldsymbol{c}}\right)\cdot\underline{\boldsymbol{D}} = \underline{\boldsymbol{R}} + \underline{\boldsymbol{R}}_{\boldsymbol{c}} \tag{4.21}$$

In equation (4.21),

$$\underline{\boldsymbol{K}_c} = \underline{\boldsymbol{C}^T}\,\underline{\boldsymbol{\alpha}}\,\underline{\boldsymbol{C}} \tag{4.22}$$

$$\underline{\boldsymbol{R}_c} = \underline{\boldsymbol{C}^T}\,\underline{\boldsymbol{\alpha}}\,\underline{\boldsymbol{Q}} \tag{4.23}$$

where $\underline{\boldsymbol{K}_c}$ and $\underline{\boldsymbol{R}_c}$ are the contact stiffness matrix and the contact force vector.

Figure 4.26 illustrates two domains in contact. Let the two domains overlap with a distance $-g_n$ between two arbitrary points at each domain. This penetrated condition is unrealistic and g_n should be always greater than or equal to zero.

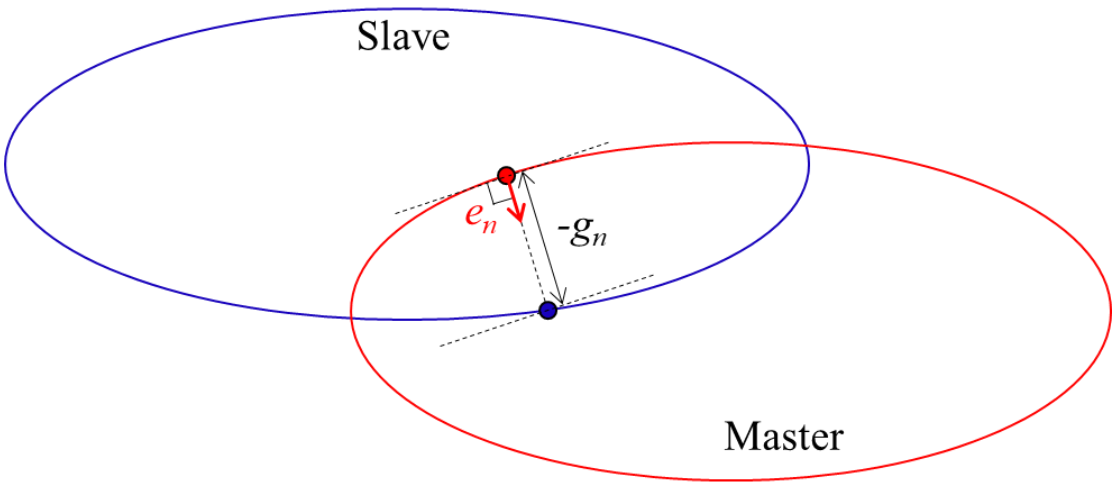

Figure 4.26 Two domains with penetration gap $-g_n$

Figure 4.27 depicts the contact stiffness and the contact forces between these two points in Figure 4.26. As defined in equations (4.22) and (4.23), the contact stiffness and the

contact force can be defined by penalty number. For a simple application, both terms are set as simple function of penalty number as

$$k_c = \alpha \tag{4.24}$$

$$f_c = \alpha g_n \tag{4.25}$$

The contact forces are exerted in the directions which reduces the penetration, while the contact stiffness resists the deformation due to the contact forces as described in Figure 4.27.

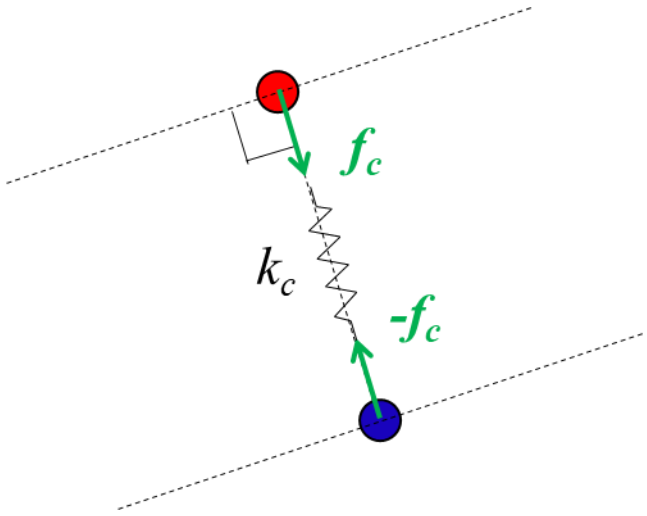

Figure 4.27 Contact model schematic with contact stiffness and contact forces

As an implement of the contact model, a rectangular beam shaft is utilized as shown in Figure 4.28. An overlap between the two shafts is set by locating them at certain positions manually. The contact nodes can be found by the contact node search

algorithm. Figure 4.29 illustrates the contact dynamics at the interface. The deformed structure by the application of the penalty method is plotted in Figure 4.30. The axial contact force distribution is plotted in Figure 4.31, and the calculated stress are compared with the one from ANSYS APDL simulation. ANSYS APDL calculates the maximum Von Mises stress as 8.11 GPa, while SFER predicts 8.12 GPa, which is within acceptable deviation ranges for a different numerical code.

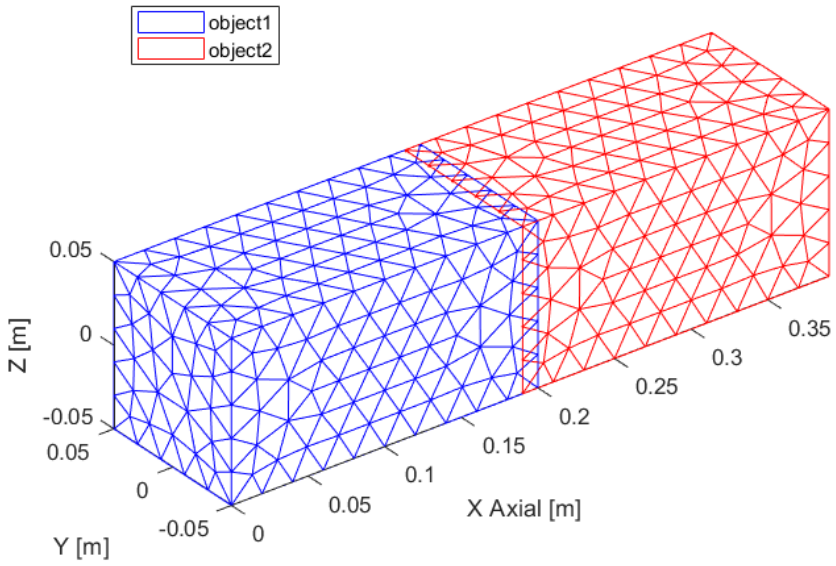

Figure 4.28 Rectangular beams with planar contact interface (penetrate condition)

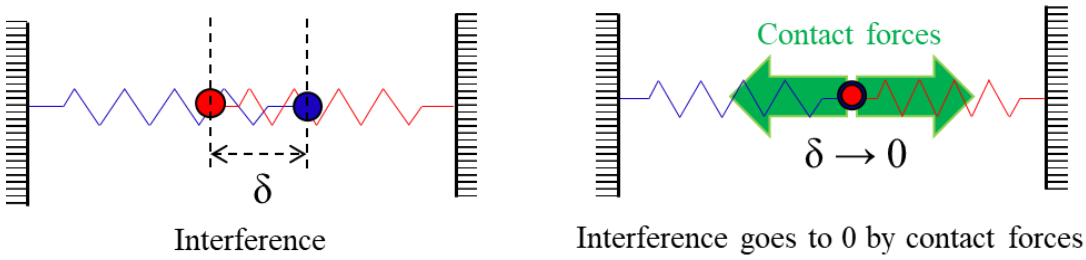

Figure 4.29 Schematic diagram for the rectangular beams with planar contact interface

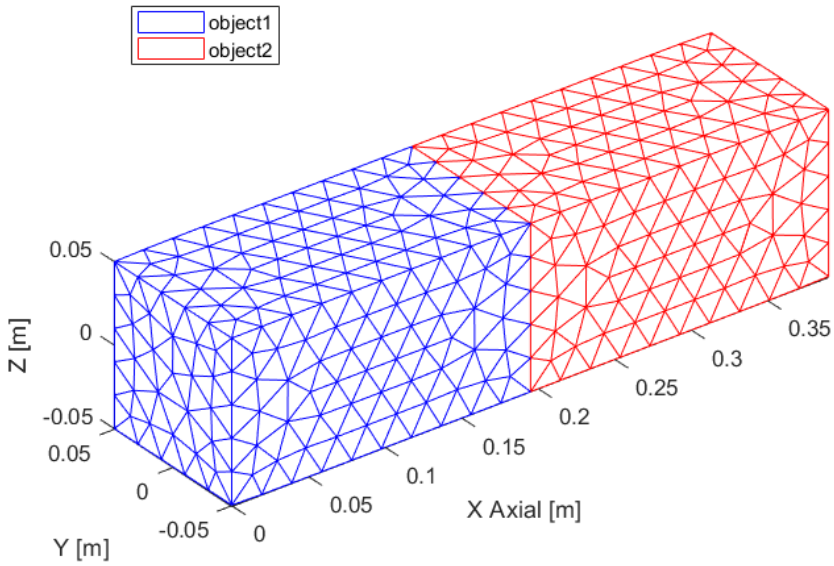

Figure 4.30 Rectangular beams with planar contact interface (impenetrate condition)

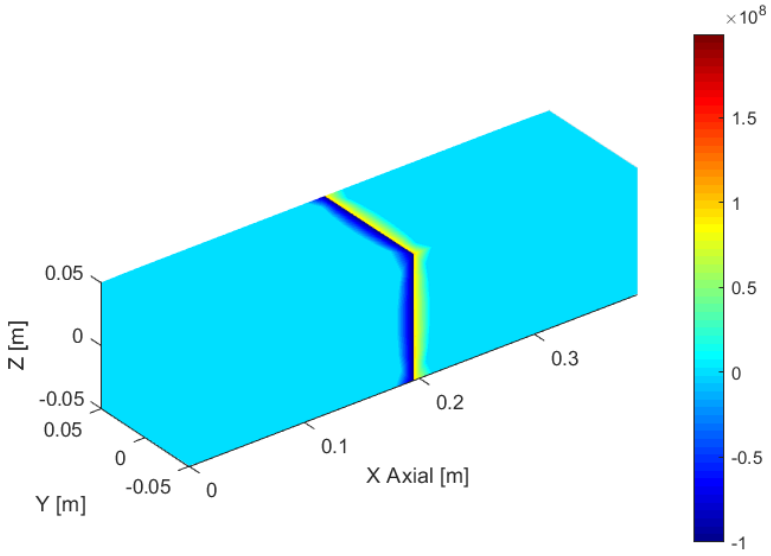

Figure 4.31 Axial force distribution of the rectangular beam assembly

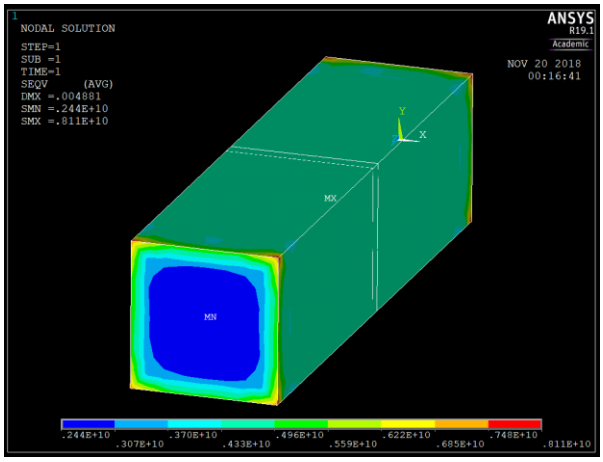

Figure 4.32 ANSYS APDL Von Mises stress distribution for the rectangular beam assembly

The contact model is applied to a cylindrical interface, such as shaft-disk assemblies as shown in Figure 4.33 and Figure 4.34. The shaft and the disk are assembled by interference fit. The penalty method is utilized to satisfy the impenetrate condition for

the assembly. Although the penalty algorithm satisfies the impenetrate condition within a tolerance, the stress distribution of the shaft-disk assembly may be undesirable as plotted in Figure 4.35. The irregularly distributed contact stress may be caused by the unstructured mesh and non-conformal mesh at the interface.

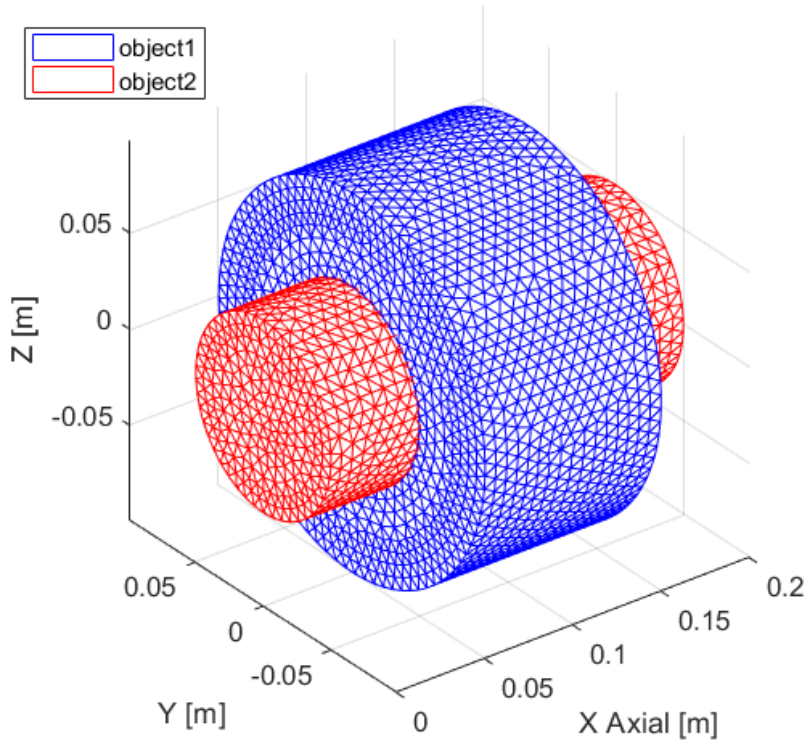

Figure 4.33 Shaft-disk assembly with interference fit

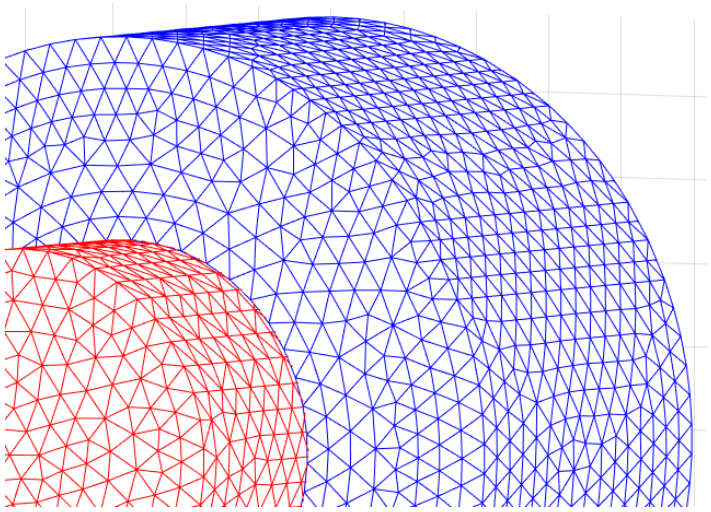

Figure 4.34 Shaft-disk assembly with interference fit (zoom in)

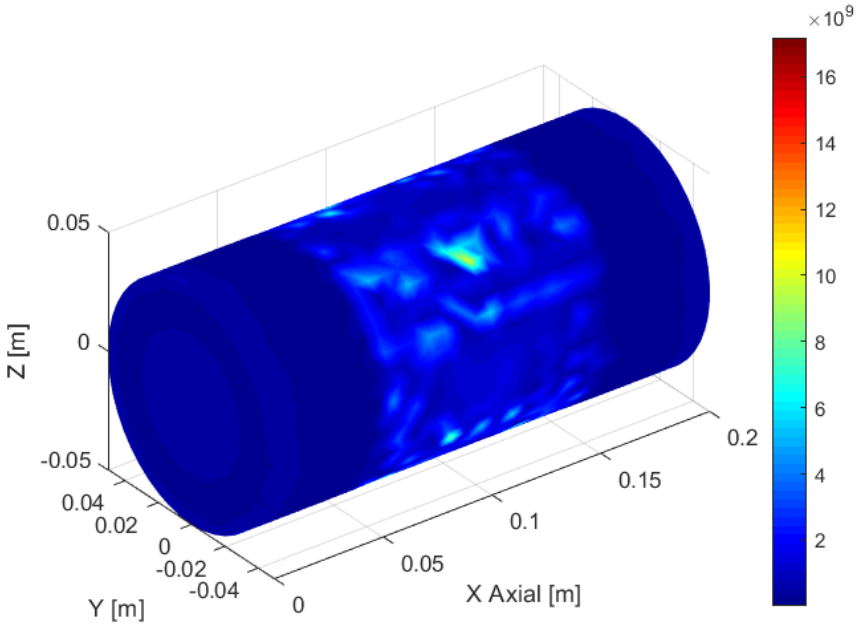

Figure 4.35 Von Mises stress distribution at the interface of the shaft-disk assembly

A structured mesh is generated for a shaft-disk assembly with conformal interface as shown in Figure 4.36. The conformity in the model implies the concentric alignment of each surface node set of the shaft and the disk. This constraint ensures the conformity for a deformed mesh after the penalty method is applied. The initial interference between the shaft and the disk is set as 0.05 mm. Then the contact node search algorithm pairs each node at the two domains, and the penalty algorithm finds the contact stiffness and contact forces at the interface. Figure 4.37 compares the undeformed structure and the deformed structure. Then the radial stress distribution is plotted in Figure 4.38. It is shown that no circumferential deviation is given in the solution, while the radial stress varies along with the axial direction. An analytical solution can be obtained as [65]

$$P = \frac{\delta}{\frac{d}{E_o}\left(\frac{d_o^2 + d^2}{d_o^2 - d^2} + \upsilon_o\right) + \frac{d}{E_i}\left(\frac{d^2 + d_o^2}{d^2 - d_o^2} - \upsilon_i\right)} \tag{4.26}$$

where P, δ, d_i, d_o, d, E_i, E_o, υ_i, and υ_o are the contact pressure in the radial direction at the interface, the diametral interference, the inner diameter of the shaft, the outer diameter of the disk, the nominal shaft diameter, Elastic modulus of the shaft, Elastic modulus of the disk, Poisson's ratio of the shaft, and Poisson's ratio of the disk, respectively. Table 4.9 compares the results from the analytical solution and the results from the finite element model.

From the demonstration, the use of structured mesh with conformal mesh interface is recommended for a rotor assembly since the circumferential contact is a common practice in rotating machinery.

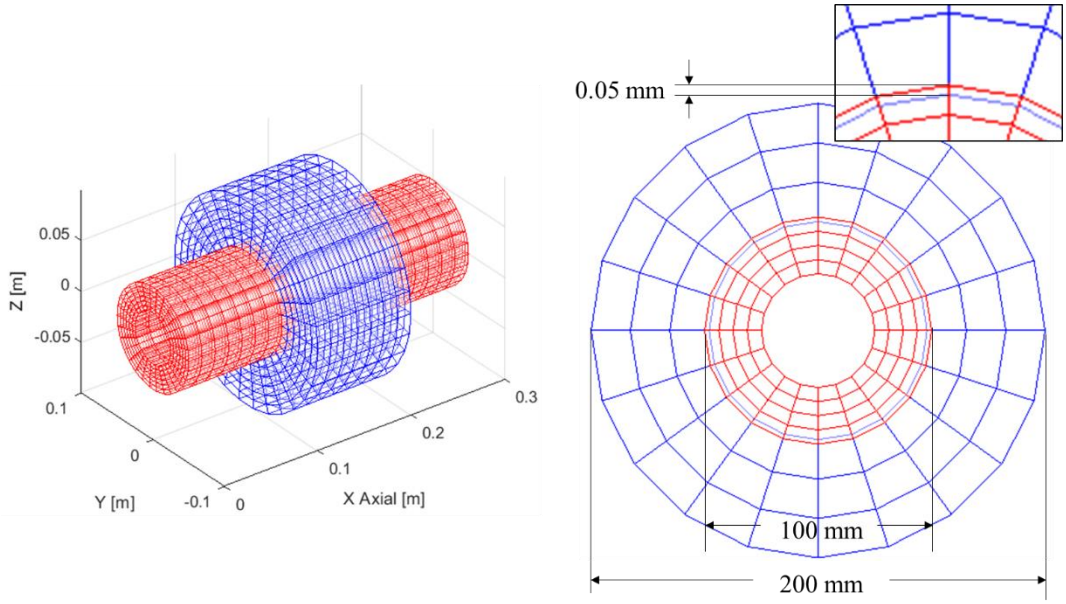

Figure 4.36 Structured mesh for a shaft-disk assembly with conformal contact interface

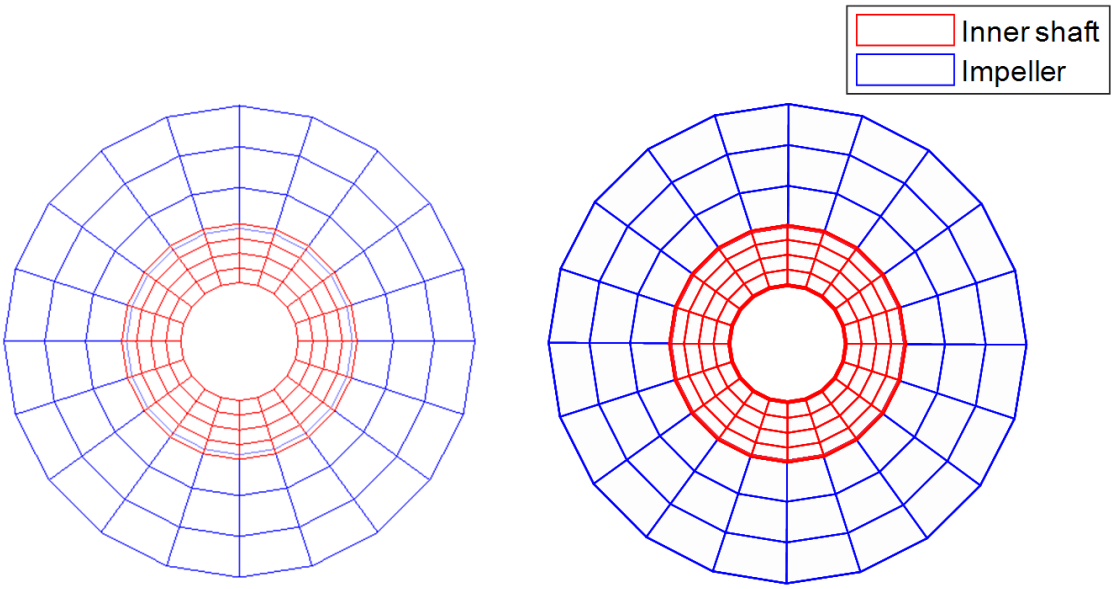

Figure 4.37 Deformation of the shaft-disk assembly by the penalty method

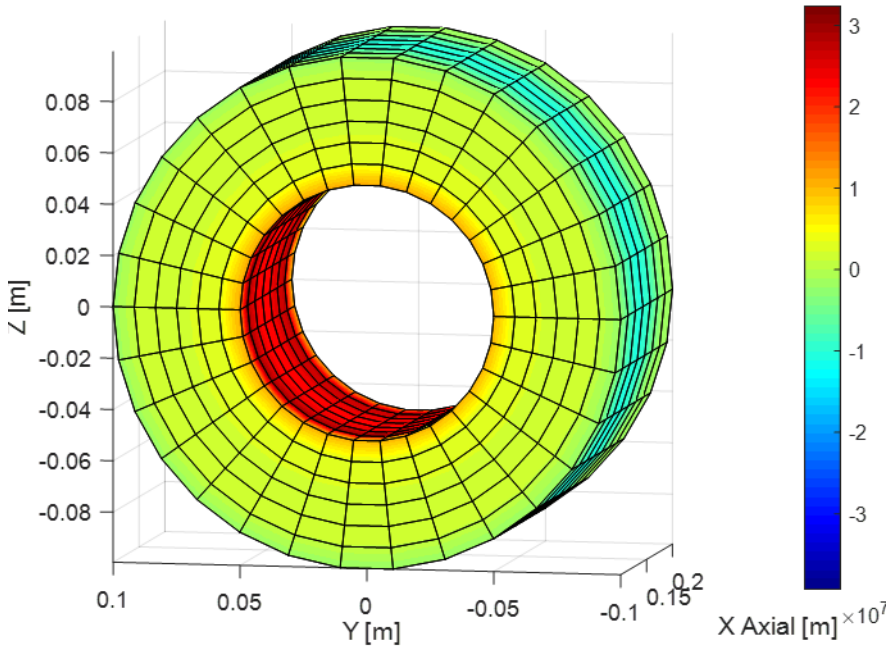

Figure 4.38 Radial stress distribution of the shaft-disk assembly with interference fit

Table 4.9 Comparison between analytical solution and FEM

	2D theory	3D FEM
σ_{max}	25.4 MPa	29.49 MPa
σ_{min}		10.57 MPa
σ_{avg}		21.69 MPa

4.4.5. Asperity Contact Model

The asperity contact model is another approach to deal with the rotor structure assembled with multiple parts. The theoretical derivation and validation is provided in Chapter 3. The asperity contact model is differentiated from general contact models, such as the penalty method, by several aspects as follows. The asperity contact model aims to find a physical contact stiffness which corresponds to the given preload, whereas the penalty method uses a numerical value for the contact stiffness. The contact stiffness in the penalty method may not reflect physical meanings. Instead, it is determined to satisfy the impenetrate condition. The value of *t* in the impenetrate condition of equation (4.16) becomes close to zero as penalty number increases, and it leads better compliance with the impenetrate condition. However, penalty number should be limited to prevent numerical singularity of the system stiffness matrix [77]. Hence, the asperity contact model may be an adequate choice for preloaded rotor assemblies.

In finite element analyses, structured mesh is preferred since it can provide good mesh quality and computational efficiency in general. However, structured mesh would require manual mesh generation and even highly skilled meshing technique when it

comes to complicated geometries. As for the penalty method, it is shown that structured conformal mesh at interfaces is nearly necessary for robust solutions. This is mainly because the gap function between nodes are significantly affected by the mesh structure. Regarding the asperity contact method, however, unstructured non-conformal mesh can also be used since the compliance for the impenetrate condition is unnecessary.

5. CONCLUSIONS

5.1. 3D Solid Finite Element Rotordynamics

The influences of the geometrical characteristics of rotor structures on rotordynamic characteristics of stability and critical speed prediction have been studied in this dissertation. The methodologies for conventional rotordynamic problems may be inadequate for high-fidelity rotor structure dynamic analyses. To account for the unconventional structural rotordynamic characteristics, novel modelling and analysis approaches using 3D solid finite element rotordynamic models were proposed. Unique computational algorithms were implemented by the standalone in-house 3D solid finite element rotordynamic code. It was shown that the novel modelling method provides more accurate prediction on parametric stability and critical speeds for complex-shaped rotor-bearing systems.

An efficient method was presented for rotordynamic stability simulation of systems with non-axisymmetric rotors and bearings, modeled with 3D solid finite elements. Ten (10) node quadratic tetrahedron elements were developed for modelling the non-axisymmetric rotor. Guyan reduction was utilized to reduce the dimension of the matrix differential equation to efficiently evaluate its monodromy matrices. Parametric instabilities in non-axisymmetric rotor-bearing systems were determined with Floquet theory, exploiting Hsu's method to discretize the Monodromy matrix. Numerical integration and a Routh-Hurwitz test were utilized to validate the approach for a Jeffcott rotor model with rectangular cross section. Use of Hsu's method and parallel

computation for evaluation of Monodromy matrices accelerated the computation time by a factor of 400 or more. The approximate Hsu approach was demonstrated to be highly accurate with a large order model example. Parametric studies were conducted to determine the effect of varying bearing and rotor asymmetry on the intensity of the instability and the speed ranges over which it will occur. The prior method using Hill's infinite determinant was compared with the proposed method using Hsu's method. The presented results imply that applications of Hill's method may be limited to the inertial coordinate system or to small level of bearing asymmetry in the rotor-fixed coordinate system, whereas the proposed method in this paper using Hsu's method accurately predicts the instability of the 3D solid rotor-bearing systems having complex geometries which require a large number of dofs and description in the rotor-fixed coordinate system without limitation of the level of bearing asymmetry. It was also shown that the proposed method becomes more advantageous as the number of dofs increases with respect to computational efficiency. A demonstration model with a Timoshenko beam rotor and fluid film journal bearings was developed to show that the proposed method can detect both parametric and non-parametric instabilities. A Root type impeller example was presented to illustrate the possibility of parametric instability (resonance) for practical, non-axisymmetric rotors. The system exhibited unstable behavior at spin speeds near the first bending modes, undamped natural frequencies.

The study presented a new high-fidelity, 3D solid element, finite contact method for the rotordynamic modeling of a rotor assembly with multiple preloaded parts and joints. A contact element for 3D solid finite element rotordynamic model was

introduced, and a finite element formulation for the contact element was presented. The contact element can be used for direct applications of statistics-based contact theories to the 3D solid finite element rotordynamic model. A test rig was built to validate the proposed contact modeling method. Multiple configurations, for various degrees of roughness at contact interfaces, were tested along with varying internal shaft preloads, and natural frequencies were measured. A prediction model for the test configurations was developed. An iterative calculation algorithm was introduced in order to solve the implicit equations between contact stiffness and stress distribution. Converged stress distributions of the rotor assembly, and contact stiffness at the interfaces in the test configurations were obtained for various degrees of interface roughness and preloads. Next, the natural frequencies of the rotor assembly were calculated and compared with the experimental results. The prediction results accurately follow the trend of the measurement with respect to the level of interface surface roughness and the increase of preloads. An overhung impeller type rotor bearing system simulation model was presented for demonstrating practical applications of the proposed modeling method. The simulation results demonstrate that the predicted critical speeds vary with respect to preload and contact surface roughness.

5.2. Future work

The current industrial practice in rotordynamic analyses still may have preference on using beam-type finite element rotor models, since it has been firmly established through industry working environments from generation to generation.

Therefore, one of the main remaining goals of the work should be seamless implementation of the suggested high-fidelity structural rotordyanmic analyses into the conventional beam-type finite element rotordynamics. It may be achieved by employing optimization algorithms to get tuned or adjusted beam-element corresponding 3D solid finite element rotordynamic components, such as couplings, blade disks, and etc.

The novel approach using 3D solid finite element Hsu's method parametric instability was suggested for complex-shaped non-axisymmetric rotor-bearing system. It was numerically shown that Hill's method may incorrectly predict unstable speed ranges when it comes to large non-axisymmetry for both rotor and bearings in the rotor-fixed coordinate system. Analytical demonstration should provide the limitations of these applications more clearly. Furthermore, experimental tests for rotor-bearing systems with large non-axisymmetry may prove the validity of the proposed method. Using the developed Hsu's method, steady-state imbalance response may be obtained which accounts for operating margins for non-axisymmetric rotor-bearing systems.

The contact model suggested in this dissertation is applicable to arbitrary geometries of coupling contact interfaces, while only demonstration models with flat contact interfaces were numerically investigated and experimentally validated. As the proposed method accounts for non-flat contact surface as well, such as Hirth-joint and Curvic-joint couplings, further studies on such non-flat contact interface cases can be conducted.

6. REFERENCES

[1] Genta, G., 2005, "Dynamics of Rotating Systems," Springer, NY.

[2] Childs, D. W., 1993, "Turbomachinery Rotordynamics," John Wiley & Sons, Inc., NJ.

[3] Jeffcott, H. H., 1919, "XXVII. The lateral vibration of loaded shafts in the neighbourhood of a whirling speed.—The effect of want of balance," The London, Edinburgh, and Dublin Philosophical Magazine and Journal of Science, 37(219), pp. 304-314.

[4] Prohl, M. A., 1945, "A general method for calculating critical speeds of flexible rotors," Transactions ASME 67, 67, p. A142.

[5] Myklestad, N. O., 1944, "A new method of calculating natural modes of uncoupled bending vibration of airplane wings and other types of beams.," Journal of the Aeronautical Sciences, 11(2), pp. 153-162.

[6] Nelson, H. D., 1980, "A Finite Rotating Shaft Element Using Timoshenko Beam Theory.," Journal of Mechanical Design, 102(4), pp. 793-803.

[7] Archer, J. S., 1963, "Consistent Mass Matrix for Distributed Mass Systems," Journal of the Structural Division, 89(4), pp. 161-178.

[8] Ruhl, R. L. and Booker, J. F., 1972, "A Finite Element Model for Distributed Parameter Turborotor Systems.," Journal of Manufacturing Science and Engineering, 94(1), pp. 126-132.

[9] Palazzolo, A. B., 2016, "Vibration Theory and Applications with Finite Elements and Active Vibration Control," Wiley, Chichester, UK.

[10] Hu, L. and Palazzolo, A., 2019, "An Enhanced Axisymmetric Solid Element for Rotor Dynamic Model Improvement," Journal of Vibration and Acoustics, 141(5), p. 051002.

[11] Cook, R. D., Malkus, D. S., Plesha, M. E. and Witt, R. J., 2002, "Concepts and Applications of Finite Element Analysis," John Wiley & Sons. Inc., NJ.

[12] Nandi, A. and Neogy, S., 2001, "Modelling of Rotors with Three-Dimensional Solid Finite Elements," Journal of Strain Analysis for Engineering Design, 36, pp. 359-371.

[13] Lazarus, A., Prabel, B. and Combescure, D., 2010, "A 3D Finite Element Model for the Vibration Analysis of Asymmetric Rotating Machines," Journal of Sound and Vibration, 329(18), pp. 3780-3797.

[14] Zeidan, F. Y., San Andres, L. and Vance, J. M., 1996, "Design And Application Of Squeeze Film Dampers In Rotating Machinery," Proceedings of the 25th Turbomachinery Symposium, pp. 169-188.

[15] Mortazavi, F. and Palazzolo, A. B., 2018, "Prediction of Rotordynamic Performance of Smooth Stator-Grooved Rotor Liquid Annular Seals Utilizing Computational Fluid Dynamics," Journal of Vibration and Acoustics, 140(3), p. 031002.

[16] Shin, D. and Palazzolo, A. B., 2020, "Nonlinear analysis of a geared rotor system supported by fluid film journal bearings," Journal of Sound and Vibration, 475, p. 115269.

[17] Hu, L., Palazzolo, A. and Karkoub, M., 2016, "Suppression of Lateral and Torsional Stick–Slip Vibrations of Drillstrings With Impact and Torsional Dampers," Journal of Vibration and Acoustics, 138(5), p. 051013.

[18] Hu, L. and Palazzolo, A., 2017, "Solid Element Rotordynamic Modeling of a Rotor on a Flexible Support Structure Utilizing Multiple-Input and Multiple-Output Support Transfer Functions," Journal of Engineering for Gas Turbines and Power, 139(1), p. 012503.

[19] G. Vannini, 2014, "Rotordynamic Validation of an Ultra High Speed Multistage Centrifugal Compressor Stacked Rotor," Turbine Technical Conference and Exposition, Duesseldorf, Germany.

[20] Oh, J., Palazzolo, A. and Hu, L., 2020, "Stability of Non-Axisymmetric Rotor and Bearing Systems Modeled With Three-Dimensional-Solid Finite Elements," Journal of Vibration and Acoustics, 142(1), p. 011010.

[21] Chatelet, E., D'Ambrosio, F. and Jascquet-Richardet, G., 2005, "Toward Global Modelling Approaches for Dynamic Analyses of Rotating Assemblies of Turbomachines," Journal of Sound and Vibration, 282, pp. 163-178.

[22] Combescure, D. and Lazarus, A., 2008, "Refined Finite Element Modelling for the Vibration Analysis of Large Rotating Machines: Application to the Gas Turbine Modular Helium Reactor Power Conversion Unit," Journal of Sound and Vibration, 318, pp. 1262-1280.

[23] Chaudhry, J. A., 2011, "3-D Finite Element Analysis of Rotors in Gas Turbines, Steam Turbines and Axial Pumps including Blade Vibrations," Ph.D. Thesis, University of Virginia, Charlottesville, VA.

[24] Black, H. F., 1969, "Parametrically Excited Lateral Vibrations of an Asymmetric Slender Shaft in Asymmetrically Flexible Bearings," Proceedings of the Institution of Mechanical Engineers, Part C, 11(1), pp. 57-67.

[25] Hsu, C. S., 1963, "On the Parametric Excitation of a Dynamic System Having Multiple Degress of Freedom," Journal of Applied Mechanics, 85(Series E), pp. 367-372.

[26] Genta, G., 1988, "Whirling of Unsymmetrical Rotors: A Finite Element Approach Based on Complex Coordinates," Journal of Sound and Vibration, 124(1), pp. 27-53.

[27] Oncescu, F., Lakis, A. A. and Ostiguy, G., 2001, "Investigation of the Stability and Steady State Response of Asymmetric Rotors, Using Finite Element Formulation," Journal of Sound and Vibration, 245(2), pp. 303-328.

[28] Nandi, A. and Neogy, N., 2005, "An Efficient Scheme for Stability Analysis of Finite Element Asymmetric Rotor Models in a Rotating Frame," Finite Elements in Analysis and Design, 41, pp. 1343-1364.

[29] Ma, W. M., Wang, J. J. and Wang, Z., 2015, "Frequency and Stability Analysis Method of Asymmetric Anisotropic Rotor-Bearing System Based on Three-Dimensional Solid Finite Element Method," Journal of Engineering for Gas Turbines and Power, 137, p. 102502.

[30] Tai, W. C. and Shen, I. Y., 2015, "Closed-Form Vibration Response of a Special Class of Spinning, Cyclic Symmetric Rotor-Bearing-Housing Systems," Journal of Vibration and Acoustics, 137, p. 061011.

[31] Hsu, C. S., 1974, "On Approximating a General Linear Periodic system," Journal of Mathematical Analysis and Applications, 45, pp. 234-251.

[32] Oh, J., Kim, B. and Palazzolo, A. B., 2021, "3D Solid Finite Element Contact Model for Rotordynamic Analysis: Experiment and Simulation," Journal of Vibration and Acoustics, doi: https://doi.org/10.1115/1.4048556.

[33] Greenwood, J. A. and Williamson, J. B. P., 1966, "Contact of nominally flat surfaces," Proceedings of the Royal Society A: Mathematical, Physical, Engineering Sciences, 295(1442), pp. 300-319.

[34] Müser, M. H., Dapp, W. B., Rugnicourt, R. and et al., ., 2017, "Meeting the Contact-Mechanics Challenge," Tribology Letter, 65(4), p. 118.

[35] Petrov, E. P. and Ewins, D. J., 2003, "Analytical Formulation of Friction Interface Elements for Analysis of Nonlinear Multi-Harmonic Vibrations of Bladed Disks," Journal of Turbomachinery, 125(2), pp. 364-371.

[36] Firrone, C. M. and Zucca, S., 2009, "Underplatform dampers for turbine blades: The effect of damper static balance on the blade dynamics," Numerical Analysis-Theory and Application, 36(4), pp. 515-522.

[37] Mayer, M. H. and Gaul, L., 2007, "Segment-to-segment contact elements for modelling joint interfaces in finite element analysis," Mechanical Systems and Signal Processing, 21(2), pp. 724-734.

[38] Brake, M. R., Reuss, P., Segalman, D. J. and Gaul, L., 2014, "Variability and Repeatability of Jointed Structures with Frictional Interfaces," 32nd International Modal Analysis Conference (IMAC XXXII), Orlando.

[39] Süß, D. and Willner, K., 2015, "Investigation of a jointed friction oscillator using the Multiharmonic Balance Method," Mechanical Systems and Signal Processing, 52-53, pp. 73-87.

[40] Festjens, H., Chevallier, G. and Dion, J. L., 2014, "Nonlinear model order reduction of jointed structuresfor dynamic analysis," Journal of Sound and Vibration, 333(7), pp. 2100-2113.

[41] Gaul, L. and Lenz, J., 1997, "Nonlinear dynamics of structures assembled by bolted joints," Acta Mechanica, 125(1-4), pp. 169-181.

[42] Brake, M. R., 2017, "The mechanics of jointed structures: recent research and open challenges for developing predictive models for structural dynamics," Springer, Cham, Switzerland.

[43] Fantetti, A., Tamatam, L. R., Volvert, M., Lawal, I., Liu, L., Salles, L., Brake, M. R., Schwingshackl, C. W. and Nowell, D., 2019, "The impact of fretting wear on structural dynamics: Experiment and Simulation," Tribology International, 138, pp. 111-124.

[44] Stender, M., Papangelo, A., Allen, M., Brake, M. R., Schwingshackl, C. and Tiedemann, M., 2016, "Structural Design with Joints for Maximum Dissipation," Shock & Vibration, Aircraft/Aerospace, Energy Harvesting, Acoustics & Optics, vol. 9.

[45] Peyret, N., Chevallier, G. and Dion, J. L., 2013, "Dynamics of Assembled Structures: Taking Into Account the Surface Defects in Interfaces," ASME 2013 International Design Engineering Technical Conferences and Computers and Information in Engineering Conference, Portland, France..

[46] Gastaldi, C. and Gola, M. M., 2016, "On the relevance of a microslip contact model for under-platform dampers," International Journal of Mechanical Sciences, 115-116, pp. 145-156.

[47] Zhang, Y., Du, Z., Shi, L. and Liu, S., 2010, "Determination of Contact Stiffness of Rod-Fastened Rotors Based on Modal Test and Finite Element Analysis," Journal of Engineering for Gas Turbine and Power, 132(9), p. 094501.

[48] Peng, H., Liu, Z., Wang, G. and Zhang, M., 2011, "Rotor Dynamic Analysis of Tie-Bolt Fastened Rotor Based on Elastic-Plastic Contact," Proceedings of ASME Turbo Expo 2011, Vancouver, British Columbia, Canada.

[49] Gao, J., Yuan, Q., Li, P., Feng, Z., Zhang, H. and Lv, Z., 2012, "Effects of Bending Moments and Pretightening Forces on the Flexural Stiffness of Contact Interfaces in Rod-Fastened Rotors," Journal of Engineering for Gas Turbines and Power, 134(10), p. 102503.

[50] Lu, M., Geng, H., Xu, G. and Yu, L., 2013, "Analytical and Experimental Study of Dynamic Chracteristics of Rod Fastened Rotor-Bearing System under Preload Saturation," Proceddings of ASME Turbo Expo 2013: Turbine Technical Conference and Exposition, San Antonio, Texas, USA.

[51] Zhuo, M., Yang, L. H. and Yu, L., 2016, "Contact Stiffness Calculation and Effects on Rotordynamic of Rod Fastened Rotor," Proceedings of the ASME 2016 International Mechanical Engineering Congress and Exposition, Phoenix, Arizona, USA.

[52] Liu, X., Yuan, Q., Liu, Y. and Gao, J., 2014, "Analysis of the Stiffness of Hirth Couplings in Rod-Fastened Rotors Based on Experimental Modal Parameter Identification," Proceedings of ASME Turbo Expo 2014: Turbine Technical Conference and Exposition, Duesseldorf, Germany.

[53] Rimpel, A. M. and Leopard, M., 2020, "Simple Contact Stiffness Model Validation for Tie Bolt Rotor Design With Butt Joints and Pilot Fits," Journal of Engineering for Gas Turbine and Power, 142(1), p. 011014.

[54] Floquet, G., 1883, "Sur les équations différentielles linéaires à coefficients périodiques," Annales de l'École Normale Supérieure, 12, pp. 47-88.

[55] Guyan, R. J., 1965, "Reduction of Stiffness and Mass Matrices," AIAA Journal, 3(2), p. 380.

[56] Thomas, O., Lazarus, A. and Touze, C., 2010, "A Harmonic-based Method for Computing the Stability of Periodic Oscillations of Non-linear Structural Systems," Proceedings of the IDETC-CIE, Montreal, Quebec, Canada, August 15-18, 2010, ASME Paper No. DETC2010-28407.

[57] Loewy, R. G., 1969, "Dynamic of Rotating Shafts," The Shock and Vibration Information Center United States Department of Defense, Washington, DC.

[58] Someya, T., 1931, "Journal-Bearing Databook," Springer-Verlag Berlin Heidelberg GmbH, NY.

[59] A. Bucur, "Linear Systems, MIT Department of Mathematics," 2009, accessed 2018, http://www-math.mit.edu/~alina/18.03/linsys.pdf.

[60] Bishop, R. and Parkinson, A., 1965, "Second Order Vibrations of Flexible Shafts," Philosophical Transactions of the Royal Society, 259, pp. 1-31.

[61] McCool, J. I., 1986, "Comparison of Models for the Contact of Rough Surfaces," Wear, 107(1), pp. 37-60.

[62] Bhushan, B., 1998, "Contact mechanics of rough surfaces in tribology: multiple asperity contact," Tribology Letters, 4(1), pp. 1-35.

[63] Abramowitz, M. and Stegun, I. A., 1965, "Handbook of Mathematical Functions," General Publishing Company, Ltd., Toronto, Ontario.

[64] Sherif, H. A. and Kossa, S. S., 1991, "Relationship between normal and tangential contact stiffness of nominally flat surfaces," Wear, 151(1), pp. 49-62.

[65] Budynas, R. G., Nisbett, J. K. and Shingley, J. E., 2008, "Shigley's Mechanical Engineering Design," McGraw-Hill, New York.

[66] Kessel, R., Kacker, R. and Berglund, M., 2006, "Coefficient of contribution to the combined standard uncertainty," Metrologia, 43(4), p. S189.

[67] Balbahadur, A. C. and Kirk, R. G., 2004, "Part II - Case Studies for a Synchronous Thermal Instability Operating in Overhung Rotors," International Journal of Rotating Machinery, 10(6), pp. 477-487.

[68] Yang, J. and Palazzolo, A. B., 2019, "Three-Dimensional Thermo-Elasto-Hydrodynamic Computational Fluid Dynamics Model of a Tilting Pad Journal Bearing—Part I: Static Response," Journal of Tribology, 141(6), p. 061702.

[69] Yang, J. and Palazzolo, A. B., 2019, "Three-Dimensional Thermo-Elasto-Hydrodynamic Computational Fluid Dynamics Model of a Tilting Pad Journal Bearing—Part II: Dynamic Response.," Journal of Tribology, 141(6), p. 061703.

[70] Shin, D., Yang, J., Tong, X., Suh, J. and Palazzolo, A. B., 2020, "A Review of Journal Bearing Thermal Effects on Rotordynamic Response," Journal of Tribology.

[71] Yang, J. and Palazzolo, A., 2021, "Computational Fluid Dynamics Based Mixing Prediction for Tilt Pad Journal Bearing TEHD Modeling—Part I: TEHD-CFD Model Validation and Improvements," Journal of Tribology, 143(1), p. 011801.

[72] Yang, J. and Palazzolo, A., 2021, "Computational Fluid Dynamics Based Mixing Prediction for Tilt Pad Journal Bearing TEHD Modeling—Part II: Implementation With Machine Learning," Journal of Tribology, 143(1), p. 011802.

[73] Shin, D. and Palazzolo, A. B., 2021, "Tilting Pad Journal Bearing Misalignment Effect on Thermally Induced Synchronous Instability (Morton Effect)," Journal of Tribology, 143(3), p. 031802.

[74] Shin, D., Palazzolo, A. and Tong, X., 2020, "Squeeze Film Damper Suppression of Thermal Bow-Morton Effect Instability," ASME Journal of Engineering for Gas Turbines and Power, doi: https://doi.org/10.1115/1.4048602.

[75] Guyan, R. J., 1965, "Reduction of Stiffness and Mass Matrices," AIAA J., 3(2), p. 380.

[76] Cifuentes, A. O. and Kalbag, A., 1992, "A performance study of tetrahedral and hexahedral elements in 3-D finite element structural analysis," Finite Elements in Analysis and Design, 12(Elsevier), pp. 313-318.

[77] Kim, N., 2014, "Introduction to Nonlinear Finite Element Analysis," Springer Science & Business Media, New York.

[78] Trujillo, D. M. and Pappoff, C. G., 2002, "A general thermal contact resistance finite element," Finite Elements in Analysis and Design, 38(3), pp. 263-276.

APPENDIX A

Appendix A mainly describes constraint equations given in [11].

Provided constraint equations are given as

$$\underline{\boldsymbol{C}} \cdot \underline{\boldsymbol{D}} - \underline{\boldsymbol{Q}} = \underline{\mathbf{0}} \tag{A.1}$$

$$[\underline{\boldsymbol{C}}_r \quad \underline{\boldsymbol{C}}_c] \begin{bmatrix} \underline{\boldsymbol{D}}_r \\ \underline{\boldsymbol{D}}_c \end{bmatrix} - \underline{\boldsymbol{Q}} = \underline{\mathbf{0}} \tag{A.2}$$

$$\begin{bmatrix} \underline{\boldsymbol{D}}_r \\ \underline{\boldsymbol{D}}_c \end{bmatrix} = \begin{bmatrix} \underline{\boldsymbol{I}} \\ -\underline{\boldsymbol{C}}_c^{-1} \underline{\boldsymbol{C}}_r \end{bmatrix} \underline{\boldsymbol{D}}_r + \begin{bmatrix} \underline{\mathbf{0}} \\ \underline{\boldsymbol{C}}_c^{-1} \underline{\boldsymbol{Q}} \end{bmatrix} \tag{A.3}$$

$$\underline{\boldsymbol{D}} = \underline{\boldsymbol{T}}\, \underline{\boldsymbol{D}}_r + \underline{\boldsymbol{Q}}_0 \tag{A.4}$$